Advances in

Geosciences

Volume 5: Oceans and Atmospheres (OA)

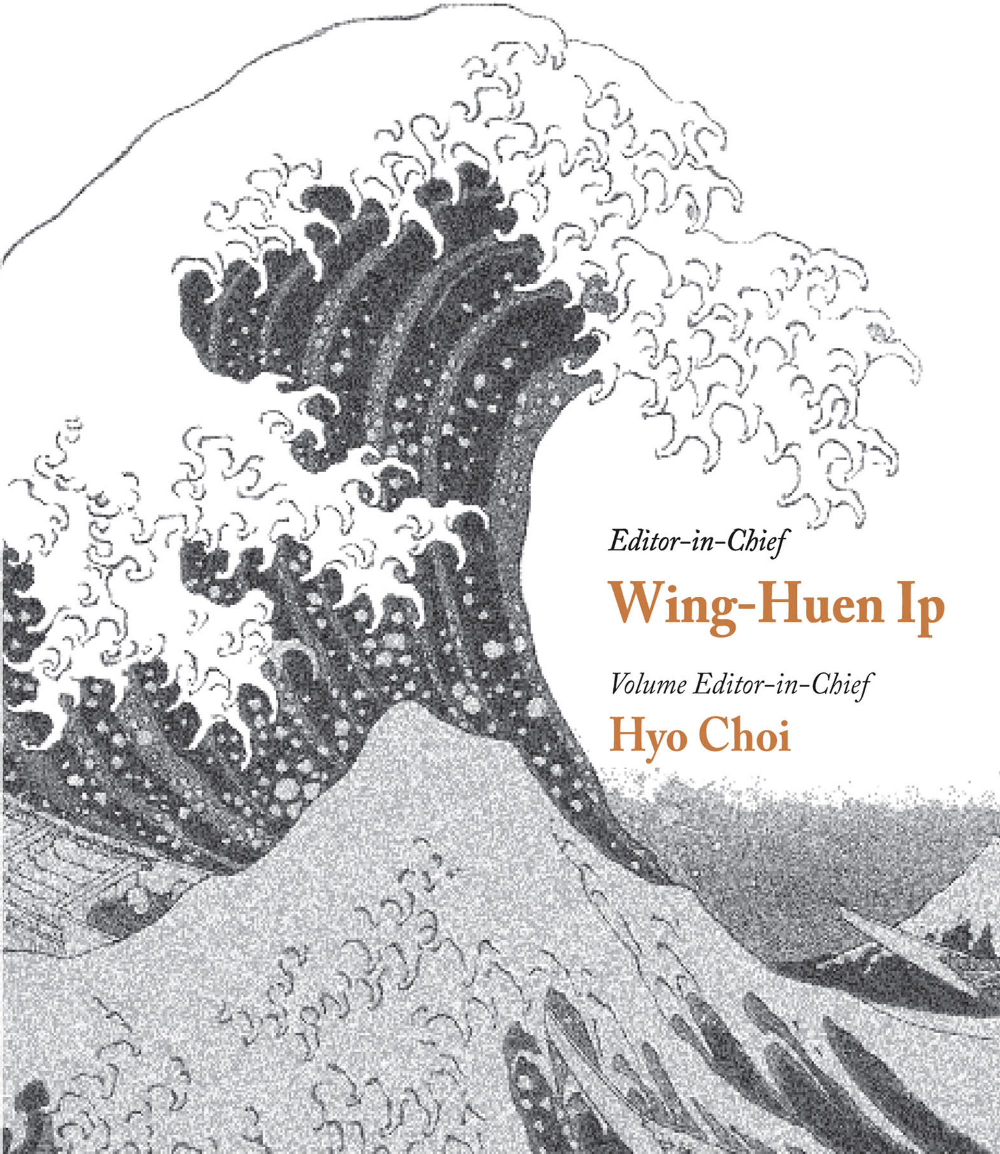

Editor-in-Chief

Wing-Huen Ip

Volume Editor-in-Chief

Hyo Choi

Choi

Advances in **Geosciences**

Volume 5

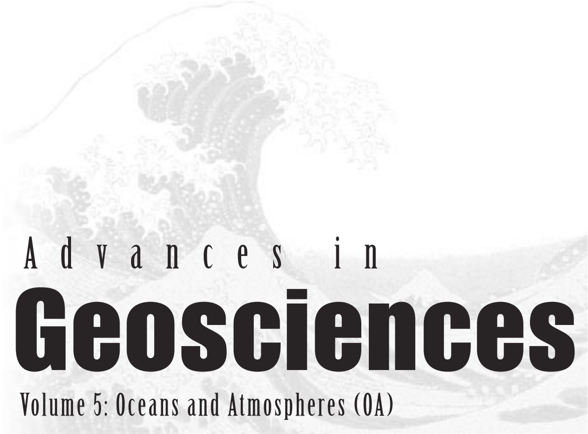

Advances in

Geosciences

Volume 5: Oceans and Atmospheres (OA)

ADVANCES IN GEOSCIENCES
A 5-Volume Set
Editor-in-Chief: Wing-Huen Ip *(National Central University, Taiwan)*

Volume 1: Solid Earth (SE)
ISBN 981-256-985-5

Volume 2: Solar Terrestrial (ST)
ISBN 981-256-984-7

Volume 3: Planetary Science (PS)
ISBN 981-256-983-9

Volume 4: Hydrological Science (HS)
ISBN 981-256-982-0

Volume 5: Oceans and Atmospheres (OA)
ISBN 981-256-981-2

Advances in

Geosciences

Volume 5: Oceans and Atmospheres (OA)

Editor-in-Chief

Wing-Huen Ip

National Central University, Taiwan

Volume Editor-in-Chief

Hyo Choi

Kangnung National University, Korea

World Scientific

NEW JERSEY • LONDON • SINGAPORE • BEIJING • SHANGHAI • HONG KONG • TAIPEI • CHENNAI

Published by

World Scientific Publishing Co. Pte. Ltd.
5 Toh Tuck Link, Singapore 596224
USA office: 27 Warren Street, Suite 401-402, Hackensack, NJ 07601
UK office: 57 Shelton Street, Covent Garden, London WC2H 9HE

British Library Cataloguing-in-Publication Data
A catalogue record for this book is available from the British Library.

ADVANCES IN GEOSCIENCES
A 5-Volume Set
Volume 5: Oceans and Atmospheres (OA)

ISBN 981-256-456-X (Set)
ISBN 981-256-981-2 (Vol. 5)

Typeset by Stallion Press
Email: enquiries@stallionpress.com

Printed in Singapore.

EDITORS

Editor-in-Chief: Wing-Huen Ip

Volume 1: Solid Earth (SE)
Editor-in-Chief: Chen Yuntai
Editor: Zhong-Liang Wu

Volume 2: Solar Terrestrial (ST)
Editor-in-Chief: Marc Duldig
Editors: P. K. Manoharan
Andrew W. Yau
Q.-G. Zong

Volume 3: Planetary Science (PS)
Editor-in-Chief: Anil Bhardwaj
Editors: Francois Leblanc
Yasumasa Kasaba
Paul Hartogh
Ingrid Mann

Volume 4: Hydrological Science (HS)
Editor-in-Chief: Namsik Park
Editors: Eiichi Nakakita
Chulsang Yoo
R. B. Singh

Volume 5: Oceans & Atmospheres (OA)
Editor-in-Chief: Hyo Choi
Editor: Milton S. Speer

REVIEWERS

All the papers published in this volume have been reviewed by

Dr. Hyo Choi, Professor
Department of Atmospheric Environmental Sciences
Kangnung National University
Kangnung, 210-702
Korea

and

Dr. Milton S. Speer, Professor
School of Mathematics
The University of New South Wales
Sydney, NSW
Australia 2052

Contents

SABAH SHORELINE MANAGEMENT PLAN

FLEMMING JAKOBSEN*, JULIEN FRACHISSE
and NEIL HARTSTEIN
DHI Water and Environment (M) Sdn. Bhd.
Sabah, Malaysia
**flj@dhi.dk*

The management of the coastline around Sabah faces numerous conflicting interests from the public, private, and industry groups. The public demands socio-economic growth, sustainable development, and preservation of natural resources while the private sector and industry demand local coastal protection and often reckless development. To resolve these issues the creation of a management plan for Sabah's coastline has been initiated. Numerical models of both catchments and sea were used to integrate available information and simulate the consequences of different development scenarios. The focus of the paper is on the integration of information, but some details are also given on the important conflicts and habitat threats.

1. Introduction

Major population centers and socio-economic growth in Sabah is concentrated in the coastal area. The management of the shoreline is therefore of critical importance. Economic growth in Sabah is driven mainly by agricultural development, however, the tourism industry is also growing at >20% per year and has strong development potential.

Sabah's coastal environment is dominated by wetland, coral reef, and seagrass ecosystems (Fig. 1). These ecosystems are important for the physical protection of coastal habitat, economically in supporting fishing, aquaculture, forestry, and tourism industries and finally to protect and preserve natural resources for future generations.

Increasing population and resulting urbanization have altered environmental conditions in coastal areas.[1] The deterioration of the coastal environment is visible to everybody residing in or visiting Sabah and is of general growing concern.

Development in catchment areas can potentially influence coastal environmental conditions. For that reason the coastal area cannot be seen in isolation. Planning, zoning and controlling coastal areas can optimize coastal

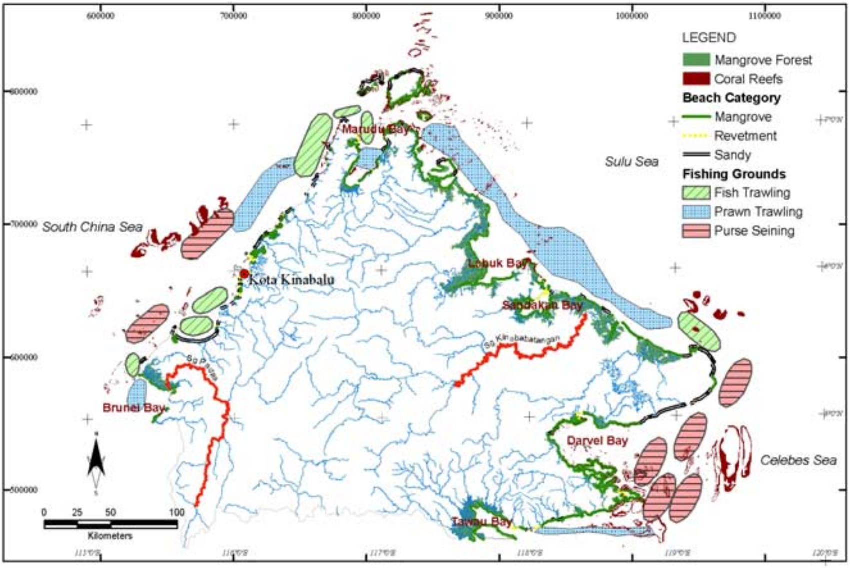

Fig. 1. Map of Sabah showing capital, major rivers, mangrove, coastal classification, coral reef data, and fishing information.

development while preserving natural resources, but can do little about the development in the upstream catchment.

The aim of the Shoreline Management Plan study is to produce a development plan for the Sabah shoreline which is sensitive to the particular conditions of the coast and is consistent with the general development policies of Sabah State.[2,3] The methodology applied to develop a shoreline management plan for Sabah is considered an example to be followed along many coastal areas in Southeast Asia, and around the world, in resolving the impact of inland development on the coastal environment.

2. Measurements and Methods

Numerical models served to integrate the available information to hind-cast and now-cast physical conditions and predict the consequences of different development scenarios.

Sabah was divided into 79 subcatchments and the rainfall-runoff calculated. Sediment and pollution load were also calculated. The sediment and pollution loads were imposed in the coastal models to simulate the spreading of sediment and pollution in the coastal area. Year 2003 was chosen as "design period" for "production runs" as analysis showed it was an average year for rainfall, catchment runoff etc. Details can be found in the project reports.

3. Coastal Ecology Results

A detailed understanding of the coastal ecology and the distribution of the dominant ecological systems along Sabah's coastline (Fig. 1) guides a sound sustainable management of the coastal environment.

In 1999–2002 the total area of Sabah mangroves was 341,377 ha. Based on analysis of recent satellite images, mangroves presently cover an area of 327,678 ha. Overall, in Sabah, as elsewhere in Malaysia, the main threats to mangroves arise from wholesale clearing and destruction of mangrove habitats, rather than indirect impacts such as changes in water quality, sedimentation, etc. In general mangroves are resilient to environmental changes.[4]

Owing to the importance of mangrove forests, the primary management objective under the SMP for mangrove areas is protection and conservation. Economic objectives, such as aquaculture or other mangrove conversion for development, should only be considered in specific areas with clear limits and guidelines.

The waters around Sabah support over 75% of all Malaysian coral reefs. The main causes of reef habitat loss in Sabah are the use of destructive fishing methods, and sediment erosion from improper development along the coast and in the hinterland leading to coral mortality from high turbidity and/or burial. There has been a dramatic rise in sediment and nutrient loads of rivers in Sabah over the past two decades with adverse effects on the coral reef ecosystem.

Good quality coral reef areas shall be considered "critical environmental capital," the preservation of which is essential to achieve environmental sustainability. Buffer zones around good quality coral reef areas shall be established under the SMP based on knowledge of water flow and existing suspended sediment and pollution loadings to appropriately restrict adjacent and nearby shoreline area development.

Seagrass beds intermix with coral reefs or cover shallow areas that fringe mangrove swamps. Seagrass beds in many areas around Sabah are at risk due to siltation.

Under the SMP all remaining coastal areas containing seagrass are to be protected as either wildlife or marine reserves and are also considered "critical environmental capital," given its importance in supporting the fisheries resource.

In terms of the SMP, the distribution of rare and endangered marine fauna must be taken into consideration in terms of habitat connectivity in establishing the location of protected areas. In addition the SMP must consider the siting of industrial or other development areas to avoid heavy marine traffic conflicting with marine faunal habitats and any known migration routes.

Within this study we do apply water quality standards, but also consider known tolerances from previous investigations on seagrass[5] and corals.[6]

4. Results on Sediment Load and Sediment Plumes

Sediment (soil) is eroded from the land catchments of Sabah, during rainfall events, and is transported by rivers to the coastline (Fig. 2).

The soil erosion at a given location in the catchment is governed by soil type, land use, terrain and rainfall-runoff, while the amount transported to the coastline is governed by the river systems. Erosion depends mostly on terrain and land use and the main generators of soil erosion are croplands,

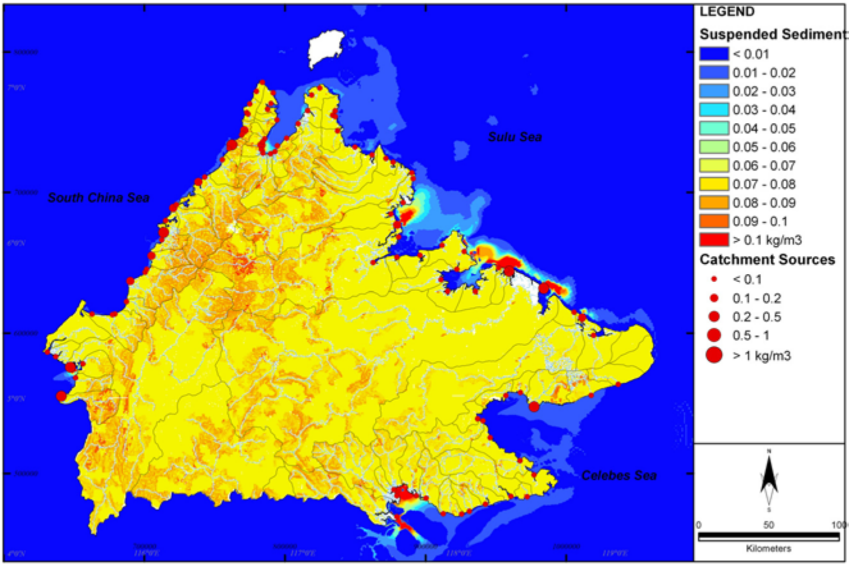

Fig. 2. Annual averaged (2003) suspended sediment load at the coastline, and suspended sediment concentrations on May 19, 2003 at 18:00.

cleared land (including logging) and oil palm plantations. The major sources of sediment to coastal waters are found along the northeast coast of Sabah (including Kinabatangan River).

The actual sediment concentration at an offshore location depends on the sediment load and water exchange. The areas most influenced by high suspended sediment concentrations are Tawau and Indonesian bays. Darvel Bay is influenced in areas immediately adjacent to the source, in contrast Labuk Bay and the Sulu Sea have high concentrations most of the year. It is highly likely that the concentrations in these embayments have increased due to land-based activities. Along the coastline towards the South China Sea and towards the Sulu Sea, an area 5–10 km in width is influenced.

Comparing the sediment concentration and the coral reef distribution, it is found that in areas with high concentrations, either no coral reefs or only poor quality reefs were found. Likewise a correlation between high sediment concentrations, mangrove forest and prawn trawling grounds was found.

5. Results on Pollution Loads and Coastal Distribution

Pollution loads from land depend on the nature and extent of industry, population and agriculture present in each catchment, and also on the distance from the coastline and runoff quantity. In addition, biological processes also affect the concentrations.

Heavy industrial polluters are located in or around major cities and growth centers. Population concentrations in urban areas generate significant amounts of BOD, TN, TP, and in particular *E-coli.* Agricultural or cultivated areas such as oil palm plantations are a significant source of nitrogen and phosphorus.

Pollutants tend to accumulate in semienclosed areas, such as several of the bays. In general, calculated concentrations meet water quality standards, but the assessment needs to be made in greater detail.

6. Discussion and Conclusion

Through the baseline data collection and analyzes as described in the above sections, a detailed understanding of the issues relating to Sabah's coastline has been established, allowing management objectives to be set. Threats to mangrove forests have been identified in terms of clearing and reclamation, thus protection of mangroves can be considered a management objective.

The *management objectives* are general in that they represent a set of alternatives for the overall study area from which specific strategies for specific areas or coastal reaches can be applied. Following the development of a list of broad management objectives, the coastline is then divided into *management units* whereby primary and secondary objectives are selected from this list for each unit based upon the particular characteristics of that unit. In carrying this out, extensive use of suitability mapping, threat mapping will be undertaken using GIS. For the purposes of the SMP, the preferred management objectives for each management unit will be chosen on the basis of the issue or sector given the most weighting. There is a considerable degree of subjectivity and potential conflicts in this process, thus necessitating extensive input and feedback of the relevant government authorities, NGO's, local community leaders and where possible, the local community.

In considering management strategies for each unit, an appraisal of alternative strategies will be considered and tested against the objectives for the management unit and the preferred sustainable option selected. Testing of the management strategies will involve an appraisal of the extent to which they fulfil the primary and secondary objectives.

The zoning and management strategies to be developed as part of the SMP can be regarded as a planning tool for sustainable development of the shoreline on a regional scale.

References

1. GCRMN. Status of coral reefs of the world, in ed. C. Wilkinson, *Global Coral Reef Monitoring Network*, Australian Institute of Marine Science, 2000.
2. D. Ir and Hj. K. Bin Abdullah, Integrated coastal management for sustainable development, *Buletin Ingenieur* (2002).
3. M. B. Moktar and S. A. B. A. G. Aziz, Integrated coastal zone management using the ecosystems approach, some perspectives in Malaysia, *Ocean & Coastal Management* **46** (2003).
4. J. C. Ellison, Impacts of sediment burial on mangroves, *Marine Pollution Bulletin* **37** (1999).
5. J. Terrados, C. M. Duarte, M. D. Fortes, J. Borum, N. S. R. Agawin, S. Bach, U. Thampanya, L. Kamp-Nielsen, W. J. Kenworthy, O. Geertz-Hansen and J. Vermaat, Changes in community structure and biomass of seagrass communities along gradients of siltation in SE Asia, *Estuarine Coastal and Shelf Science* **46** (1998).
6. C. S. Rogers, Responses of coral reefs and reef organisms to sedimentation, *Marine Ecology Progress Series* **62** (1990).

THE SPATIAL DISTRIBUTION OF CHLOROPHYLL-*a* AND ITS RESPONSES TO OCEANOGRAPHIC ENVIRONMENTS IN THE SOUTH CHINA SEA

HUI ZHAO and DANLING TANG*
Laboratory for Tropical Marine Environmental Dynamics
South China Sea, Institute of Oceanology
Chinese Academy of Sciences, Guangzhou-510301, P. R. China
**lingzistdl@126.com*

This study investigates the spatial distribution of Chlorophyll *a* (Chl-*a*) in the summer season for the South China Sea (SCS) using satellite measurements and discusses the mechanisms of spatial variation of phytoplankton. Results show that Chl-*a* concentrations are higher in the west than in the east of the SCS. Chl-*a* concentrations in the west central basin, southeast of Vietnam and a jet like band east of Phan Ri Bay are evidently higher than in the rest of the SCS. Their spatial characteristics are related to upwelling derived from Ekman pumping, Ekman transport induced by southwest monsoon winds, and the strong offshore current east of Vietnam.

1. Introduction

The South China Sea (SCS) is the largest marginal sea, in the western Pacific Ocean covering 3.5 million km^2 from the equator to 23°N and from 99°E to 121°E, with an average depth of 2000 m (Fig. 1). The monsoons always play an important role in the dynamics of upper circulations of SCS throughout the year,[1,2] as it is dominated by strong northeasterly monsoon during winter (December–February) and southwesterly monsoon in summer (June–August).[3] The seasonally reversing monsoons arouse considerable changes in general oceanic circulations and hydrological features,[4,5] whilst southwesterly winds and the orientation of the coastline provide favorable conditions for wind-induced upwelling along the SCS west coast.[1,4] In addition, a strong offshore current northeast of Vietnam,[1,4,6] may also exert important influence on the growth of phytoplankton, especially the chlorophyll-*a* (Chl-*a*) close related to primary productivity in the northern SCS, and possibly over the whole SCS, by bringing nutrients from sublayer waters.

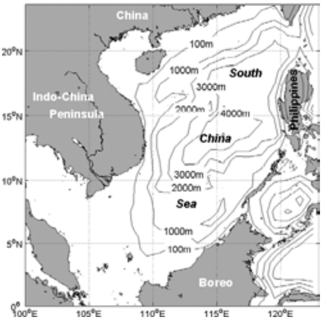

Fig. 1. Bathymetric and geographic map of the SCS. PRB: Phan Ri Bay.

Tang[7–9] studied spatio-temporal variability of regional chlorophyll and primary productivities in the SCS continental shelf, the Gulf of Tonkin and inshore Vietnamese coastal waters, and analyzed water conditions during the corresponding period based on *in situ* measurements and satellite data. Shang[10] and Tang[11] analyzed the distribution of Chl-*a* in upwelling zones. Hung *et al.*,[12] Lee Chen *et al.*,[13] and Agawin *et al.*[14] discussed the relation between biomass of phytoplankton and nutrient conditions. Chen *et al.*[15] investigated elementarily seasonal and spatial characteristics of chlorophyll concentrations of the SCS.

Tang *et al.*[9] observed high-chlorophyll concentrations in a jet-shape on the northeastern region of Phan Ri Bay (PRB) with sustaining nutrients-rich transport through the offshore current during almost the whole summer. Tang *et al.*[16] also observed harmful algal blooms (HABs) during July caused by upwelling. We carried out cruise studies for the northwest SCS in 2000 and 2005. The comparison studies[8,16,17] between satellite (SeaWiFS and Modisa) derived Chl-*a* data and *in situ* measurements show that satellite data are useful for verifying Chl-*a* concentration in this area.

The studies on spatial and temporal dissimilarities of Chl-*a* concentrations mingled with other environmental factors for this region are highly concerned with developing a better understanding of physical and biological processes along with existing bio-geochemical cycles. The present study focuses on the spatial distribution of Chl-*a* concentration during summer season for the entire SCS for a 5-year period and discusses its responses to environmental conditions linked with factors of sea surface temperature (SST), sea surface wind stress (SSWS), Ekman pumping and upwelling. Satellite data obtained from 1998 to 2003 have been analyzed to investigate interesting phenomena and related mechanisms.

2. Data and Analysis

The SCS is a marginal sea located in the west Pacific Ocean, lying in the tropical monsoon zone between the equator and the tropic of Cancer (Fig. 1). Our study focuses mainly on the western SCS with wide continental shelf in the south and north, and comparatively narrow continental shelf in the mid-west of the study area near Phan Ri Bay (PRB in Fig. 1), where the depth reaches 4000 m at its narrowest width of 2 km.

The Chl-*a* data acquired from SeaWiFS Version 4 has been used to derive the Chl-*a* estimates. Monthly Standard Mapped Image (SMI) Products (Level 3) (spatial resolution, $9 \times 9\,\mathrm{km}^2$) were procured from the Distributed Active Archive Center (DAAC) of Goddard Space Flight Center (GSFC), NASA (http://oceancolor.gsfc.nasa.gov/cgi/level3.pl) The summer Chl-*a* image averaged for June–August from 1998 to 2003 were produced with the help of Matlab Version 6.5 and Grid Analysis and Display System (GrADS) Version 1.8 software from monthly data sets.

The SST data derived from Advanced Very-High Resolution Radiometer (AVHRR) of Ocean Pathfinder channel-5 (spatial resolution 4 km/ month-daytime) was provided by Physical Oceanography Distributed Active Archive Center (PO.DAAC), Jet Propulsion Laboratory (JPL), NASA (http://podaac.jpl.nasa.gov/sst). The seasonal average SST images were generated by the means similar to SeaWiFS Chl-*a* data processing using Matlab and GrADS to show the spatial variations of SST during summer.

The wind stress data entitled, Tropical Indian Winds from 1970 to 2004 are obtained from the Center for Ocean-atmospheric studies of Florida State University (http://www.coaps.fsu.edu). The data is pseudo-stressed based on surface marine observations (TD-1129) for the years after 1980 produced by the National Climatic Data Center (NCDC) and for the years 1970–1979 they are based on the COADS CMR5 individual ship observations with a resolution of 1° grid, expressed in (m/s).[2]

3. Results

3.1. *Spatial distribution of Chl-a*

A relatively high concentration of Chl-*a* ($>0.13\,\mathrm{mg/m^3}$) is observed offshore of southeast Vietnam (oval area marked in Fig. 2(A)) compared with other locations, while the Chl-a in areas east of the SCS, north of Borneo and southwest of Luzon Island, display lower concentrations ($<0.1\,\mathrm{mg/m^3}$). Figure 2(A) also shows an extreme high band of Chl-*a* parallel to the

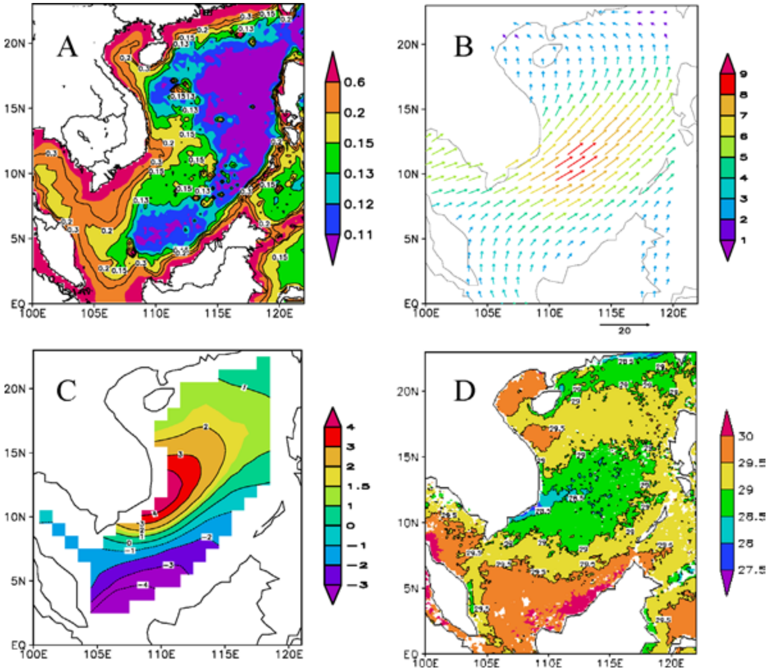

Fig. 2. (A) SeaWiFS-derived Chl-*a* (mg m^{-3}) images in summer for the SCS averaged for June–August from 1998 to 2003. (B) FSU SWS vectors and their magnitude (contours in 10^{-2} Nm^{-2}) for June–August from 1970 to 2003. (C) Summer Ekman Pumping velocity (upward positive in 10^{-6} m/s) derived from wind stress and averaged for June–August from 1970 to 2003 in the SCS. (D) Summer SST Image (in °C) averaged for June–August from 1998 to 2003 in the SCS.

coastline within a range of 200 km from the Mekong estuary to PRB. Furthermore, Fig. 2(A) also indicates a high Chl-*a* jet on the east side of PRB intruding as far as 116°E, and merging with the high chlorophyll bond parallel to the coastline.

3.2. *Spatial variability of prevailing winds and Ekman pumping velocity*

During summer, southwesterly winds are persistent in the SCS. Figure 2(B) displays the spatial distribution of wind stress for June–August. At about 11°N off Vietnam, the wind stress reaches maximum (approximately 0.09 Nm^{-2}), which is almost twice that of the ambient intensity. The southeast coast of Vietnam is oriented southwest to northeast, roughly parallel to the southwesterly winds. The axis of this wind seems to divide the SCS into two parts, with Ekman upwelling and downwelling in the north and south areas, respectively (Fig. 2(B)). The Ekman Pumping image (Fig. 2(C)) displays a strong upwelling tendency in the west basin southeast of Vietnam.

3.3. *Spatial variability of SST*

Figure 2(D) indicates that high temperatures prevail in most of the SCS (>29.5°C), while in the western SCS, low temperatures are obvious, in the shape of ellipse with a short radius of approximately 300 km to the southeast of Vietnam in the western SCS. This location matches roughly with the area of high positive Ekman pumping velocity, and especially a clearly defined lower jet-shape SST (<28.5°C) to northeast PRB.

4. Discussion

4.1. *Key factors limiting the growth of phytoplankton*

Generally, the availability of nutrients and light radiation are the key factors limiting the growth of phytoplankton. However, in the SCS light may not be a key factor because it is located in the tropics, whereas the accessibility of nutrients may perhaps be the determining factor.[8,18] The hydrological conditions in the study area are complex, varying with space and time, and the interaction between these factors must have had a considerable influence on the transport and distribution of nutrients in the study region, ultimately affecting the growth of phytoplankton. Hence, we place an emphasis on discussing important hydrological features influencing the distribution of Chl-*a* concentration in this study.

4.2. *The distribution of Chl-a and oceanic conditions*

In the southeastern offshore part of Vietnam, where high Chl-*a* concentration appears (oval-shape in Fig. 2(A)), intense Ekman Pumping upwelling (Fig. 2(C)) induced by positive SSWS (Fig. 2(B)) eddies will transport cold water from the sub-surface to surface layer, lowering SST (Fig. 2(D)) and increasing Chl-*a* concentration (Fig. 2(A)). The concept of Ekman Pumping velocity is seldom introduced in similar previous research. Our results (Fig. 2(A) and 2(B)) also show that high Chl-*a* concentration matches positive Ekman Pumping velocity and low SST (Fig. 2(D)) in terms of intensity, shape and location. The result may mean that the region of high Chl-*a* concentration is primarily induced by upwelled water with rich nutrients through Ekman pumping.

In the nearshore area to southeast Vietnam, the strong southwesterly wind stress (Fig. 2(B)) parallel to the coastline induces strong offshore Ekman transport, leading to coastal upwelling with low SST. In this region, well-defined coastal upwelling can be also identified in the SST image (Fig. 2(D)). By the intense Ekman upwelling associated with the strong influence of southwesterly winds, the upwelling east of Vietnam in the southwestern SCS may lead to conspicuous localized cooling of the area. The findings of Tang *et al.*[9,16] and Xie *et al.*[6] also revealed similar conditions in the same area under investigations. High Chl-*a* concentration may be a response to the upwelling in the coastal area. The band of high Chl-*a* concentration over the near-shore region in south Vietnam (south of PRB, in Fig. 1) coincides with the region of strong wind (Fig. 2(B)), with the band of low SST parallel to the coastline (Fig. 2(D)). Overall, by the mechanism of coastal upwelling in the near-shore area, offshore Ekman pumping transports cold water from the bottom to the surface and from the coast to offshore and thereby could induce the continuous supply of nutrients, low temperature and high Chl-*a* concentration.

In addition, in nearshore regions, another important factor for the sustenance of high Chl-*a* is attributed to the advantageous position of being close to the discharge waters of the Mekong River, which brings nutrients from upstream. Earlier investigations[19] revealed that there is a strong northeastward coastal current during the southwest monsoon, originating from shallow water in the southwest part of the SCS and the maximum runoff from the Mekong river along the Vietnamese coast (available: http://www.na.unep.net). This current turns into the northeast basin of the SCS near 11°N, forming an offshore jet in the northeast direction.[5] As a consequence, these conditions may also support a wide band of Chl-*a* in the coastal waters southeast of Vietnam and lead to a high Chl-*a* jet protruding into northeastern basin near PRB, as shown in Fig. 2(A).

5. Conclusions

This study revealed a high Chl-*a* concentrations in the western SCS during summer, also showing a larger spatial variation in the west than in the east owing to differences in oceanic conditions, especially the wind stress and Ekman pumping velocity. The high Chl-*a* concentration and the Chl-*a* jet in the western SCS are related to upwelling induced by southwesterly monsoon winds. A high coastal Chl-*a* band is sustained due to coastal upwelling derived from Ekman offshore transport of strong winds with lower temperature, while the high Chl-*a* in the western SCS basin is related to upwelling induced by wind stress.

Acknowledgements

The present research was supported by: a, "Major Project of Knowledge Innovation (No. KZCX3-SW-227-3)" funded by the Chinese Academy of Sciences (CAS); b, the National Natural Science Foundation of China (NSFC40576053); c, "One Hundred Talents Program" (Ybjh0403) of CAS; and d, "International Cooperation Program (Knowledge Innovation Group)" of CAS awarded to Professor DanLing TANG.

References

1. K. Wyrtki, *Scripps Institution of Oceanography* (La Jolla, CA, 1961), p. 195.
2. J. Pan, X.-H. Yan, Q. Zheng, W.-T. Liu and V. V. Klemas, *Remote Sens. Environ.* **84** (2002) 53.
3. W.-T. Liu and X. Xie, *Geophys. Res. Lett.* **26** (1999) 1473.
4. P.-T. Shaw and S.-Y. Chao, *Deep-Sea Res.* **41** (1994) 1663.
5. W.-D. Fang, P. Shi *et al.*, *J. Geophys. Res.* **107** (2002) 3202.
6. S.-P. Xie, Q. Xie, D. Wang and W. T. Liu, *J. Geophys. Res.* **108** (2003) C8001867.
7. D. L. Tang, I-H. Ni, F. E. Müller-Karger and Z. J. Liu, *Cont. Shelf Res.* **18** (1998) 1493.
8. D. L. Tang, H. Kawamura, M. A. Lee and V. Y. Dien, *Remote Sens. Environ.* **85** (2003) 475.
9. D. L. Tang and H. Kawamura, Tran Dien and Ming An Lee, *Mar. Ecol. Prog. Ser.* **268** (2004) 31.
10. S. L. Shang, C. Y. Zhang, H. S. Hong *et al.*, Deep-Sea Res., II: *Tropical Studies in Oceanography* **51** (2004) 11113.
11. D. L. Tang, I-Hsun Ni and Dana R. Kester, *Mar. Ecol. Prog. Ser.* **191** (1999) 43.
12. T. C. Hung, C. C. H. Tsai, S. H. Wu *et al.*, *Acta Oceanogr. Taiwanica* **16** (1984) 8.
13. Y. L. Lee Chen, Houng-Yung Chen *et al.*, *Continental Shelf Research* **24** (2004) 527.
14. N. S. R. Agawin, C. M. Duarte, S. Agusti *et al.*, *Estuarine, Coastal and Shelf Science* **56** (2003) 493.
15. Chen Chu-qun, Shi Ping and Mao Qing-wen, *Journal of Tropical Oceanography* **20** (2001) 66.

16. D. L. Tang, H. Kawamura, H. Doan-Nhu and W. Takahashi, *J. Geophys. Res.* **109** (2004b) C03014, doi: 10. 1029/2003J C 002045.
17. H. Zhao and D. L Tang, *Journal of Tropical Oceanography* **24** (2005) 27–31 (in Chinese).
18. N. T. An and H. T. Du, *Proceedings of the SEAFDEC Seminar on Fishery Resources in the South China Sea Area IV: Vietnamese Water*. Thailand: Southeast Asian Fisheries Development Center, Vol. 1, 2000.
19. L. Li, *Journal of Oceanography in Taiwan Strait* **21** (2002) 114.

A PRELIMINARY ANALYSIS OF THE INFLUENCE OF SUMATRAN TSUNAMI ON INDIAN OCEAN CHL-*a* AND SST

DANLING TANG[†,*], B. SATYANARAYANA[†], HUI ZHAO[†]
and R. P. SINGH[‡]
[†]*Laboratory for Tropical Marine Environmental Dynamics*
South China Sea Institute of Oceanology
Chinese Academy of Sciences
Guangzhou-510301, P. R. China
[‡]*Department of Civil Engineering, Indian Institute of Technology*
Kanpur-208016, India
**lingzistdl@126.com*

The massive earthquake off the northern Sumatran coast (Indonesia) on December 26, 2004 produced the largest trans-oceanic tsunami. Besides landform destruction and changes, the alterations produced the phenomena of aquatic environments, highlighting that ecosystem responses are also important. In this paper, we present pre- and post consequences of the tsunami on spatial and temporal distribution of Chlorophyll-*a* (Chl-*a*), the vital element of marine ecosystem and primary production. Our analysis based on satellite data (MODIS) indicated that levels of Chl-*a* increased prior (December 2–22) to the tsunami, and dispersed afterwards along with the drift of current. The time-series data (daily and 8-day intervals) between 2002 and 2005 (October–January) also revealed a similar trend and indicated an inverse relationship between Chl-*a* and Sea Surface Temperature (SST). Further detailed analyzes have shown that the distribution of Chl-*a* is influenced also by other environmental factors such as wind, upwelled water and circulation in the Indian Ocean.

1. Introduction

The term "tsunami" is used to describe a series of waves that travel across the ocean with exceptionally long wavelengths.[1,2] The case in this study was a subduction[3] earthquake on December 26, 2004 off the northern Sumatran coast (Indonesia).[4–6] According to United States Geological Survey (USGS),[7] the epicentre of earthquake was located near 3.3°N, 95.95°E with a magnitude of 9.0 and focal depth of 10 km at 00:58:53 UTC. It was presumed that approximately a trillion tonnes of water was displaced and driven towards Southeast Asia's coastline in long, low amplitude waves travelling up to 900 km/h.[8] Although, the velocity of waves slows down when approaching the shallow region of coastlines, their height increases to as high as 30–50 m and strikes the shore with a devastating force.[9–12]

Apart from land related changes, issues like changes in the ocean related to sea level rise, transfer of materials from land to sea and vice versa, biodiversity and biological productivity are also important. Earthquakes can induce sudden changes in the ocean-atmosphere interaction, for which the consequences in terms of anomalous behavior of numerous oceanic and atmospheric parameters are believed to show precursory signals.[13,14] However, only very few studies have been carried out pertinent to tsunami and ocean Chlorophyll associated with phytoplankton, possibly due to less number of such incidents. Taking advantage of satellite data, we have made an attempt to address some of these concerns.

2. Materials and Methods

2.1. *Study area*

The sea surface area extending between 5° to 25°N and 75° to 105°E, adjoining Southeast Asian countries was investigated (Fig. 1). To cover with the consequences of the tsunami, time-series data for Chl-*a* and SST were also examined from an area close to the epicenter of the earthquake. While daily information on Chl-*a* was extracted from 4.5° to 7.5°N and 93° to 96°E (box-X with checks on December 26–31, 2004, Fig. 1(A)), the 8-day average (Chl-*a* and SST) covers the area from 3° to 9°N and 90° to 96°E (box-Y on December 26–31, 2004, Fig. 1(A)).

2.2. *Satellite data*

Chlorophyll-*a* (level-3) data observed from Moderate Resolution Imaging Spectroradiometer (MODIS) onboard the Aqua of Earth Observing System (EOS) was obtained from the Ocean Color Web (http://oceancolor.gsfc.nasa.gov) at daily and 8-day intervals (spatial resolution 9 km), between 2002 and 2005 (October–January). Discontinuity of information was encountered in both cases due to missing values for several days (i.e. 22 in daily and eight days in weekly datasets). The data was processed through logarithm (log 10) transformation using Matlab and GrADS Version 1.8 (Grid Analysis and Display System) software.

Microwave optimally interpolated SST data (daily/resolution, 25 km) was acquired from Remote Sensing Systems (http://remss.come.sst).

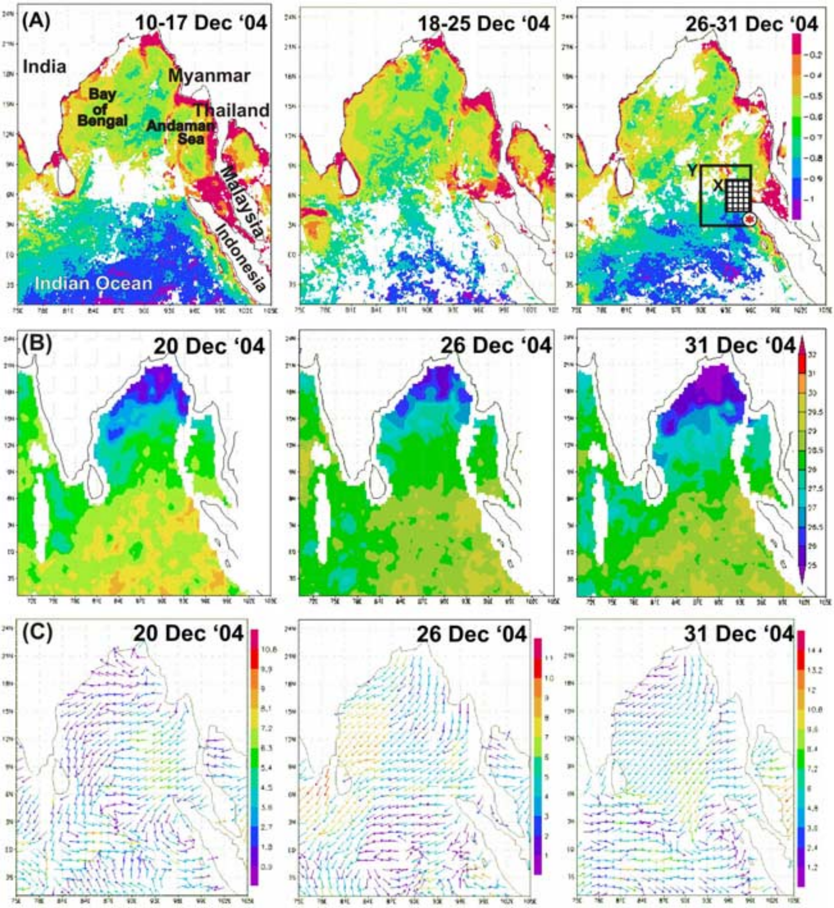

Fig. 1. (A) Distribution of Chl-*a* (mg m^{-3}) in Indian Ocean (December, 2004). The epicenter of earthquake is marked with red star on December 26–31, image. Boxes (X & Y) near the epicenter denote the regions for which time series data of Chl-*a* and SST were examined. (B) Variations in Sea Surface Temperature (SST) ranged between 25 and 32°C. (C) Wind speed and direction. The intensity of wind (m/s) represented by color bar in each panel, increased from 0.9–10.8 (December 20) to 1–11 (December 26) followed by 1.2–14.4 (December 31).

Daily information on level-3 QuikScat sea surface winds (m/s) (resolution 25 km) was obtained via the Physical Oceanography Distributed Active Archive Center (PO.DAAC) of the Jet Propulsion Laboratory, NASA (http://podaac.jpl.nasa.gov).

3. Results and Discussion

3.1. *Variability of Chl-a*

Spatial and temporal variability of Chl-*a* may occur due to large scale disturbances in the ocean circulation patterns, derived from sudden changes of thermal structure[15] of the water. Very few articles in the literature available on earthquakes and ocean productivity indicated that concentration of Chl-*a* rises particularly before the occurence of earthquake events.[16] It is noteworthy that present observations also show the tendency of increasing Chl-*a* from the second week of December (December 10–17, 2004, Fig. 1(A)) which continued throughout the third week (December 18–25, 2004, Fig. 1(A)), while dispersing to its maximum extent in the fourth week (December 26–31, 2004, Fig. 1(A)). In this context, the increased Chl-*a* may be associated with upwelled water and also thermal energy released from the point of earthquake, which can alter the *in situ* thermal structure of the water. Moreover, plankton in the coastal waters of Southeast Asian countries, for example, along the east coast of India and around Sri Lanka, is significantly diluted and diffused by the action of the giant waves. This could be the reason for dispersed/increased levels of Chl-*a* in the Bay of Bengal and the Andaman Sea soon after the disaster (Fig. 1(A)).

3.2. *Changes of SST*

The variations in SST following the tsunami are evident (Fig. 1(B)). The high surface temperature (29–30°C) before (December 20, Fig. 1(B)) the earthquake decreased to 28–29°C on the day of the tsunami (December 26, Fig. 1(B)). Further lowering of SST (27–28°C) was exclusively observed along the east coast of India in the Bay of Bengal (December 31, Fig. 1(B)). The area close to the epicenter of the earthquake was however indicating warm water conditions, namely, SST ranging between 29°C and 30°C, with only a small change of 0.5–1.0°C prior to and after the event, probably due to the release of thermal energy.[17] When wind speed is considered (Fig. 1(C)), mostly northeast winds prevailed accompanying the winter monsoon (November–February). On December 20, the wind speed reached 5.0 m/s covering most of the study area and reached a peak of 10 m/s on December 26 on the southeast coast of India and Sri Lanka, where severe damage was reported from the States of Tamil Nadu and Andhra Pradesh (India) and all around Sri Lanka. The high Chl-*a* together with low SST and high wind speed was evident at the time of observation.

3.3. *Time-series analysis*

Further analysis was carried out using time-series data for Chl-*a* and SST between 2002 and 2005 for October to January (Fig. 2). Based on daily data (Fig. 2(A)), the Chl-*a* values increased close to the time of the earthquake (up to 0.69 mg m^{-3} on December 22, 2004), and soon after fluctuations occurred with a series of aftershocks. Nevertheless, the Chl-*a* concentrations were appreciably higher during the period of the disaster than that for other years (Fig. 2(B)).

While Chl-*a* increased evidently from 3 to 10 December and attained a peak value of 0.35 mg m^{-3} between 19 and 26 December (Fig. 2(B)), it decreased to 0.33 mg m^{-3} between 27 and 31 December 2004. A further decrease to 0.25 mg m^{-3} occurred through the period January 1–8, 2005. The differences in Chl-*a* values between the higher daily averages compared to the lower 8-day averages are due to the effect of smoothing. Figure 2(C) shows inverse relationship between SST and Chl-*a*.

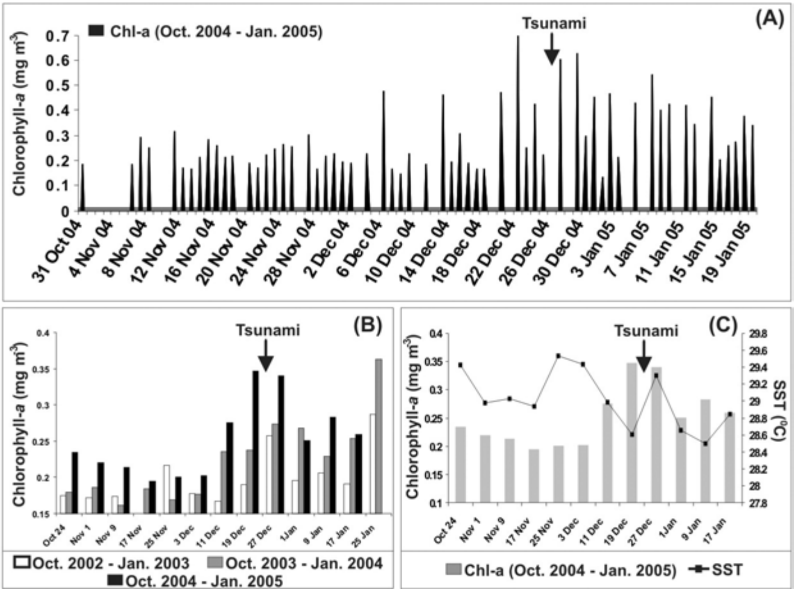

Fig. 2. (A) Daily concentrations of Chl-*a* (from box-X in Fig. 1(A)). (B) Comparison of Chl-*a* (8-day average) between the three years (2002–2005) (from box-Y in Fig. 1(A)). (C) Chl-*a* and SST (8-day average) between October 2004 and January 2005 (from box-Y in Fig. 1(A)). The date of the tsunami is indicated by the downward pointing arrow in all panels. Discontinuity in Fig. 2(A) is due to missing values in daily coverage.

4. Summary

The results indicate the persuasiveness of the Boxing Day tsunami on the marine ecosystem and ultimately on the productivity of the Indian Ocean. Together with thermal energy, nutrients were brought from below the surface by upwelled water and facilitated the growth of phytoplankton. The drift of Chl-a is obvious at times by the action of the giant waves produced and this is also responsible for the low Chl-a along the east coast of India and around Sri Lanka. It is thought that these waves that reached land were highly contaminated by sludge and other wastes that, in turn, caused a strong effect on water quality and biota of coastal as well as offshore environments. However, the post-consequences following such a tsunami are so catastrophic to the natural ecosystem that loss estimates and rate of recovery times are difficult to calculate.

Acknowledgments

This work was support by the National Natural Science Foundation of China (CNSF40576053), Research Foundation (KZCX3-SW-227-3) from Chinese Academy of Sciences (CAS) and 'One Hundred Talents Program' (Ybjh0403) of CAS awarded to Professor DL TANG. The post-doctoral fellowship of CAS awarded to Dr. Satyanarayana (No. 2005037619) has contribution to this study.

References

1. A. G. Dawson, P. Lockett and S. Shi, *Environ. Int.* **30** (2004) 577.
2. E. Bryant, *Nature* **415** (2002) 469.
3. W. Hopkin, *Nature* **433** (2005) 3.
4. H. Kanamori, *Annu. Rev. Earth Planet. Sci.* **14** (1986) 293.
5. S. L. Bilek and T. Lay, *Nature* **400** (1999) 443.
6. H. Houston, *Nature* **400** (1999) 409.
7. USGS, *http://earthquake.usgs.gov/eqinthenews/2004/usslav* (2004).
8. E. Marris, *Nature* **433** (2005) 3.
9. D. Cyranoski, *Nature* **425** (2003) 649.
10. J. J. Clague, P. T. Bobrowsky and I. Hutchinson, *Quat. Sci. Rev.* **19** (2000) 849.
11. F. Nanayama *et al.*, *Nature* **424** (2003) 660.
12. T. K. Pinegina, J. Bourgeois, L. I. Bazanova, I. V. Melekestsev and O. A. Braitseva, *Quat. Res.* **59** (2003) 36.
13. S. Dey and R. P. Singh, *Nat. Haz. Earth Sys. Sci.* **3** (2003) 1.
14. S. Dey, S. Sarkar and R. P. Singh, *Advances in Space Research* **33** (2004) 274.
15. N. Chaturvedi and A. Narain, *Int. J. Remote Sens.* **24** (2003) 511.
16. R. P. Singh, S. Bhoi and A. K. Sahoo, *Int. J. Remote Sens.* **23** (2002) 3123.
17. D. Ouzounov and F. Freund, *Advances in Space Research* **33** (2004) 268.

POTENTIAL FOR SULFIDE MINERAL DEPOSITS IN AUSTRALIAN WATERS

TIMOTHY F McCONACHY
Commonwealth Scientific and Industrial Research Organisation
Division of Exploration and Mining, P.O. Box 136, North Ryde
New South Wales 1670, Australia
Tim.McConachy@csiro.au

The world is witnessing a paradigm shift in relation to marine mineral resources. High-value seafloor massive sulfides at active convergent plate boundaries are attracting serious commercial attention. Under the United Nations Convention on the Law of the Sea, maritime jurisdictional zones will increase by extending over continental margins and ocean basins. For Australia, this means a possible additional 3.37 million km^2 of seabed. Australia's sovereign responsibility includes, amongst other roles, the management of the exploitation of nonliving resources and sea-bed mining. What, therefore, is the potential in Australia's marine jurisdiction for similar deposits to those currently attracting commercial attention in neighboring nations and for other types/styles of sulfide deposits? A preliminary review of opportunities suggests the following: (i) volcanogenic copper–lead–zinc–silver–gold mineralization in fossil arcs and back arcs in eastern waters Norfolk Ridge and the Three Kings Ridge; (ii) Mississippi Valley-type lead–zinc–silver mineralization in the NW Shelf area; (iii) ophiolite-hosted copper mineralization in the Macquarie Ridge Complex in the Southern Ocean; and (iv) submerged extensions of prospective land-based terranes, one example being offshore Gawler Craton for iron oxide–copper–gold deposits. These areas would benefit from pre-competitive surveys of detailed swath bathymetry mapping, geophysical surveys, and sampling to help build a strategic inventory of future seafloor mineral resources for Australia.

1. Introduction

Submarine deposits of massive sulfides are attracting commercial attention by exploration and mining companies. This is mainly due to their high concentrations of gold, copper, zinc, and silver.[1–3] These submarine mineral deposits are no longer scientific curiosities, but are potential new sources of metals in their own right. This marks a paradigm shift to commercially driven exploration. As is the case for mining mineral deposits on land, a sustainable-licence-to-mine the seafloor will be also critically important; and in this respect fossil "black smokers", devoid of living chemosynthetic vent fauna and abundant biodiversity, may offer more suitable targets for sustainable commercial exploitation. It also means that fossil deposits in other geological settings on the seabed may warrant attention in the future.

The aim of this contribution is to provide an initial analysis of conceptual prospectivity within Australia's seabed for sulfide mineral deposits. While the analysis is not exhaustive, it is hoped that it might act as a catalyst to initiate surveys utilizing detailed swath bathymetric mapping, side scan sonar imagery, geophysical methods such as magnetics, gravity and resistivity, dredging and coring to test various hypotheses and if successful, ultimately increase Australia's inventory of seabed mineral resources.

2. Setting of Seafloor Massive Sulfide Deposits

Since the discovery of "black smokers" at 21°N on the East Pacific Rise in the late 1970s,[4] research-driven exploration has discovered mineral deposits actively forming at hydrothermal vents related to submarine volcanism in every major ocean basin and divergent plate margin on Earth.[5,6] Sites of equivalent activity at convergent plate margins such as those found in island arcs and backarcs are well documented, particularly in the western and southwestern Pacific region, for example, at Sunrise in the Izu-Bonin arc south of Japan, at PACMANUS in the Manus back arc of Papua New Guinea and along the Kermadec arc in New Zealand.[7–9]

If Australia's recent lodgment of revised maritime boundaries with the UN Commission on the Limits of the Continental Shelf in November 2004 is accepted, it will have one of the world's largest maritime jurisdiction of 14.41 million km^2, or slightly more than half the total land area[10] (Fig. 1). Accordingly, Australia has a commitment to manage this jurisdiction, including nonliving resources such as seabed mineral resources. Although no active spreading centres or associated sulfide mineral deposits are presently known within its maritime boundaries, this does not mean that sulfide deposits are absent on or in Australia's seabed.

In the following sections, geological settings are examined which are considered to have potential to host certain types of sulfide deposits. Submerged extensions of mineralized land terranes are considered as well.

3. Fossil Island Arcs and Back Arcs

The SW Pacific consists of a number of remnant and active back-arc basin and volcanic arc systems which formed as a consequence of Australia-Pacific plate convergence commencing in late Cretaceous and continuing to the

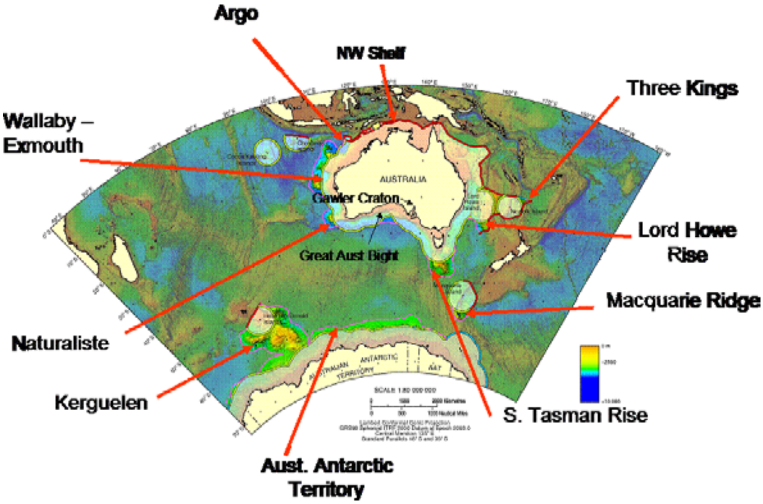

Fig. 1. Australia's maritime boundaries showing the areas of extended continental shelf submitted to the UN Commission on the Limits of the Continental Shelf in November 2004,[10] and some areas of sulfide prospectivity.

present.[11–13] Plate reconstructions and palaeo-age grids for the Western Pacific margin illustrate a number of back-arc basins associated with active and remnant volcanic arcs systems including Norfolk Ridge, Loyalty-Three Kings Ridge, Lau-Colville Ridge, and the Tonga-Kermadec Ridge.[14,15]

By comparison with modern volcanic arc and back arc systems, the Norfolk Ridge and Loyalty-Three Kings Ridge arc-back arc systems in eastern Australian waters have potential to host submarine Cu–Zn–Au–Ag massive sulfide deposits. Further work incorporating tectonic models and observational constraints into 3D mantle convection models is providing important predictive tools for mineral exploration.[14,15] Zones of reduced magnetization-often associated with volcanogenic massive sulfide hydrothermal systems[16] are potential geophysical footprints with which to explore for massive sulfides in this area.

4. Mississippi Valley-Type Deposits

Like volcanogenic copper–zinc deposits, Mississippi Valley-type lead–zinc-deposits are also an important class of base metal deposit.[17] Most occur in orogenic foreland settings. Bradley and Leach[18] have examined deposits in collisional forelands and suggest that, tectonically, the passive foreland carbonate shelf environment of the Banda Arc collision zone off NW Australia is a good modern analogue for Mississippi Valley-type mineralization, and in particular the best modern example is the emergent forebulge of the Kepulauan Aru (Aru Islands) in neighboring Indonesia. Other lines of evidence support this hypothesis. For example, recent work[19] has recognized significant natural hydrocarbon seeps (methane plumes and associated tube worms, some of which are coated with manganese carbonate) on the seafloor on the Yampi Shelf and Arafura Sea. These seeps are considered strong evidence for an active petroleum system in this area.[19] Hydrocarbons such as bitumen are common accessory materials in Mississippi Valley-type lead–zinc deposits and provide a link between petroleum and base metal sulfide formation. Further survey work in NW Australian waters is required to assess base metal potential.

A cruise (GABSEEPS, FR01/2001)[20] along the edge of the Great Australian Bight tested the hypothesis for Mississippi Valley-type lead zinc mineralization, and possibly also for a form of uranium mineralization associated with hydrothermal "warm seeps" venting basin brines or fluids rising up faults from basement.[20] It was anticipated that such sites might host mineral-rich deposits, or that the vent fluids might have compositions implying operation of subsurface ore-forming processes. Even though no evidence of hydrothermal seepage or associated deposits was found, investigations of this nature can yield important results for future science and expedition planning.

5. Ophiolite-Hosted Copper

A major strike slip fault marks the boundary between the Australian and Pacific plates via the Alpine Fault in South Island New Zealand and extending SW to Macquarie Island, approximately 1500 km SSE of Tasmania in the Southern Ocean. This fault marks the only active plate boundary within Australia's marine jurisdiction. A triple junction to the south of Macquarie Island links the Macquarie Ridge Complex with the Southeastern Indian Ridge and the Pacific-Anatarctic Ridge. Uplifted blocks of oceanic crust formed at the Australia-Pacific spreading center between 12 and 9 Ma are exposed on World Heritage Listed Macquarie Island.[21,22] This structurally dismembered ophiolite exposes pillow basalt, sheeted dykes, gabbro and peridotite; and preserves many primary seafloor and sub seafloor features such as rift-related and transfer-related structures at the fossil spreading ridge system. These structures acted as conduits for hydrothermal fluids and host enclaves of vein stockworks, hydrothermal quartz–pyrite–epidote breccias and small pods of massive sulphide consisting of mostly pyrite and traces of chalcopyrite.[23,24]

It is likely that similar styles of mineralization and other styles not yet considered could be exposed on the seafloor in the Macquarie Ridge Complex which remains under explored due to its remote location and challenging sea conditions. The Hjort Trench, south of Macquarie Island is noteworthy for being the deepest point in Australia, around 6700 m below sea level.

6. Off Shore Extensions to Mineralized Land Terranes

Clues for off shore prospectivity and mineralization can also be gained from examination of the distribution of mineralization on Australia's land mass. For example, the Australian land mass hosts around 40,000 mineral occurrences in rocks ranging in age from Achaean to Mesozoic. Figure 2 shows occurrences of base metal (excluding nickel) and a number of the major base metal operating mines which are significant contributors to Australia's GDP. This pattern and distribution of mineral occurrences evident in Fig. 2 essentially outlines the major exposed geological terranes in Australia. Based on magnetics and gravity data a number of these terranes extend into the offshore environment.

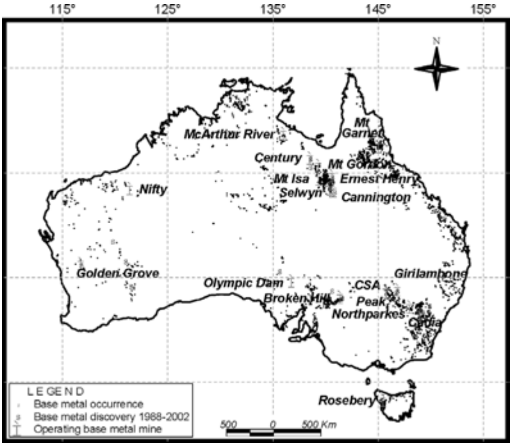

Fig. 2. Location of base metal mines and base metal occurrences (excluding nickel) in Australia.[27–29]

The Gawler Craton in South Australia is one such example of a mineral-rich geological terrane that extends offshore. The Gawler Craton hosts the giant Olympic Dam orebody, an important source for copper (and gold and uranium).[25] Although not a massive sulfide deposit *sensu stricto*, there has been significant land-based exploration in the Gawler Craton for deposits of its class, so called iron oxide–copper–gold deposits. Off shore exploration has included drilling of magnetic and gravity features below relatively shallow water ($<$5–10 m) in Spencer Gulf but so far without success.[26]

7. Conclusions

Growing commercial activity for high value seafloor massive sulfides in neighboring countries such as Papua New Guinea and New Zealand may lead companies to focus their attention on fossil sulfide deposits in Australian waters. With pending changes to maritime boundaries, Australia will have one of the largest maritime jurisdiction in the world, but its extensive seabed is grossly under explored with respect to mineral resources generally, and metallic sulfides in particular.

An initial analysis of sulfide mineral potential in Australian water indicates a number of possible areas of prospectivity, and include the following:

(1) Volcanogenic copper–lead–zinc–gold–silver mineralization associated with fossil volcanic arcs and back arcs in eastern Australian waters, including Norfolk Ridge, Lord Howe Rise and Three Kings Ridge.
(2) Mississippi Valley–type lead–zinc–silver mineralization in the NW Shelf area.
(3) Ophiolite-hosted copper mineralization associated with the major strike slip fault in the Macquarie Ridge Complex.
(4) Submerged extensions of prospective land based terranes, for example, the iron oxide–copper–gold potential in the Gawler Craton, South Australia. It is a reasonable assumption that a similar pattern of mineral occurrences and more significant deposits would be found offshore, if exploration were to proceed in that environment.

Prospective terranes for other styles of mineralization also extend offshore and offer potential for new mineral discoveries in the future. The areas highlighted in this contribution would benefit from pre-competitive surveys utilizing detailed swath bathymetry mapping, and other appropriate search techniques such as side scan sonar, detailed magnetics and gravity and “ground truthing” by dredging, grabs and sediment coring.

Acknowledgments

The idea for this paper germinated during a CSIRO Wealth from Oceans Natural Research Flagship hosted workshop on seabed minerals in Sydney and at AOGS in Singapore.[30,31] Bill McKay, Phil Symonds, Jim Colwell, Yanis Miezitis, and Ron Sait of Geoscience Australia are thanked for discussions regarding Australia's maritime jurisdiction. Terry Briggs brought attention to modern Mississippi Valley-type analogues by other researchers.

References

1. D. Heydon, in *Seabed Hydrothermal Systems of the Western Pacific: Current Research and New Directions*, ed. C. J. Yeats (CSIRO Exploration and Mining Report 1112R, 2003), pp. 79–80.
2. D. Heydon, in *Seabed Hydrothermal Systems of the Western Pacific: Current Research and New Directions*, ed. C. J. Yeats (CSIRO Exploration and Mining Report 1112F, 2003a), pp. 84–86.
3. M. D. Johnston, in *Deep Blue Minerals — Towards a Sustainable Marine Minerals Industry: Extended Abstracts*, eds. C. J. Yeats and T. F. McConachy (CSIRO Exploration and Mining Report P2005/135, 2005), p. 19.
4. J. M. Edmond, C. Measures, B. Grant, F. R. Sclater, R. Collier, A. Hudson, L. I. Gordon and J. B. Corless, *Earth Planet Sc. Lett.* **46** (1979).
5. H. N. Edmonds, P. J. Michael, E. T. Baker, D. P. Connelly, J. E. Snow, C. H. Langmuir, H. J. B. Dick, R. Muehe, C. R. German and D. W. Graham, *Nature* **421** (2003) 6920.
6. P. Stoffers, T. Worthington, R. Hekinian, S. Petersen, M. Hannington, M. Tuerkay and F/S Sonne 157 Shipboard Scientific Party, *EOS*, *Trans. Amer. Geophys. Union* **83** (2002) 28.
7. R. A. Binns and S. D. Scott, *Econ. Geol.* **88** (1993).
8. K. Iizasa, R. S. Fiske, O. Ishizuka, M. Yuasa, J. Hashimoto, J. Ishibashi, J. Naka, Y. Horii, Y. Fujiwara, A. Imai and S. Koyama, *Science* **283** (1999) 5404.
9. C. E. J. de Ronde, E. T. Baker, G. J. Massoth, J. E. Lupton, I. C. Wright, R. A. Feely and R. R. Greene, *Earth Planet Sc. Lett.* **193** (2001).
10. J. B. Colwell and P. A. Symonds, in *Deep Blue Minerals — Towards a Sustainable Marine Minerals Industry: Extended Abstracts*, eds. C. J. Yeats and T. F. McConachy (CSIRO Exploration and Mining Report P2005/135, 2005), pp. 3–8.
11. D. E. Karig, *J. Geophys. Res. Solid. Ea.* **76** (1971).
12. S. Uyeda and H. Kanamori, *J. Geophys. Res. Solid. Ea.* **84** (B3) (1979).
13. P. Clift, in *Active Margins and Marginal Basins of the Western Pacific*, eds. B. Taylor and J. Natland (American Geophysical Union, Washington D.C., 1995), pp. 67–96.
14. M. Sdrolias, R. D. Müller and C. Gaina, in *The Evolution and Dynamics of the Australian Plate*, eds. R. Hillis and R. D. Müller (Geological Society of

Australia Special Publication 22 and Geological Society of America Special Paper 372, 2003), pp. 343–359.

15. M. Sdrolias and R. D. Müller, in *Deep Blue Minerals — Towards a Sustainable Marine Minerals Industry: Extended Abstracts*, eds. C. J. Yeats and T. F. McConachy (CSIRO Exploration and Mining Report P2005/135, 2005), pp. 37–39.
16. M. A. Tivey, P. A. Rona and H. Schouten, *Earth Planet. Sci. Letts.* **115** (1993).
17. S. R. E. Penny, R. M. Allen, S. Harrison, T. C. Lees, F. C. Murphy and A. R. Norman, *T. I. Min. Metalli. B.* **113** (2004) B171–B182.
18. D. C. Bradley and D. I. Leach, *Miner. Deposita.* 38 (2003).
19. N. Rollet and G. A. Logan, *Petroleum Exploration Society of Australia News*, June/July, 2005.
20. R. A. Binns, Cruise Summary RV Franklin FR01/01 (GABSEEPS Cruise), CSIRO Report Number P2005/137 (2001).
21. P. Boyer, *Australian Antarctic Magazine* **3** (2002).
22. P. A. Rivizzigno and J. A. Karson, *Geology* **32**, 2 (2004).
23. S. Lewis and G. J. Davidson, *Proceedings of the 17th Australian Geological Convention, Hobart, Tasmania*, Australia, Feb. 8–13, Abstracts, Geological Society of Australia, 73, 2004, p. 216.
24. N. Daczko, K. Wertz, S. Mosher, M. Coffin and T. Meckel, *Proceedings of the 17th Australian Geological Convention*, Hobart, Tasmania, Australia, Feb. 8–13, Abstracts, Geological Society of Australia, 73, 2004, p. 202.
25. J. S. Reeve, K. C. Cross, R. N. Smith and N. Oreskes, in *Geology of Mineral Deposits of Australia and Papua New Guinea*, ed. F. E. Hughes (The Australasian Institute of Mining and Metallurgy, Melbourne, 1990), pp. 1009–1035.
26. W. J. McKay, Y. Miezitis, N. F. Exon and R. Sait, in *Deep Blue Minerals — Towards a Sustainable Marine Minerals Industry: Extended Abstracts*, eds. C. J. Yeats and T. F. McConachy (CSIRO Exploration and Mining Report P2005/135, 2005), pp. 9–14.
27. T. F. McConachy and B. I. A. McInnes, in *Copper Zinc Massive Sulphides in Western Australia*, eds. T. F. McConachy and B. I. A. McInnes (CSIRO Explores 2 Series, 2004), pp. 131–149.
28. G. R. Ewers and N. Evans (B. Kilgour, compiler), *MINLOC Mineral Localities Database* (Digital Dataset, 2001).
29. G. R. Ewers, N. Evans and M. Hazell (B. Kilgour, compiler), *OZMIN Mineral Deposits Database* (Digital Datasets, 2002).
30. C. J. Yeats and T. F. McConachy (eds.) *Deep Blue Minerals — Towards a Sustainable Marine Minerals Industry: Extended Abstracts* (CSIRO Exploration and Mining Report P2005/135, 2005), p. 63.
31. T. F. McConachy, Abstract, *Joint 2nd Asia Oceania Geosciences Society (AOGS) Conference*, June 20–24, Singapore 58-OA-A3027, 2005.

LOCAL TO LONG-RANGE DUST TRANSPORT OVER CENTRAL EASTERN AUSTRALIA

MILTON S. SPEER*,‡ and LANCE M. LESLIE†,§
Bureau of Meteorology, Sydney, Australia
†*School of Meteorology, The University of Oklahoma, Norman, OK, USA*
‡*mss@lighthill.maths.unsw.edu.au*
§*lmleslie@ou.edu*

A climatology of dust reporting days from 1995 to February 2004 has been prepared for the central eastern Australia region. The climatology reveals a total of 55 "dust days," consisting of 43 dust days associated with fronts. Of these 24 were classified as being embedded in the zonal westerlies in the Great Australian Bight (GAB) or in westerlies produced by from low-pressure systems in the GAB. The remaining 19 were associated with fronts over eastern Australia where high pressure systems in the GAB generated postfrontal south to southeast winds. Two case studies of dust storm generation and transport were modeled using an integrated wind erosion prediction system. The model predictions were broadly consistent with both satellite images highlighting dust and with the synoptic observations that reported dust.

1. Introduction

The *local* or *long*-range transport of dust by wind erosion, events most commonly referred to as dust storms (in some regional areas they are called dust devils), are a regular occurrence over much of central eastern Australia. McTainsh and Pitblado[1] showed that annual dust storm frequencies over Australia for the period 1957–1984 can be as high as 5–10 times per year in some areas. Ekström *et al.*[2] divided Australian dust storms into two groups with distinct dust storm seasons, namely, spring–summer (September–February), and summer–autumn (December–May). Dust storms can be further subdivided into two types; those that result in the local dust transport and those that produce long-range dust transport. Local dust transport typically occurs over periods ranging from a few minutes to a few hours as a result of short-lived, extreme wind speeds generated from thunderstorms or dust devils.

Long-range dust transport occurs on longer time scales and on spatial scales ranging from hundreds to thousands of kilometres usually with the passage of a frontal system. In these prolonged dust storm episodes wind erosion can have a dramatic effect on the air quality in regions downstream of the dust sources, reduce the quality of the topsoil, play an important role in the global dust cycle and disrupt social and economic activities. In this study we focus on long-range dust transport, over the period from 1995 to 2005, using dust reports at Australian Bureau of Meteorology synoptic reporting stations (see Fig. 1) over central eastern Australia. The main meteorological characteristics of long-range dust transport, particularly, in data sparse areas of Australia are best investigated using an integrated wind erosion assessment and prediction scheme. Limitations of the synoptic network include the small number, clustering of stations, infrequent sampling, and the fact that estimates of visibility are subjective.

The three-dimensional (3D) weather variables of wind speed and direction, temperature, and moisture are observed routinely once per day, but

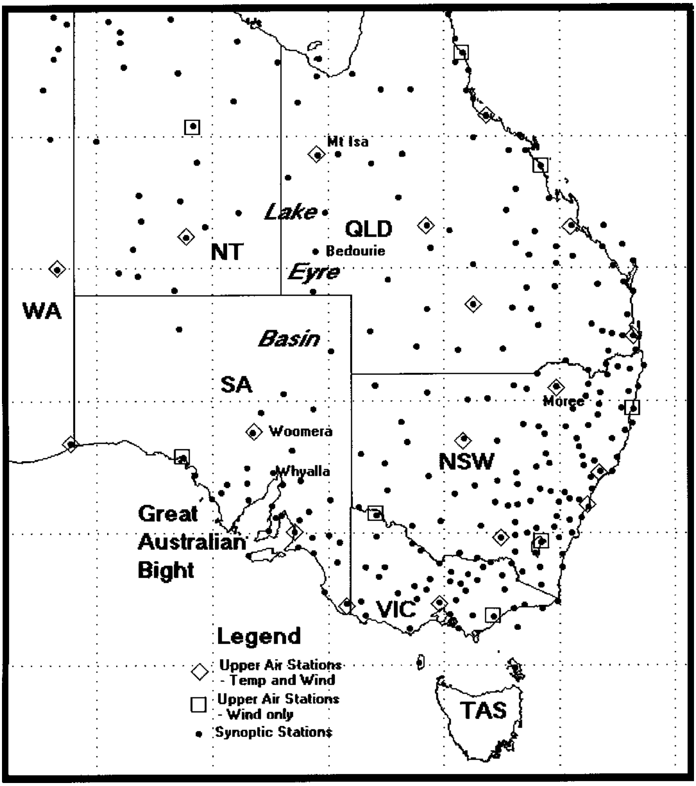

Fig. 1. Map of central eastern Australia showing synoptic reporting stations (thinned around the coastline), upper air stations and place names mentioned in the text.

only at a few locations scattered around Australia. In this study we use a land-surface scheme, a wind erosion scheme and a transport-deposition scheme, all of which are coupled. In turn, this system is supported by a comprehensive GIS database that is continuously updated with the latest available land–surface data. The original system, developed and tested by Shao and Leslie,[3] has been greatly extended by Lu and Shao,[4] and Shao *et al.*[5] The system recently has been adapted for operational use by the National Meteorological Centre of the Chinese Meteorology Agency to provide routine daily numerical forecasts of dust storm weather. This was the first real-time application of a coupled numerical weather prediction-soil erosion and system.[6]

The main aims of our present study are as follows. First, we describe the data and climatology. Second, we outline the integrated wind erosion modeling system that provides predictions of dust concentration by simulating dust particle entrainment, transport, and deposition. The integrated prediction system used here is based on the HIRES numerical weather prediction (NWP) model developed by the second author,[7] which is coupled with the wind erosion model of Shao and Leslie,[3] Lu and Shao,[4] and Shao *et al.*[8] The integrated system enables us to differentiate between the major meteorological factors that determine long-range dust transport. Two recent dust storm events are studied in detail. They occurred in the same seasonal period (spring–summer) and affected the same central-eastern areas of Australia, which lie in the spring-summer dust storm group delineated by Ekström *et al.*[2]

Third is a brief synoptic description of the case studies. The emphasis here is in determining the main synoptic differences of the events rather than focusing on their detailed mesoscale meteorological development and structure. The main numerical model outputs are the forecast dust concentrations from the integrated wind modeling system. Fourth, the results are presented and verified by comparing the predictions of the two dust storms with both conventional meteorological data and satellite data. Fifth the study and its findings are summarized, and research areas are identified that require future work.

2. Data and Climatology

In the period 1995–2005 dust was reported on a total of 55 days by Australian Bureau of Meteorology stations. There were 43 days on which

Table 1. Total number of days dust was reported each year in the period 1995 to February 2005.

	1995	1996	1997	1998	1999	2000	2001	2002	2003	2004	Feb 2005
Local	—	—	1	—	3	1	1	4	2	—	—
Long-range	1	1	—	—	—	1	1	26	11	1	1

dust transport was long-range and 12 days on which dust transport was local (Table 1).

Note that in the spring months of September–November 2002, dust was reported on a total of 30 days, comprising four local dust transport days and 26 long-range dust transport days. Without strong synoptic scale low-level winds, the decadal total of 12 local dust storms contained 8 days during which convective gusts were the likely cause. Of the remaining four, three were from localized wind storms near Whyalla and Adelaide in South Australia (SA) and one was from a dry, continental southeast wind surge in tropical Queensland (QLD). Hereafter, we focus only on the long-range dust storms, all 43 of which are associated in some way with the passage of a cold front. When these 43 cases were further classified synoptically, 24 were from cold fronts that were linked to zonal westerlies or low-pressure systems in the Great Australian Bight (GAB). The remaining 19 were post-frontal, being the result of high pressure systems in the GAB that became established after the passage of frontal systems. The first group typically is characterized by pre-frontal northwest winds and west to southwest winds over central eastern Australia in the immediate post-frontal air, while the second group is typically characterized by post-frontal south to southeast winds in the immediate post-frontal air. The low-level temperature inversion in the post-frontal air contributes to the concentration of dust particles near the surface and hence a reduction in visibility over a one to several days after the passage of the cold front. Such an inversion was present in 8 days out of the 43. These eight cases fall into the second or post-frontal southerly wind group just defined.

The main frontal characteristic within the long-range dust transport category is the length and longevity of the cold front's path. Some frontal systems moved east more quickly and cleared the east Australian coast, a distance of several thousand kilometres, while others moved slowly, typically either stalling or weakening over eastern Australia. The depth of the mixed layer on dust reporting days was estimated from the nearest radiosonde stations. Observations of vertical temperature and wind observations typically extended above 850 hPa and in some cases above 700 hPa. In the climatology, 900 hPa wind speeds at 0000 UTC (08:30 local time) at Woomera, the station nearest the source area, were all greater than 30 knots for long-range dust transport associated with fronts that cleared the east Australian coast and greater than 20 knots for dust transport associated with fronts that stalled or weakened over eastern Australia. However, there was no threshold value of the 900 hPa wind speed that discriminated between these frontal characteristics within the long-range category.

3. Brief Overview of Case Studies

3.1. *Case study 1: October 23, 2002*

The main antecedent conditions for dust storm generation are drought or rainfall deficiency over the dust source region, as for the Lake Eyre (SA) drainage basin for the 6 months ending September 2002, when rainfall deficiencies were the lowest on record. During such periods of rainfall deficiency, the surface soil is far more prone to wind erosion than usual.

3.2. *Case study 2: February 2, 2005*

In the 6 months to the end of January 2005 there were rainfall deficiencies below decile 3 (very much below average) in the Lake Eyre source region and this area of very much below average rainfall increased in the three months ending January 2005 over the source region. With a vigorous frontal system developing in the GAB, dust storm generation in northeast SA is likely to occur.

4. Integrated Wind Erosion Model

4.1. *The atmospheric model*

The atmospheric model used is the HIgh RESolution NWP model (HIRES), developed at The University of New South Wales and the University of Oklahoma.[7] Model features are in Table 2.

4.2. *The wind erosion scheme*

Details of the wind erosion scheme were described originally by Shao *et al.*,[3] and since then improvements have since been made to the land surface scheme, the GIS database, and the particle entrainment, transport and

Table 2. Details of the HIRES atmospheric model used for this study.

Model feature	HIRES
Horizontal resolution	15 km
Numerical scheme	Split semi-implicit (high order)
No. of vertical levels	34
Assimilation scheme	6-hourly cycling
Initialization	Dynamic
Orography	2 min resolution
Boundary layer scheme	Mellor–Yamada, Level 2.25
Radiation scheme	Fels–Schwarzkopf
Convective scheme	Kain–Fritsch
Sea–surface temperatures	5-day average
Lateral boundary conditions	From BMRC LAPS model

deposition. These changes are discussed by Irannejad and Shao,[9] Lu and Shao[4] and especially by Shao.[10] The wind erosion scheme is described in detail by Shao *et al.*[5] The scheme tracks the history of various particle sizes and the output we are interested in for this study is the total dust concentration, which is the sum of the concentrations of all the dust particle sizes considered in the scheme. As in the study by Shao *et al.*,[5] we used three dust particle sizes, and therefore calculated the temporal and spatial evolution of the three particle concentration terms c_1 c_2, and c_3 that contribute additively to the total dust concentration, one concentration term from each of the particle sizes. The particle sizes, d_i, were $d_1 < 2\,\mu\text{m}$; $2\,\mu\text{m} \leq d_2 \leq 11\,\mu\text{m}$; and $11\,\mu\text{m} \leq d_3 \leq 22\,\mu\text{m}$.

5. Results and Discussion

For the modeling case studies, satellite imagery indicating suspended dust provides the best available verification, for Australia, of the aerial extent of dust. Dust areas in these satellite images can be compared to the model predicted wind fields for the same time to provide verification of the model. Multi-spectral satellite techniques rely principally on differences in absorption and radiation between water/ice and dust in key infrared bands. The satellite images used for highlighting the dust areas were generated using GOES-9 imagery in the Bureau of Meteorology by the 11–12 μm "split-window" or "reverse absorption" algorithm that is used to identify volcanic ash.[11,12] This technique uses the different absorption characteristics of dust and water vapour clouds in the 11 and 12 μm wavelength bands. The difference in the two bands creates a "split-window" image from which areas of dust are identified. The main limitation of the technique is that it only works for (semi-) transparent clouds, relying on emitted thermal energy from the earth's surface passing through them. Verification of the model predicted dust concentrations is mainly by the use of the satellite image enhancements described above and quantitatively, from available synoptic observations of reduced visibility estimated by the Bureau of Meteorology and observers. The problem in verifying by visibility observations is the scarcity of reports in inland central and eastern Australia (see Fig. 1) and once dust becomes sufficiently elevated and dispersed well away from the dust source, reductions in visibility due to suspended dust might not be reported.

5.1. *Case study 1: October 23, 2002*

Figures 2(a), (b) are infrared images at 1800 UTC 22 October 2002 (04:00 local, 23 October) and 06:00 UTC 23 October (16:00 local). The model predicted dust concentrations at 00:00 UTC on 23 October are contoured from grid values and are defined in area and amount in Fig. 2(c). After 06:00 UTC the area and concentration rapidly diminished (not shown). In the infrared images the intensity of the dust concentration is indicated by the color.

Each color step represents a half-degree difference in T 11 μm–T 12 μm below a particular threshold. Each color step can be thought of as a change in the strength of absorption, which approximates the thickness of the dust cloud, and is also affected by particle size and amount of surface radiation. The dust concentrations are be expected to increase from the morning through the afternoon due to the increasing depth of the mixed layer and stronger winds at the surface lifting more dust. This increase is evident in the two images. Figure 2(d) shows synoptic observations that recorded dust including the lowest visibility for 23 October. High visibility values amongst low values mostly indicates stations with few reporting times per day such that a dust storm with very low visibility may have affected the station but not at or even close to any reporting time during the day. In Fig. 2(d) the observations that recorded the lowest visibility tend to be in southern and central QLD which compares well with the area of highest model predicted average dust concentration in Fig. 2(c).

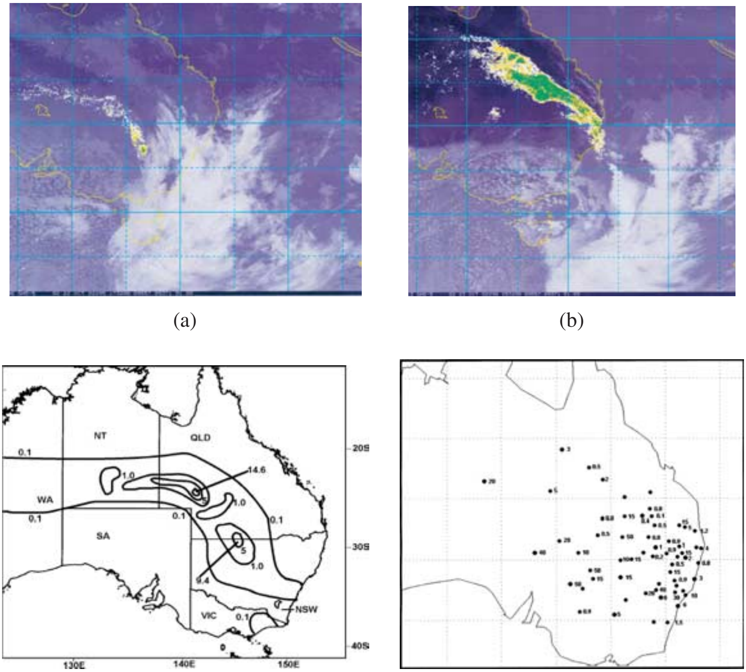

(a) (b)

(c) (d)

Fig. 2. (a) GOES-9 imagery at 18:00 UTC October 22, 2002 (04:00 local, 23 October). Increasing dust shown by white-yellow-green. (b) As in (a) except for 06:00 UTC 23 October (16:00 local). (c) HIRES model predicted dust concentration (g^{-3}) 00 UTC October 23, 2002. (d) Synoptic observations reporting dust including lowest visibility (km) on October 23, 2002.

5.2. *Case study 2: February 2, 2005*

Figures 3(a), (b) is infrared images highlighting dust concentrations at 04:00 UTC and 19:00 UTC February 2, 2005, respectively. The model-predicted dust concentrations for the same times are shown in Figs. 3(c), (d). At first the dust is concentrated near Lake Eyre, which is experiencing low level south to southeast winds, and over southwest QLD, which is closer to the front but is also experiencing post-frontal southerly winds.

An increase in the dust concentration is evident in the satellite image with red (high) appearing in Fig. 3(a). This is consistent with an increase in the model predicted dust concentration values. Figure 3(e) shows synoptic observations that recorded dust including the lowest visibility on February 2, 2005. The main point to note here is the low visibility values

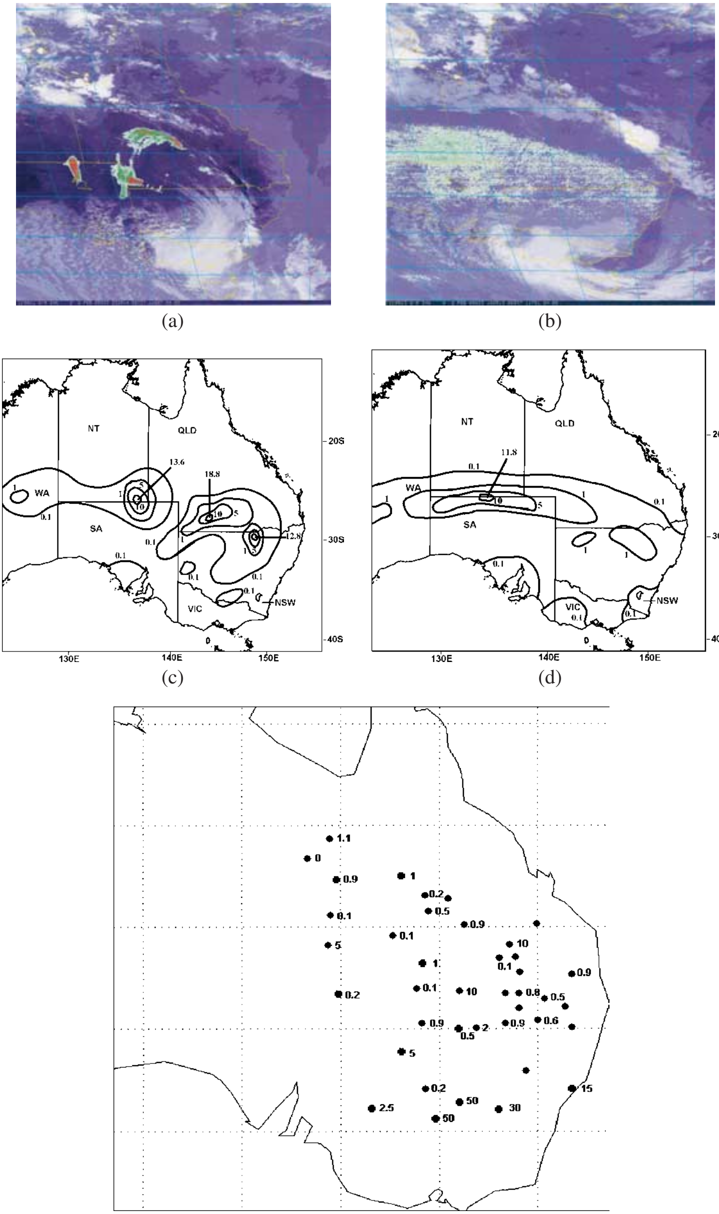

Fig. 3. (a) GOES-9 imagery of dust concentration for 04:00 UTC February 2, 2005. (b) As in (a), except for 19:00 UTC. (c)–(e) Synoptic observations reporting dust including lowest visibility (km) on February 2, 2005.

recorded at places across northern NSW. This area of concentrated dust does not appear in Figs. 3(a), (b) but does show as a weak concentration later in the period (Fig. 3(c)). The most probable cause of this inconsistency early in the period was the thick cloud near the front which is evident across northern NSW in Figs. 3(a), (b) but not in Figs. 3(c), (d).

5.3. *Synoptic differences between the two case studies*

For both cases the low-level frontal movement and associated wind speeds were sustained across eastern Australia from the source to the east coast. In this case study of February 2, 2005 there was cloud and rain over the southern portion of the front in Victoria. There was no rain and little cloud where the dust occurred in the first case study, which is more typical of the climatology.

6. Conclusions

From 1995 to 2005 there were 55 "dust days" in central eastern Australia, as recorded by the Australian Bureau of Meteorology's synoptic stations. These 55 days consisted of 43 associated with fronts, with 24 classified as either embedded in the zonal westerlies in the GAB or in westerlies generated by low-pressure systems in the GAB. The remaining 19 were associated with fronts over eastern Australia where high pressure systems in the GAB produced postfrontal south to southeast winds. The case studies both were in the latter group. The first synoptic group is characterized typically by single or two consecutive days on which dust was reported. The second day in a sequence was usually when a front crossed the east coast thereby causing a translation of dust reports to concentrate in coastal areas.

However, there was one sequence of six days in the second synoptic group when dust was reported over western QLD under the influence of persistent south to southeasterly winds in that area while the preceding frontal systems typically stagnated and/or weakened over central QLD. An overview was described of each of two case studies where recent dust storms were reported. The two case studies of October 23, 2002 and February 2, 2005 were similar insofar as frontal systems developing in the GAB intensified across the dust source region and the associated wind changes carried the dust across the east coast of Australia. The antecedent soil conditions in the dust source region together with the synoptic scale frontal movement and frontal strength were generically similar for both cases. The model-predicted dust concentrations in the two case studies were broadly consistent with the observations from synoptic stations reporting dust.

Finally, the controlling feature for the two cases, namely, a frontal system over southeast Australia with high pressure following in the GAB, falls into the second synoptic category as described in the climatology. In the climatology it is interesting to note that there were slightly more cases (24) of the first synoptic group with fronts in the westerlies or developing lows over the GAB compared to the second group containing the three cases studies with high pressure systems in the GAB and postfrontal south to southeasterlies (19). In contrast, previous climatological studies in the middle of the twentieth century describe the controlling synoptic scale influence producing dust as only high pressure systems in the Great Australian Bight generating south to southeast winds following frontal systems across eastern Australia. These climatological differences in those synoptic to large-scale circulation characteristics that are related to dust events are currently being investigated and will be reported on in the near future.

References

1. G. H. McTainsh and J. R. Pitblado, Dust storms and related phenomena measured from meteorological records in Australia, *Earth Surf. Processes Landforms* **12** (1987) 415–424.
2. M. Ekström, G. H. McTainsh and A. Chappell, Australian dust storms: Temporal trends and relationships with synoptic pressure distributions (1960–1999), *Int. J. Climatol.* **24** (2004) 1581–1599.
3. Y. Shao and L. M. Leslie, Wind erosion prediction over the Australian continent, *J. Geophys. Res.* **102**, D25 (1997) 30,091–30,105.
4. H. Lu and Y. Shao, Toward quantitative prediction of dust storms: An integrated wind erosion modelling system and its applications, *Environ. Modell. Software* **16** (2001) 233–249.
5. Y. Shao, L. M. Leslie and 7 others, Northeast Asian dust storms: Real-time numerical prediction and validation. *J. Geophys. Res.* **108**, D22 (2003) 4691 DOI:10.1029/2003JD003667.
6. Z. Guocai and S. Zhenxin, Operational duststorm prediction in China — an overview, *WMO Bull.* **53**, 4 (2004) 333–336.
7. L. M. Leslie and R. J. Purser, Three dimensional mass-conserving semi-Lagrangian scheme employing forward trajectories, *Mon. Wea. Rev.* **123** (1995) 2551–2556.
8. Y. Shao, E. Jung and L. M Leslie, Numerical prediction of northeast Asian dust storms using an integrated wind erosion modeling system, *J. Geophys. Res.* **107**, D24 (2002) 4814–4837.

9. P. Irannejad and Y. Shao, Description and validation of the atmosphere-land-surface interaction scheme (ALSIS) with HAPEX and Cabauw data, *Global Planet Change* **19** (1998) 87–114.
10. Y. Shao, A model for mineral dust emission, *J. Geophys. Res.* **106** (2001) 20,339–20,254.
11. A. J. Prata, Infrared radiative transfer calculations for volcanic ash clouds, *Geophys. Res. Lett.* **16** (1989) 1293–1296.
12. A. J. Prata, Observations of volcanic ash clouds in the 10–12 μm window using AVHRR/2 data, *Int. J. Rem. Sens.* **10** (1989) 751–761.

SEA ICE MOTION AND DEFORMATION IN THE MARGINAL ICE ZONE THROUGH SAR[*]

JUN YU[†], ANTONY K. LIU[‡] and YUNHE ZHAO[§]
[†]*Department of Mathematics and Statistics, University of Vermont*
16 Colchester Ave, Burlington, VT 05401, USA
[‡]*ONRIFO Asia, Unit 45002, PO Box 382*
APO AP 96337–500
[§]*Caelum Research Corporation, Rockville, MD 20850, USA*

The objective of this study is to explore motion and deformation of sea ice in the marginal ice zone (MIZ). Sea ice properties in MIZ are highly variable and complex due to the complexity of the ocean dynamic and thermodynamic processes, as well as atmosphere-sea and ice–ocean interactions. These processes and interactions play important roles in the distribution of heat, mass, and momentum fluxes in Polar Regions and in the control of the ice edge and its location. In an earlier study, sea ice features including thickness, type and motion have been analyzed using the high resolution synthetic aperture radar (SAR) imagery. A segmentation technique with dynamic local thresholding (DLT) was used to segment and to perform ice floe tracking. In this paper, we extend the earlier study to include motion and deformation analyses of the sea ice, as well as the possible effects of air–ocean–ice interactions associated with wind and waves. With the sea ice images well classified, it is efficient to track ice floes of different sizes and to study ice motions such as translation, rotation, convergence and divergence. Finally, inter-comparisons between remotely sensed products will be discussed.

1. Introduction

The ice cover in the marginal ice zone (MIZ), where sea ice and ocean meet, is about 100 km wide from the ice edge. Dynamic and thermodynamic processes in the MIZ are highly variable and complex due to a variety of organized nonstationary motions, such as jets, fronts, vortices, upwelling/downwelling.[1,2] The St. Lawrence Island polynya (SLIP) is a commonly occurring winter phenomenon in the Bering Sea, where openings in the ice cover are recurring.[3] These processes play important roles in the distribution of heat, mass, and momentum fluxes in Polar Regions and

---

[*] This work is supported by the Vermont-NASA EPSCoR Program and the University of Vermont.

in the control of the ice edge and its location. Numerical models for ice edge upwelling, in which the ice is allowed to be a dynamic medium (see Refs. 1, 4 and 5) show the effects from wave actions to be quite significant. In recent years, there has been a massive increase in high-quality ocean/ice data for research use. These data sources include SMMR, SAR, QuikSCAT, SSM/I, and ASMR-E. Therefore, it is necessary to develop automated algorithms to process the data for ocean and ice studies. Gloersen *et al.*[6] reported a frequency analysis of the Arctic sea ice concentration using the SMMR data. Recently, Wu and Liu[7] developed an automated algorithm for ocean feature detection, extraction and classification in SAR imagery, using two-dimensional wavelet analysis. Remote sensing data can also be processed to create ice motion products. Yu and Liu[8] carried out automated sea ice texture classifications and motion analysis using SAR imagery. Zhao and Liu[9] used wavelet analysis of QuikSCAT and SSM/I data to obtain daily sea ice drift information for the Polar Regions. Here, we extend the study of Yu and Liu[8] to include sea ice motion and deformation, as well as the possible relationship to wind and wave effects in the MIZ. In the next section, we describe our method and results for sea ice classification, motion and deformation analyzes. In Sec. 3, we give some conclusions and outlook.

2. Methods and Results

We use SAR imagery to study sea ice motion and deformation in the MIZ. We focus our study in the Bering Sea area. Figure 1 shows the raw SAR imagery data taken on December 14, 2001. The spatial resolution is 100 m × 100 m. The outline of the St. Lawrence Island is visible in the lower-right quarter of the image, showing the geographic location of the SAR imagery. To illustrate our method, we focus on the inset in Fig. 1, a small rectangular area southeast of the St. Lawrence Island. We then choose two consecutive SAR images of December 11 and 14, 2001 in order to study ice motion and deformation. These are shown in Figs. 2 and 3, with the eastern tip of the St. Lawrence Island visible in the upper right corner.

As was pointed out in Yu and Liu,[8] a segmentation technique with DLT can be used to analyze and segment unstructured sea ice data. Since a variety of motions and mesoscale activity exist in the MIZ, sea ice features in SAR imagery vary at different scales for different times and locations in the MIZ. Therefore, no direct global thresholding method can compensate for all these variations. DLT is a method of generating global thresholds through a dynamic local thresholding and we use this method in this study.

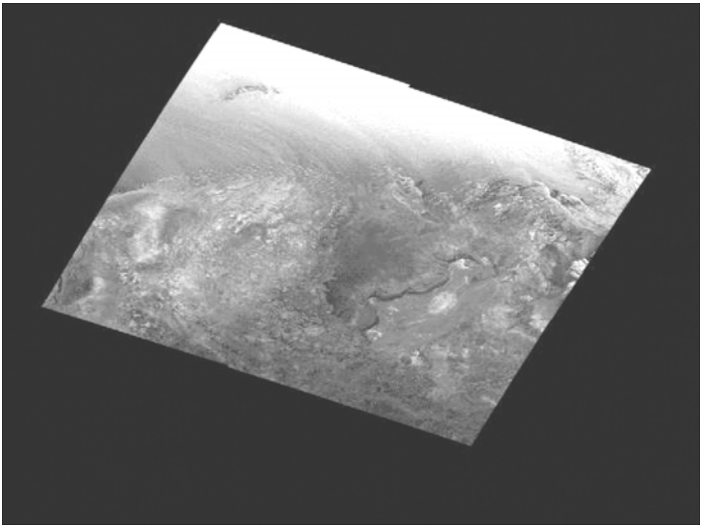

Fig. 1. SAR imagery data for the Bering Sea region taken on December 14, 2001.

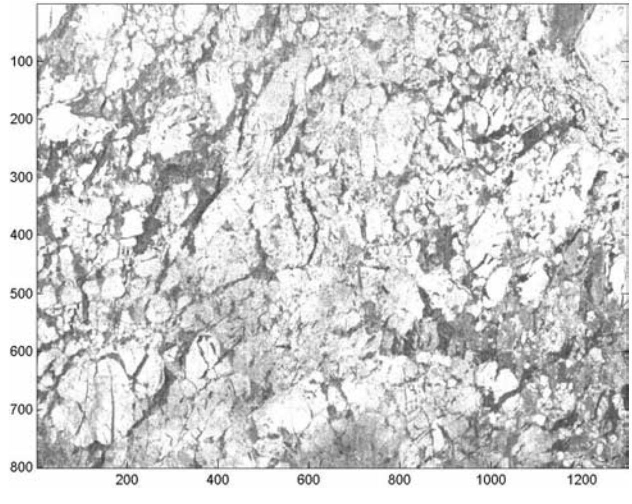

Fig. 2. SAR data for the cut-out area taken on December 11, 2001.

The initial classification is then supplemented using statistical attributes and heuristic geophysical knowledge organized in expert systems. In Figs. 4 and 5, we show the two-class segmentation results using the DLT method. Statistical method, based on the maximum correlation of nearby pixels

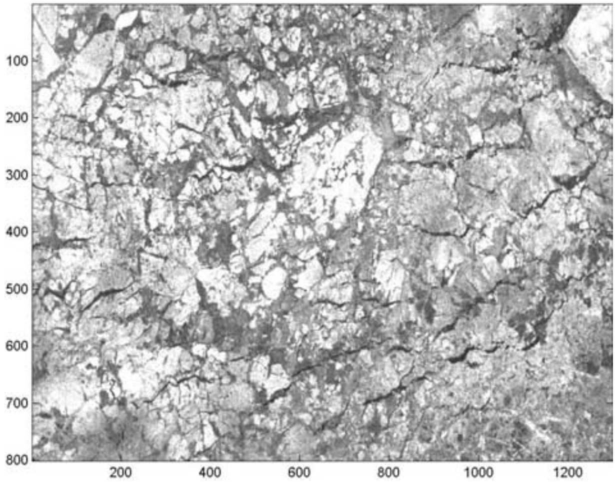

Fig. 3. SAR data for the cut-out area taken on December 14, 2001.

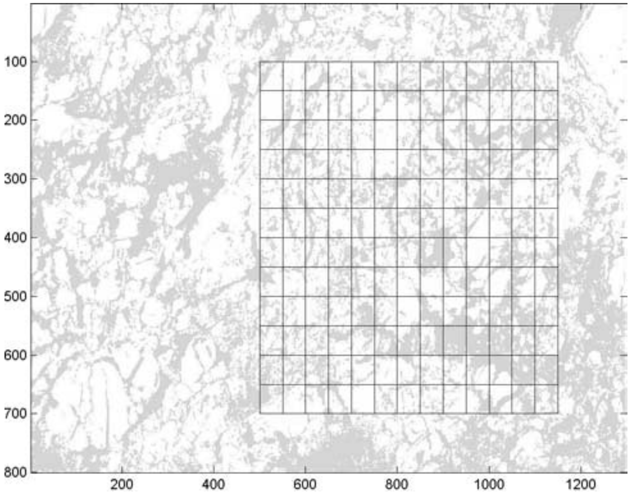

Fig. 4. Two-class segmentation result of Fig. 2, with a uniform grid (5 km × 5 km).

from the two-class segmentation results, is used to derive ice motion and deformation maps. Here, we track a uniform grid (5 km × 5 km) in Fig. 4 to observe interesting ice deformation behavior in Fig. 5. In Fig. 6, we show the ice velocities superimposed on the two-class segmentation result (Fig. 4 without the uniform grid). With the sea ice images well classified,

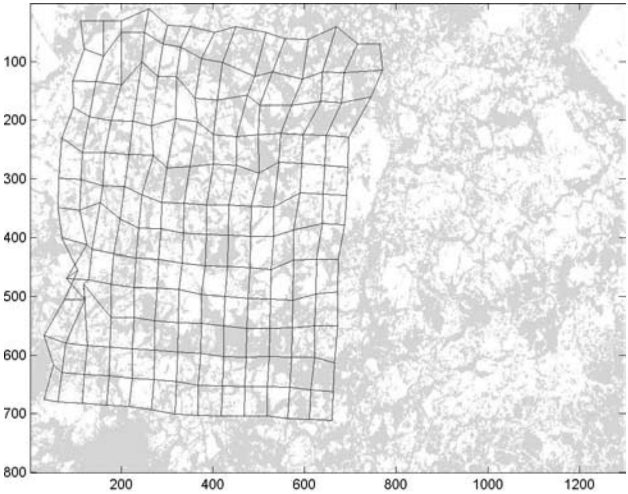

Fig. 5. Two-class segmentation result of Fig. 3, with deformed grid from Fig. 4.

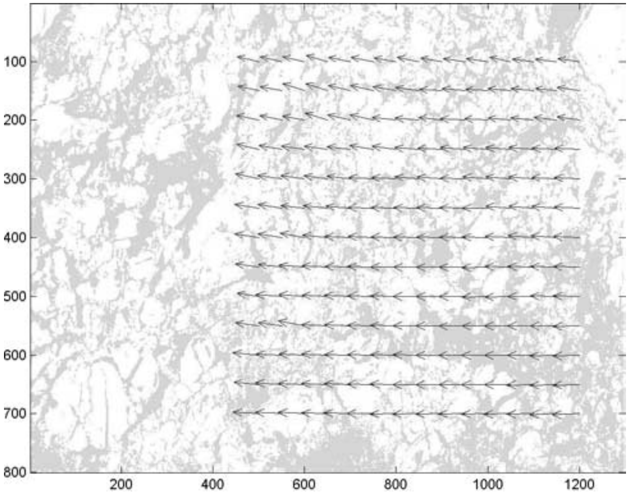

Fig. 6. Sea ice motion map on December 11, 2001, derived from Figs. 4 and 5 without grids.

it is efficient to track ice floes of different sizes and to study ice motion and deformation.

In Fig. 7, we show a sea ice motion map in Bering Sea on February 23, 2004 as derived from AMSR-E 89GHz data using wavelet transform

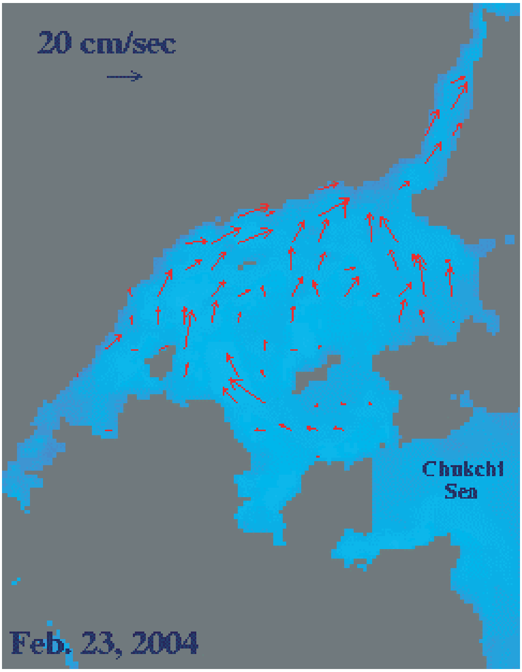

Fig. 7. Sea ice motion map in Bering Sea from AMSR-E 89 GHz data.

method. The spatial resolution is 75 km × 75 km, much larger than that for SAR data. However, the general motion of a translation and a rotation around the St. Lawrence Island can be observed.

3. Conclusions and Outlook

We have presented results of sea ice motion and deformation studies using automated sea ice classification and statistical methods from SAR imagery. We observe in Figs. 6 and 7 that an ice motion (of spatial scale larger than 10 km) consists of a translation and a rotation around the St. Lawrence Island. Wind forcing and ocean current might be the major courses of this motion. By tracking the change of a uniform grid in Fig. 4 to the deformed grid in Fig. 5, a clearer picture is revealed of the ice field deformation at a spatial scale of about 5 km. Wind, wave and ice floe collisions may have played important roles for these smaller scale variations. A more detailed comparison study of SAR and AMSR-E data has been planned. Furthermore, inter-comparison between remotely sensed products and model simulations can in general provide additional insight into the ice and ocean dynamics and their processes.

References

1. A. K. Liu, S. Hakkinen and C. Y. Peng, *J. Geophys. Res.* **98**, C6 (1993) 10,025.
2. A. K. Liu, C. Y. Peng and T. J. Weingartner, *J. Geophys. Res.* **99**, C11 (1994) 10,025.
3. A. H. Lynch, M. F. Glueck, W. L. Chapman, D. A. Bailey and J. E. Walsh, *Tellus* **49A**, 2 (1997) 277.
4. M. Ikeda, *J. Geophys. Res.* **90** (1985) 9119.
5. S. Hakkinen, *J. Geophys. Res.* **91** (1986) 819.
6. P. Gloersen, J. Yu and E. Mollo-Christensen, *J. Geophys. Res.* **101**, C3 (1996) 6641.
7. S. Y. Wu and A. K. Liu, *Int. J. Remote Sens.* **24**, 5 (2003) 935.
8. J. Yu and A. K. Liu, *Advances in Engineering Mechanics–Reflections and Outlooks, In Honor of Theodore Y.-T. Wu*, (eds. A. T. Chwang *et al.*), World Scientific Publishing Company (2005) 681.
9. Y. Zhao and A. K. Liu, *IEEE Trans. Geosci. Rem. Sens.* **40** (2002) 1241.

INTERANNUAL VARIATIONS IN PACIFIC SST DEVIATIONS THROUGH AVHRR*

JUN YU† and PER GLOERSEN‡
†*Department of Mathematics and Statistics, University of Vermont*
Burlington, VT 05401, USA
‡*NASA/Goddard Space Flight Center*
Greenbelt, MD 20771, USA

We study variability of Pacific sea surface temperature (SST) from 1985 to 1997 utilizing the data derived from the Advanced Very High-Resolution Radiometer (AVHRR). In order to enhance our analysis on the SST, we preprocess our data to derive Pacific SST deviations. Then, we study Hoffmueller diagrams for the SST deviations along different paths in the Pacific. Both 1987 and 1997–1998 El Niño events as well as the 1984–1985, 1989 and 1996 La Niña events are clearly depicted. Hoffmueller diagram along a path in the North Pacific shows an eastward moving trough during 1986 to 1989 and the pattern is followed by moving crests up to about 1993. Finally, we compare our current results with those from earlier studies using the NASA data of scanning multichannel microwave radiometer (SMMR).

1. Introduction

Climate variability in oceans has received considerable attention in recent years (see for example, Refs. 1–4). Global SST/Sea Level Pressure waves as well as basin-scale upper ocean temperature anomalies were studied in Refs. 5–7. Troposphere thermal and vorticity budgets were studied in Ref. 8, showing El Niño Southern Oscillations (ENSO) as one of the two dominant signals in Pacific Decadal Oscillation in the mid-latitude North Pacific Ocean from 1979 through 2001. Here, satellite measurements of SST are based on techniques in which spaceborne infra-red and microwave radiometers detect thermally emitted radiation from the ocean surface (see Ref. 9). Procedure for SST retrievals from infrared sensors was developed in Ref. 10 for the NOAA polar-orbiting AVHRR. Application of SST in computing the latent heat flux can be found in Ref. 11. Reference 12 described the calibration and processing procedure for obtaining SST data from the SMMR on

---

*This work is supported by the Vermont-NASA EPSCoR Program and the University of Vermont.

board the NASA Nimbus-7 satellite during 1978–1987. Events associated with ENSO during this time period were studied in Ref. 13 for global SST and in Ref. 14 for SST in the southern Pacific and Indian Oceans.

In our current study, we are interested in analyzing interannual and decadal variability in the Pacific SSTs from 1985 to 1997 using the AVHRR satellite data. Here, we focus on both spatial and temporal distribution of the ENSO component in the Pacific as well as the propagation pattern. The main objective here is to examine the dynamic behavior of SST and its implications for climate modeling and climate variability. In Sec. 2, we introduce our method and derive the Pacific SST deviations. Results and discussions are given in Sec. 3. Finally, we make concluding remarks in Sec. 4.

2. Method

There is a rich spectrum of variability in the SSTs, ranging from intraseasonal, seasonal, interannual to decadal. In order to enhance the observations of the interannual to decadal events that are the subject of this paper, we preprocess our data to derive the Pacific SST deviations by removing a modeled seasonal cycle (see Ref. 13) from the data at each pixel. We then apply a spatial Gaussian filter to smooth out spatial fluctuations (of about $5^\circ \times 5^\circ$), which are probably caused by high-frequency temporal variations. Our Gaussian smoother matrix is 25×25, whose values are given by the two-dimensional Gaussian function centered in the box with half width of six grid elements. Notice that the AVHRR SST data has a half-degree resolution.

In order to study propagation patterns of the SST deviations, we select six paths in the Pacific Ocean (see Fig. 1). Five paths are latitude lines, along the equator, latitudes 35°, 45° and 50° north and latidude 40° south, respectively. The last path is chosen in the North Pacific and follows approximately the North Pacific Current.

Hoffmueller diagrams along the chosen path show the SST deviations versus the location along the path as the x-coordinates and the time as the y-coordinates. A propagation pattern can be identified as a diagonal color feature in the Hoffmueller diagram.

3. Results and Discussions

We now analyze Hoffmueller diagrams for the SST deviations along the six paths defined in Fig. 1 and compare our results with previous studies. The left panel of Fig. 2 shows the Hoffmueller diagram for the SST deviations

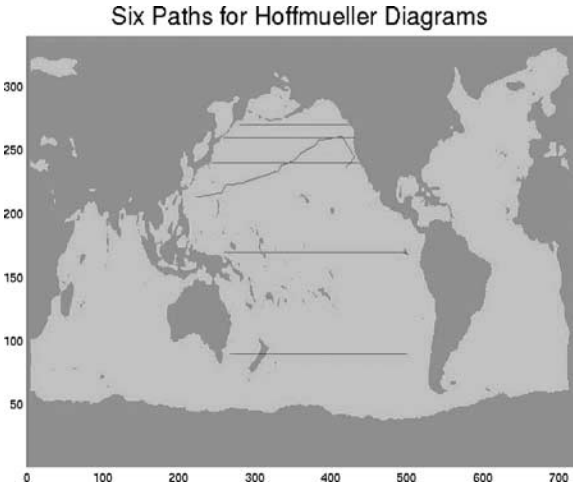

Fig. 1. Six paths along which Hoffmueller diagrams were analyzed.

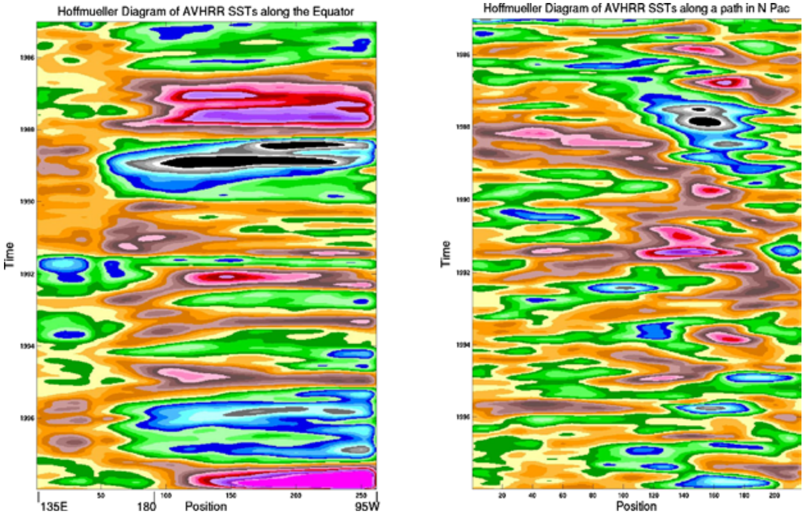

Fig. 2. Hoffmueller diagram of the AVHRR SST deviations for the path along the equator and the path in the North Pacific, as defined in Fig. 1.

along the equator. The colors in Fig. 2 represent temperatures deviated from the modeled seasonal SSTs. The values of the deviation range from −1.5°C for black color, −1.0°C for gray, −0.5°C for blue and green, 0.0°C for yellow, 0.5°C for brown, 1.0°C for pink and red, to 1.5°C for purple. Both 1987 and 1997–1998 El Niño events as well as the 1984–1985, 1989 and

1996 La Niña events are clearly depicted as either stationary or as rapidly eastward propagating waves.

Hoffmueller diagrams along the latitudes 35°, 45°, and 50° north are analyzed but are not shown here for brevity. We summarize our findings. There are eastward moving trough from about 1986 to 1989 and moving crests to about 1993 in these three diagrams. The pattern seems to move slower at higher latitude. These moving patterns are shown more clearly in the Hoffmueller diagram along the path in the North Pacific and we include this diagram in the right panel of Fig. 2. The results we obtained here with the AVHRR SST are in good agreement with those of SMMR SST reported in Ref. 13. In particular, the results from the two datasets agree well in the overlap time period of about 1985–1987. Finally, Hoffmueller diagram along the latitude of 40° south is also analyzed but not shown here. We observe near coincidence of decreased SSTs along the 40° latitude south with the 1984–1985 La Niña event in the equatorial Pacific. This is in agreement with the ENSO teleconnection in the South Pacific Ocean reported earlier using SMMR SSTs (see Ref. 14).

4. Conclusion

We have derived Pacific SST deviations using AVHRR data from 1985 to 1997. Hoffmueller diagrams for the SST deviations along six different paths in the Pacific have been analyzed. Our model clearly captured both 1987 and 1997–1998 El Niño events as well as the 1984–1985, 1989 and 1996 La Niña events. An eastward propagating wave of a period of about 4–6 years is shown in the right panel of Fig. 2, following approximately the North Pacific Current. This demonstrates the capability of AVHRR to show actual oceanic currents and gyres via the SST retrievals. Our results also show ENSO teleconnection for the 1984–1985 La Niña event in the South Pacific Ocean as reported in Ref. 14. Finally, inter-comparisons between studies using different imaging processing products are planned and can, in general, produce a more comprehensive picture of the ocean dynamic processes.

References

1. J. M. Wallace and Q.-R. Jiang, *Atmospheric and Oceanic Variability*, ed. H. Cattle, *Roy. Meteor. Soc.*, **17** (1987).
2. N. E. Graham, *Climate Dyn.* **6** (1994) 135.

3. R. J. Allan, in *El Niño and Southern Oscillation: Multiscale Variability, Global and Regional Impacts*, eds. H. F. Diaz and V. Markgraf (Cambridge University Press, Cambridge, 2000), p. 3.
4. W. B. White and Y. Tourre, *Geophys. Res. Lett.* **30**(12) (2003) 1651.
5. W. B. White, *Prog. Oceanogr.* **36** (1995) 169.
6. W. B. White and D. R. Cayan, *J. Geophys. Res.* **103** (1998) 21,335.
7. W. B. White, *J. Phys. Oceanogr.* **30** (2000) 1245.
8. W. B. White, G. Auad and I. Simmonds, submitted to *J. Climate* (2005).
9. E. G. Njoku, in *Surface Waves and Fluxes,* Vol. II, eds. G. L. Geernaert and W. J. Plant (Kluwer Academic Publishers, Dordrecht, 1990), p. 311.
10. E. P. McClain, W. G. Pichel and C. C. Walton, *J. Geophys. Res.* **90** (1985) 11587.
11. W. T. Liu, in *Surface Waves and Fluxes,* Vol. II, eds. G. L. Geernaert and W. J. Plant (Kluwer Academic Publishers, Dordrecht, 1990), p. 293.
12. P. Gloersen, *J. Climate and Appl. Met.* **23** (1984) 336.
13. J. Yu and P. Gloersen, *Int. J. of Rem. Sens.* **26** (24) (2005) 5419.
14. P. Gloersen, C. Chan, M. Zelinka and N. Huang, *Remote Sensing of the Environment*, submitted.

DIRECT RADIATIVE FORCING DUE TO ANTHROPOGENIC AEROSOL AND ASIAN DUST IN MARCH 2002 OVER EAST ASIA

SOON-UNG PARK* and EUN-HEE LEE
School of Earth and Environmental Sciences
Seoul National University, Seoul, 151-742, Korea
**supark@snu.ac.kr*

The Asian Dust Aerosol Model (ADAM) and the aerosol dynamic model with the output of the fifth generation of mesoscale model (MM5) in a grid of 30 × 30 km^2 have been employed to simulate the temporal and spatial distribution of the Asian dust aerosol and the anthropogenic aerosol concentrations in East Asia for the period of March 19–23, 2002 when a severe Asian dust event (Hwangsa) was observed in Korea. The simulated aerosols are used to estimate radiative forcing at the surface and the top of the atmosphere (TOA) with the use of the National Center for Atmospheric Research (NCAR) column radiation model (CRM) from the community climate model 3 (CCM3). The results indicate that the estimated mean total aerosol mass in the analysis domain for the period of March 19–20, 2002 is found to be about 880 mg/m^2, of which 98 and 2% are, contribute to the Asian dust aerosol and anthropogenic aerosol, respectively. However, the direct radiative forcing contribution from the anthropogenic aerosols is found to be about 40% of the mean radiative forcing at the surface ($-11\,\mathrm{W/m^2}$) and 45% at TOA ($-6\,\mathrm{W/m^2}$), implying the importance of the anthropogenic aerosol component on the direct radiative forcing at both the surface and TOA.

1. Introduction

Wind-blown mineral dust from deserts and semi-arid regions are important sources of tropospheric aerosols[1] and play an important role in the earth-atmosphere radiative system. It is estimated to contribute 1000 to 3000 Tg/year[1] to global atmospheric emissions of aerosols.[2–4]

Dust storms have become a distinct feature in many regions around the globe, including East Asia, West Africa, and South America.[5,6] In East Asia, Asian dust (Hwangsa in Korean) which is a typical example of mineral aerosol frequently occurs in the Sand desert, Gobi desert and Loess plateau in northern China and Mongolia during the spring season.[7–9] Some of the Asian dust is reported to reach western parts of the USA across the Pacific Ocean.[10,11] Husar *et al.*[10] indicate that the dust clouds in East Asia increase the albedo over the cloudless ocean and land by up to 10–20% and reduce the direct solar radiation by 30–40% causing a whitish discoloration of the blue sky, suggesting the importance of the Asian dust on the atmospheric radiation balance.

The purpose of this study is to estimate direct radiative forcing of Asian dust and anthropogenic aerosols in association with an intense Asian dust event observed in Korea during March 19–23, 2002 using the National Center for Atmospheric Research (NCAR) column radiation model (CRM) with the simulated spectral-mass concentration distribution by the Asian Dust Aerosol Model (ADAM) and the aerosol dynamic model.[12]

2. Model Description

The meteorological model used in this study is the nonhydrostatic version of the fifth-generation mesoscale model of (MM5, Pennsylvania State University/NCAR) defined in the x, y, and σ coordinate system.[13,14]

The domain of the model is shown in Fig. 1. The domain includes major dust source regions, namely, the Sand, Loess, Gobi and Mixed soil regions.[7,9] The model has a horizontal resolution of 30 km with 25 vertical layers.

The ADAM[7,9] and the aerosol dynamic model[12] with the gas-phase chemistry of the California Institute of Technology (CIT) model and the aqueous-phase chemistry of the Regional Acid Deposition Model (RADM) have been used to calculate the temporal and spatial distributions of the dust concentration and anthropogenic aerosols in the model domain.

The CRM model of NCAR[15,16] is used to estimate aerosol direct radiative forcing at the top of atmosphere (TOA) and the surface. This model uses a δ-Eddington approximation with 18 spectral intervals (7 for O_3, 1 for the visible, 7 for H_2O and 3 for CO_2) spanning the solar spectrum from 0.12 to 5.0 μm.

Average mineral components of soils obtained from 37 soil samples in the Asian dust source regions of the Sand, Gobi, Loess and Mixed Soil in northern China[17] that consist of quartz (49%), plagioclase (22%), k-feldspar (17%), illite (5%), kaolinite (2%), calcite (2%), gypsum (1%), amphibole (1%) and 14Ac (1%) are used with the refractive indices of these mineral components.[12]

The emission data of SO_2, NO_X, NH_3, CO, nonmethane volatile organic carbon (NMVOC), BC, and OC in the model domain are obtained from

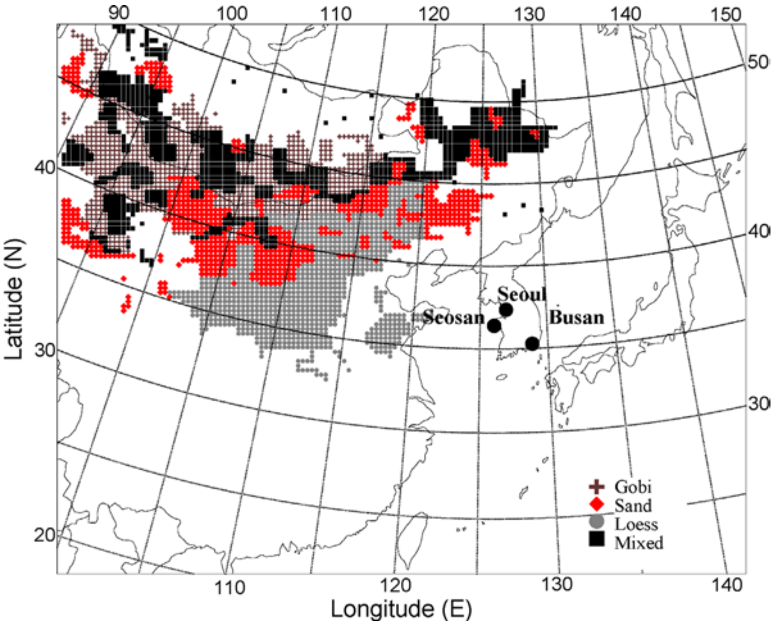

Fig. 1. The model domain and Asian dust source regions (++, Gobi, ◆◆, Sand, ●●, Loess, and ■■, Mixed). Several aerosol monitoring sites in Korea are shown.

Streets *et al.*[18] on a $30 \times 30\,\text{km}^2$ grid. The base year of the emission inventory is 2000.

3. Results

3.1. *Temporal variations of dust concentration*

Figure 2 shows the time series of modeled PM_{10} concentrations of Asian dust averaged for the layers below 100 m, 100–1500 m and above 1500 m, as estimated by the ADAM model. The mean-surface anthropogenic aerosol concentration is estimated by the aerosol dynamic model[12] with observations of PM_{10} concentration at several sites in South Korea (Fig. 1). The present ADAM model simulates quite well the temporal variation of the PM_{10} concentration of more than $1000\,\mu g/m^3$ during the Asian dust period at all sites. The starting and ending time of Asian dust and the timing of the maximum PM_{10} concentration simulated with ADAM are in good agreement with the observations at all sites over South Korea (Fig. 2).

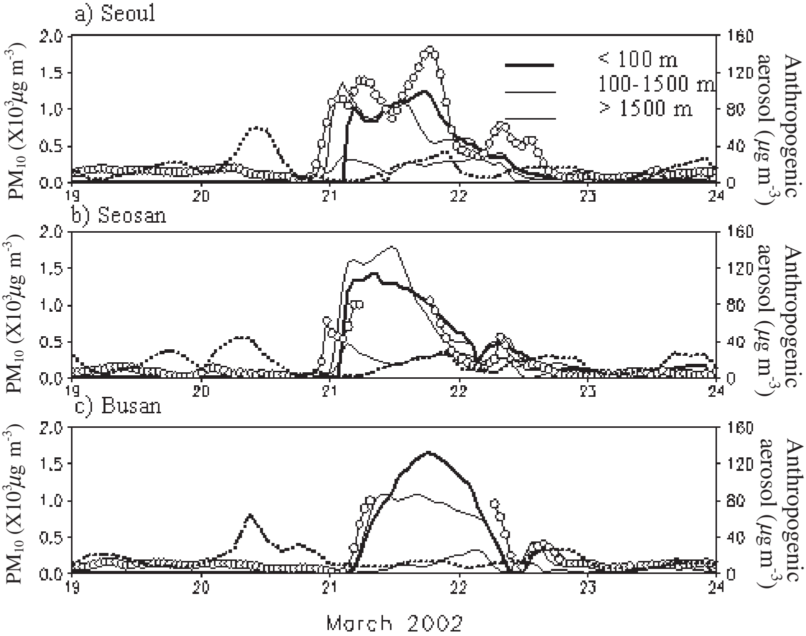

Fig. 2. The time series of modeled PM_{10} concentration of Asian dust ($\times 10^3\,\mu g/m^3$) averaged for the layers below 100 m (▬), 100–1500 m (—), above 1500 m (—) above the ground and the observed PM_{10} concentration (o-o-o-) at (a) Seoul, (b) Seosan, and (c) Busan in South Korea. The modeled anthropogenic PM_{10} concentration ($\mu g/m^3$) near the surface (· · · ·) is given in a different scale.

The contribution of the anthropogenic aerosols (black carbon, BC; organic carbon, OC; inorganic aerosol, IOC; and mixed aerosols of IOC, BC and OC) to the total PM_{10} concentration, is very small during the Asian dust period. However, these mainly contribute to the observed PM_{10} concentration during the nondust period (Fig. 2).

3.2. *Spatial distributions of aerosol concentrations*

Figures 3 and 4 show the spatial distribution of the daily averaged column integrated Asian dust concentration and anthropogenic aerosol concentration, respectively. The first dust storm which occurred on March 18 at the border of Mongolia and western Inner Mongolia and Gansu Province has progressively moved eastward accompanying newly developing dust storms over the Loess plateau and the northeastern part of Inner Mongolia.

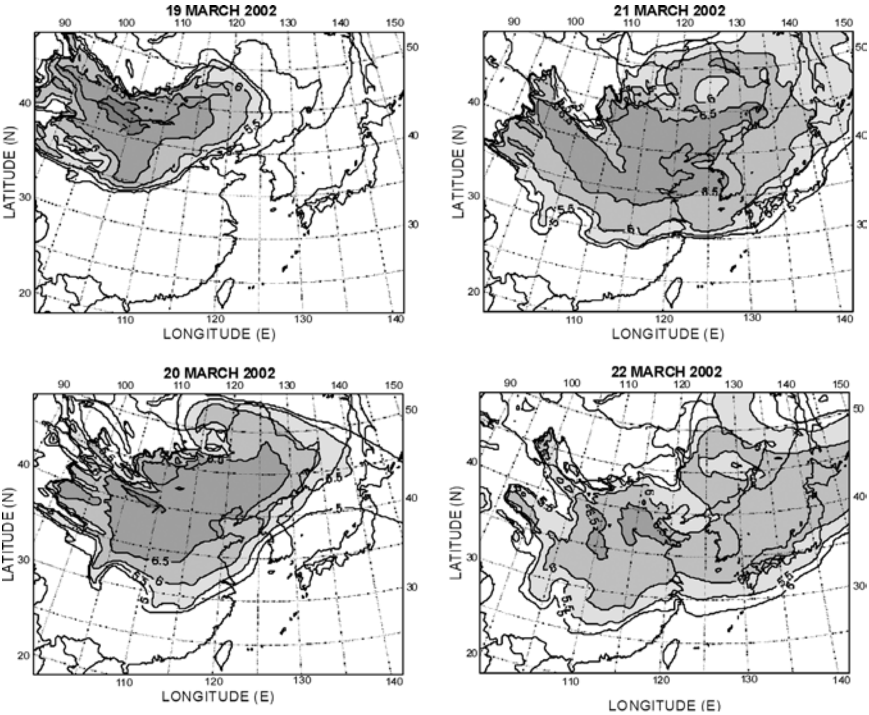

Fig. 3. Evolutionary features of the spatial distribution of the daily averaged vertically integrated Asian dust concentration (μg/m^2) expressed in common logarithms from 19 to 22 March, 2002.

The associated heavy dust clouds with vertically integrated dust concentration of more than $3\,\mathrm{g/m^2}$ have passed over the Korean peninsula on March 21, 2002 (Fig. 3) thereby producing the near surface $\mathrm{PM_{10}}$ concentration of more than $1500\,\mu\mathrm{g/m^3}$ at most of monitoring sites over South Korea (Fig. 2). In the meantime the vertically integrated anthropogenic aerosol concentration has its maximum value of more than $0.05\,\mathrm{g/m^2}$ over the southeastern part of China (Fig. 4) where the emission of pollutants is maximum. On March 21 when the Asian dust concentration is maximum over South Korea the anthropogenic aerosol concentration becomes minimum due to the southward transport of transformed aerosols by the prevailing northwesterly winds (Fig. 4). It is worth noting that the Asian dust source regions (Fig. 1) do not coincide with the anthropogenic pollutant emission regions, resulting in the different spatial distributions of these aerosols as seen in Figs. 3 and 4.

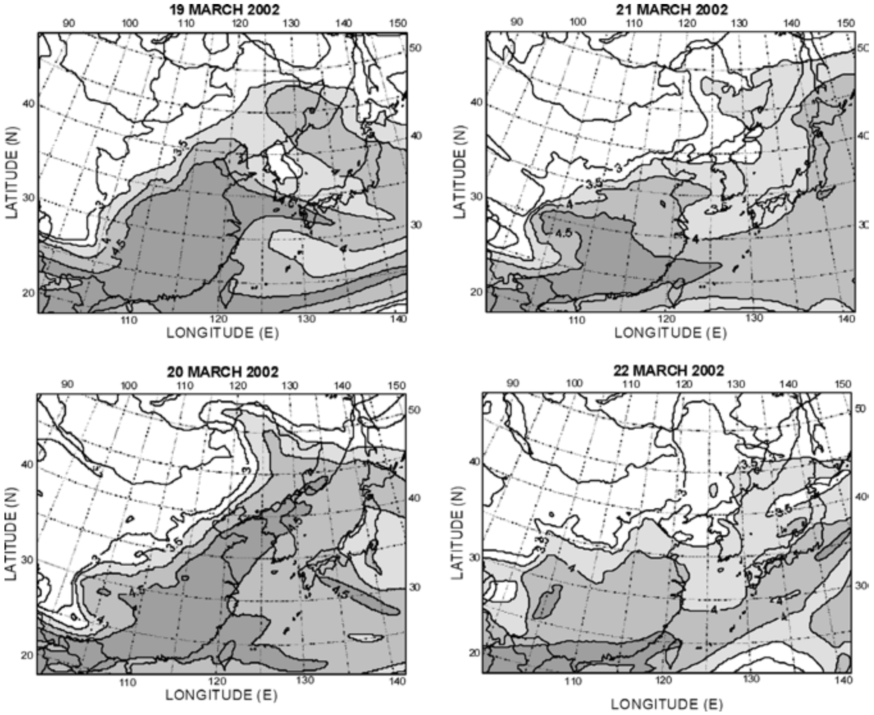

19 MARCH 2002

21 MARCH 2002

20 MARCH 2002

22 MARCH 2002

Fig. 4. As in Fig. 3, except for the anthropogenic aerosol.

3.3. *Estimation of aerosol direct radiative forcing*

Vertical profiles of temperature, pressure and H_2O mixing ratio obtained from the MM5 simulation and those of ozone and CO_2 mixing ratios from the CRM model are used as the initial profiles for CRM. The aerosol direct radiative forcing is obtained as the difference in shortwave net radiative fluxes at TOA and the surface between CRM simulations with and without aerosol mass loadings simulated by the aerosol dynamic model and ADAM.

The spatial distribution of the daily mean radiative forcing at the surface due to total aerosols (Asian dust aerosol + anthropogenic aerosol) indicates that there are two maxima with values greater than $-20\,\mathrm{W/m^2}$ in the northern central part of China and the southeastern part of China on March 19, 2002 (Fig. 5). The former is attributed to the Asian dust aerosol whereas the latter is due to the anthropogenic aerosol. As time progresses the dust clouds originating from southern Mongolia and Inner Mongolia are

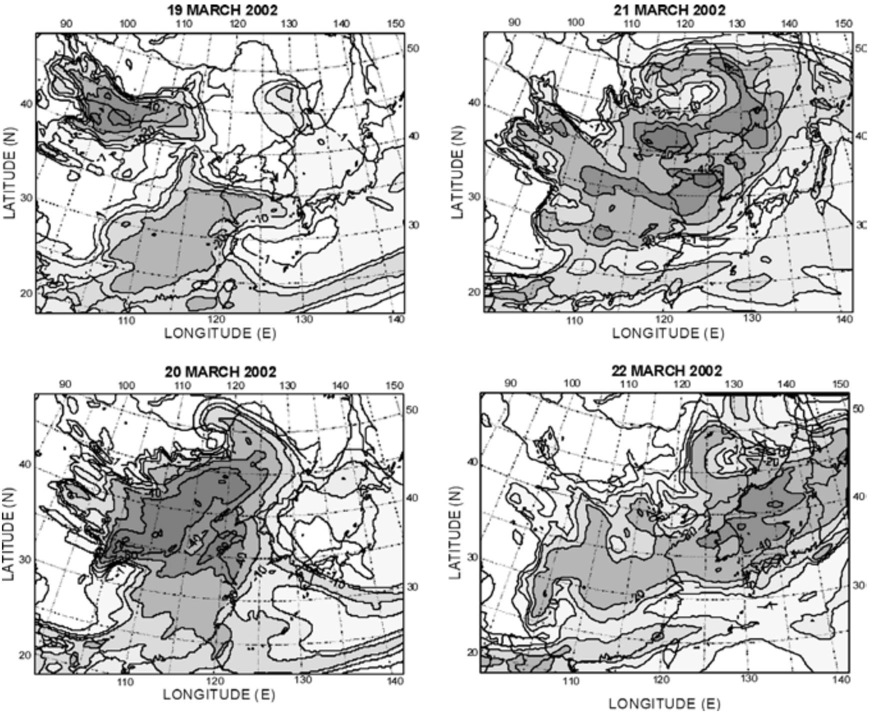

Fig. 5. Evolutionary features of the spatial distribution of direct radiative forcing (W/m^2) at the surface due to both Asian dust and anthropogenic aerosols.

transported down wind and merge together with the anthropogenic aerosol originating from eastern China where anthropogenic emissions of pollutants are maximum. This results in a high concentration of aerosols over the East China Sea, Korea, and Japan. Consequently, the direct radiative forcing at the surface is greater than –20 W/m^2 in these regions on March 22, 2002 (Fig. 5). Similar evolutionary features of observed aerosol index produced by the Total Ozone Mapping Spectrometer (TOMS) are evident during the analysis period (not shown here).

Furthermore, similar evolutionary features of the direct radiative forcing at TOA are evident in Fig. 6. In the early stage of the dust storm development in northern central China on March 19 the maximum radiative forcing at TOA associated with the dust storm is separated from that associated with transformed aerosols from anthropogenic pollutants that have their maximum emissions in East China. Gradually, both the Asian dust aerosol and the anthropogenic aerosol are transported eastward to merge together

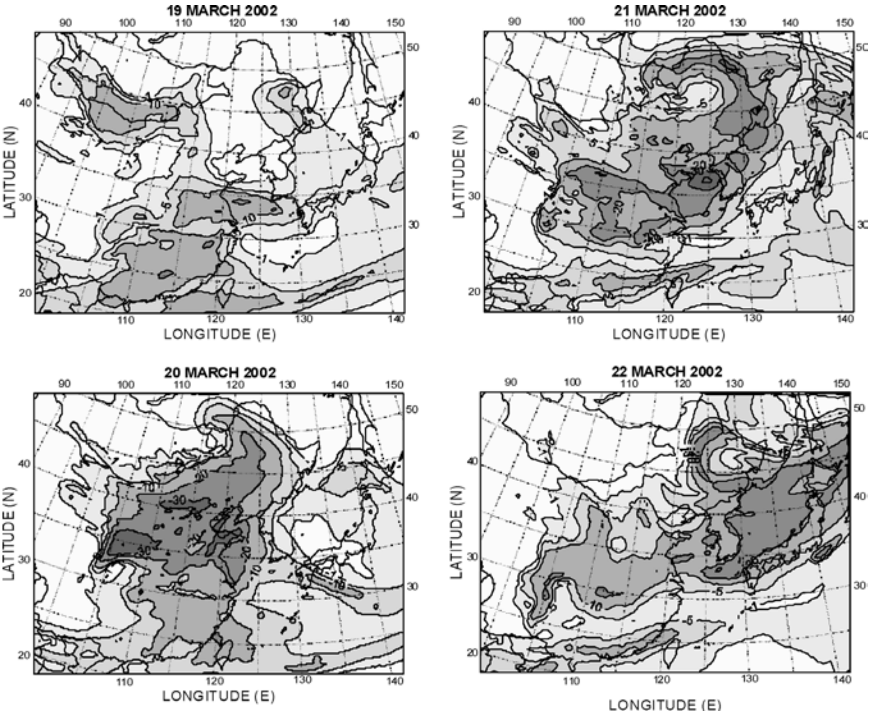

Fig. 6. The same as in Fig. 5 except for the radiative forcing at the top of atmosphere.

over Korea, Japan, and the northwestern Pacific Ocean, thereby producing high radiative forcing at TOA of more than –20 W/m^2 in these regions (Fig. 6). This implies that there is a significant impact of aerosols on the direct radiative forcing both at the surface and the top of atmosphere in the downstream source regions (Figs. 5 and 6).

The fractional contributions of each type of aerosol to the time-area averaged column integrated total mass, radiative forcings at the surface and at TOA averaged in the whole analysis domain in Fig. 1 are given in Fig. 7 for the period from 19 to 22 March, 2002. Averaged total aerosol mass in East Asia is about 880 mg/m^2, of which 98 and 2% are attributed to the Asian dust aerosols and anthropogenic aerosols, respectively (Fig. 7(a)). Averaged total anthropogenic aerosol mass is about 14 mg/m^2, of which 42, 27, 25, and 6% are attributed to the mixed aerosol (IOC-OC-BC), inorganic aerosol (IOC), organic carbon (OC) and black carbon (BC), respectively (Fig. 7(b)). The mean radiative forcing at the surface (SRF) is about -11 W/m^2, of which 61, 24, and 7% are attributed to the Asian dust aerosol,

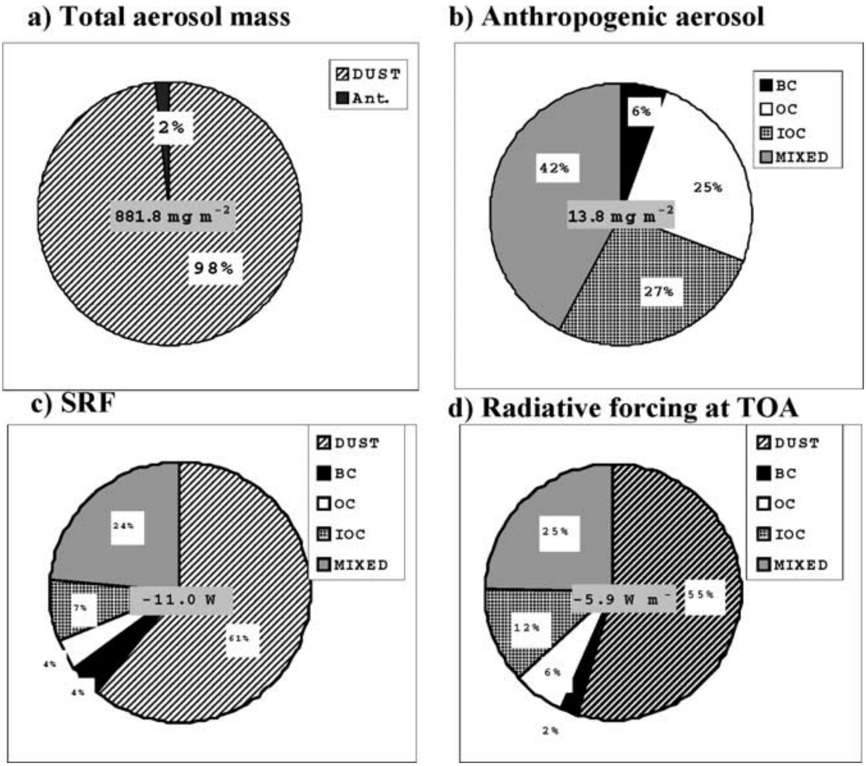

Fig. 7. The fractional contributions of each type of aerosol to the time-area averaged column integrated (a) total aerosol mass, (b) anthropogenic aerosol mass, direct radiative forcing (c) at the surface and (d) at the top of atmosphere averaged in the whole analysis domain in Fig. 1 for the period from 19 to 22 March, 2002.

the mixed aerosol and IOC, respectively (Fig. 7(c)), implying that the anthropogenic aerosol has a larger effect on the radiative forcing at the surface due to its small size distribution compared with that of the Asian dust aerosol.

The mean aerosol radiative forcing at TOA is about –6 W/m^2, of which 55% is due to the Asian dust aerosol and 45% to the anthropogenic aerosol (Fig. 7(d)), also implying a larger effect of the anthropogenic aerosol on the radiative forcing at TOA than the Asian dust aerosol. The difference between radiative forcing at TOA and at the surface yields an estimate of the aerosol absorption in the atmosphere. The estimated radiative forcing due to atmospheric aerosol absorption in East Asia is about 5 W/m^2. This implies that aerosols heat the atmosphere significantly over East Asia during the dust storm period. The atmospheric heating due to the Asian dust aerosol ($3\,\mathrm{W/m^2}$) is larger that due to the anthropogenic aerosol ($2\,\mathrm{W/m^2}$) for this period.

4. Summary and Conclusions

An intense Hwangsa event has been observed in Korea on March 19–23, 2002. The ADAM model and the aerosol dynamic model using the output of the MM5 meteorological model on a horizontal grid of $30 \times 30\,\mathrm{km^2}$ have been employed to simulate the temporal and spatial distribution of the Asian Dust aerosol and the anthropogenic aerosol concentration in East Asia during this period. The simulated both aerosols are implemented to estimate direct radiative forcing at the surface (SRF) and the TOA using the CRM model of NCAR.

The results indicate that the daily mean radiative forcing at the surface and at the top of atmosphere varies according to the evolutionary features of the dust aerosol and the anthropogenic aerosol concentrations in association with the development of dust storms and the emission distribution of the anthropogenic pollutants in East Asia. The averaged total aerosol mass in the analysis domain for the analysis period is found to be about $880\,\mathrm{mg/m^2}$. Most of the aerosol mass is composed of the Asian dust aerosol (98%). However, the estimated mean radiative forcing values at the surface ($-11\,\mathrm{W/m^2}$) and at the top of atmosphere ($-6\,\mathrm{W/m^2}$) by the dust aerosol are about 60 and 55%, respectively, suggesting a larger influence by the anthropogenic aerosol on the radiative forcing at both the surface and the top of atmosphere, which is due to its small-size spectrum.

The difference between the radiative forcing at TOA and at the surface indicates the atmospheric absorption due to aerosols. The estimated radiative forcing due to atmospheric aerosol absorption in the analysis domain is found to be $5\,\mathrm{W/m^2}$, of which 3 and $2\,\mathrm{W/m^2}$ can be attributed to the Asian dust aerosol and the anthropogenic aerosol, respectively. This study clearly indicates that both Asian dust and anthropogenic aerosols cause significant at the surface and at the top of atmosphere, particularly in downstream of sources where the dust aerosol and anthropogenic aerosol regions overlap each other.

Acknowledgments

This research is partially supported by Climate Environment System Research Center that is funded by Korea Science and Engineering

Foundation, the Ministry of Education under the Brain Korea 21 Program and the Meteorological and Earthquake R&D Program funded by Korea Meteorological Administration.

References

1. R. A. Duce, In *Dahlem Workshop on Aerosol Forcing of Climate*, 1995.
2. P. Jonas, R. Charlson and H. Rodhe, *Aerosols in Climate Change*, 1994, eds. Houghton *et al.* (Cambridge Univ. Press, New York, 1995).
3. G. d'Almeida, *J. Geophy. Res.* **92** (1987) 3017.
4. H. W. Georgii and P. Warneck, *Global Aspects of Atmospheric Chemistry*, Vol. 161 (Springer, Berlin, 1999).
5. L. Schultz, Sahara dust transport over the North Atlantic Ocean-Model calculation and measurements in Saharan desert, 267, 1979.
6. J. M. Prospero, D. L. Savoie, T. N. Carlson and R. T. Nees, Monitoring Saharan aerosol transport by means of atmospheric turbidity measurements in Saharan dust: Mobilization, Transport, 171, 1979.
7. S.-U. Park and H.-J. In, *J. Geophy. Res.* **108**, D19 (2003) 4618, doi:10.1029/2003JD00348.
8. H.-J. In and S.-U. Park, *Atmos. Environ.* **37** (2003) 4625.
9. S.-U. Park and E.-H. Lee, *Atmos. Environ.* **38** (2004) 2155.
10. R. B. Husar, D. M. Tratt, B. A. Schichtel, S. R. Falke, F. Li, D. Jaffe, S. Gasso, T. Gill, N. S. Laulainen, F. Lu, M. C. Reheis, Y. Chun, D. Westphal, B. N. Holben, C. Guymard, I. McKendry, N. Kuring, G. C. Feldman, C. McClain, R. J. Frouin, J. Merrill, D. DuBois, F. Vignola, T. Murayama, S. Nickovic, W. E. Wilson, K. Sassen, N. Sugimoto and W. C. Malm, *J. Geophy. Res.* **106** (2001) 18,137.
11. H.-J. In and S.-U. Park, *Atmos. Environ.* **36** (2002) 4173.
12. L.-S. Chang and S.-U. Park, *Atmos. Environ.* **38** (2004) 4467.
13. G. A. Grell, J. Dudhia and D. R. Stauffer, A description of the 5th generation Penn State/NCAR mesoscale model (MM5). NCAR TECH. Note NCAR/TN-398, 1994, p. 117.
14. J. Dudhia, D. Grill, Y.-R. Guo, D. Hausen, K. Manning and W. Wang, PSU/NCAR mesoscale modeling system tutorial class notes (MM5 modeling system version 2) (1998).
15. J. T. Kiehl, J. J. Hack, G. B. Bonan, B. A. Boville, D. L. Williamson and P. J. Rasch, *J. Clim.* **11** (1998) 1131.
16. B. P. Briegleb, *J. Geophy. Res.* **97** (1992) 7603.
17. S.-U. Park, Proceedings of workshop of Asian dust, March 22, 2002, Korea meteorological Administration, Korea, 2002.
18. D. G. Streets, T. G. Bond, G. R. Carmichael, S. D. Fernandes, Q. Fu, D. He, Z. Klimout, S. M. Nelson, N. Y. Tsai, M. Q. Wang, J.-H. Woo and K. F. Yarber, *J. Geophy. Res.* **108**, D21 (2003) 8809, doi:10.1029/2002JD003093.

A NUMERICAL SIMULATION OF AN ASIAN DUST (HWANGSA) EVENT OBSERVED IN KOREA ON MARCH 10–12, 2004 USING THE MODIFIED ADAM MODEL

EUN-HEE LEE* and SOON-UNG PARK
School of Earth and Environmental Sciences Seoul National University
Seoul 151-742, Korea
**s94leh@snu.ac.kr*

A moderate Asian dust (Hwangsa) event was observed in Korea for the period of March 10–12, 2004. This event has been simulated using MM5 and the modified Asian Dust Aerosol Model (ADAM2). The ADAM model developed by Park and In and Park and Lee has been modified using the observed data obtained from the monitoring tower located at Duolun in Inner Mongolia. The modification has been done by comparing modeled and monitored meteorological parameters including the relative humidity, soil surface temperature, surface wind speed and the surface vegetation conditions that are used in dust emission conditions in the ADAM model. The ADAM2 is able to simulate more accurately the start, end and the dust peak times and dust concentrations observed in South Korea. As a result, the ADAM2 model is a useful tool to forecast the Asian dust (Hwangsa) event in Korea.

1. Introduction

Asian dust which is called “Hwangsa” in Korea and “Kosa” in Japan is a typical example of mineral aerosol frequently originating in the Gobi desert, Sand desert, Loess plateau, and barren mixed soil in northern China and Mongolia during the spring season.[1–3] The occurrence of large dust storms is often associated with catastrophic consequences for humans and their environment. Indeed, very severe dust storms were observed in Korea on March 21–23 and April 7–9, 2002 with an observed maximum PM_{10} concentration greater than $1500\,\mu g/m^3$ at most monitoring sites in South Korea.[2] These intense dust storms have caused natural disasters in Korea. The consequence of these severe events has given birth to the Asian Dust Aerosol Model (ADAM) in Korea in order to issue warnings to the public. Park and In[1] and Park and Lee[2] have used this model to simulate the severe dust-storm events occurring on March 21–23, 2002 and April 7–9, 2002 with successful results. However, the ADAM model tends to overestimate the observed dust concentrations in Korea for recently observed dust events.

Consequently, the purpose of this study is to improve the ADAM model by improving dust emission conditions and the surface vegetation distribution in the source region with the monitored meteorological data at Duolun in Inner Mongolia. The improved ADAM model (ADAM2) was employed to simulate the Hwangsa event that was observed in Korea from 10 to 12 March 2004.

2. Model Description

2.1. *The meteorological model*

The meteorological model used in this study is the nonhydrostatic version of the fifth-generation mesoscale model (MM5) developed at the Pennsylvania State University/National Center for Atmospheric Research employing the x, y and terrain following σ-coordinate system as in Ref. 3. The domain of the model is shown in Fig. 1. The domain includes major source regions of Asian dust: the Sand, Gobi, Loess, and Mixed soil areas.[1] The model has 150×120 grid points with a horizontal resolution of 30 km and 25 vertical layers. The simulation covers the period from 8 to 15 March 2004, for which the evolutionary feature of each dust storm is fully resolved in the model domain.

2.2. *The Asian dust aerosol model*

The ADAM model is an Eulerian dust-transport model that includes the specification of the dust source regions delineated by the statistical analysis of the dust data reported according to WMO specifications. So statistical analyses of dust emission conditions were derived for the four regions of Sand, Gobi, Loess, and mixed soil surface, with the dust emission flux being proportional to the fourth power of the friction velocity with modification of the land use types in each source–grid region. The suspended particle-size distribution was parametrized using the log-normal distributions of soil particle-size distribution bins in the source regions based on the concept of the minimally and fully dispersed particle-size distribution. The detailed description of the ADAM model is given in Park and In[1] and Park and Lee.[2] The ADAM model uses 11 size bins with the same logarithm intervals for particles of 0.1–37 μm in radius.

The estimation of dust emission amounts ranging from 0.1 to 37 μm in radius used in the ADAM model is given as

$$F_a = \left(1 - \sum_i f_i R_i\right) \times \alpha \times u_*^4 \quad \text{if } u_* \geq u_{*_t}, \tag{1}$$

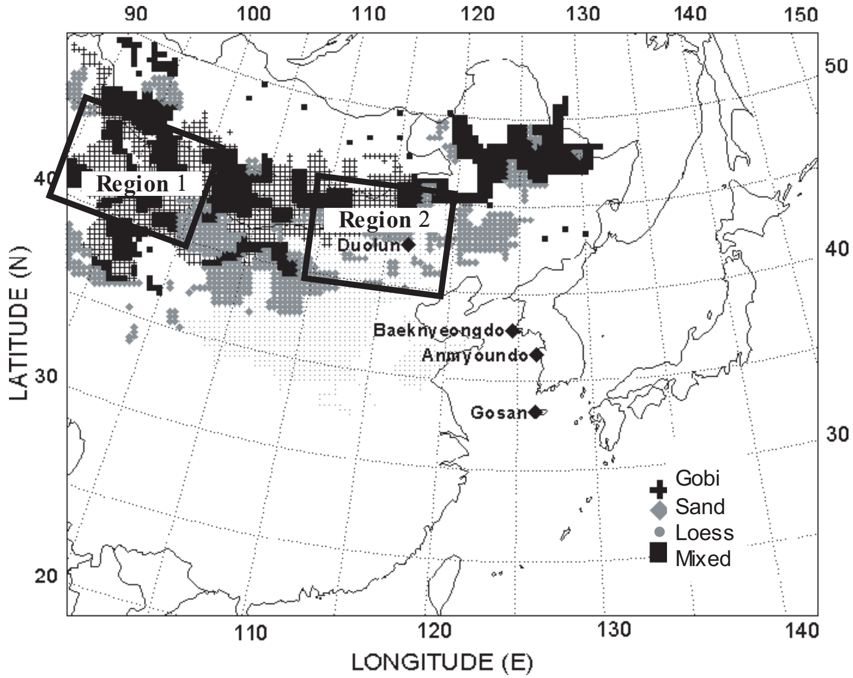

Fig. 1. The model domain and Asian dust source regions (++ Gobi, ◆◆ Sand, ● Loess and ■■ Mixed). Precipitation and vegetation index analyzes are given in Regions 1 and 2. Several PM_{10} monitoring sites in Korea are also shown.

where F_a is the dust flux from the surface (g/cm^2/s^1), u_* the friction velocity, u_{*_t} the threshold friction velocity, f_i the fractional coverage of vegetation type i in the dust-source grid and R_i is the reduction factor of vegetation type i given in Table 1, which is derived from the advanced very high-resolution radiometer (AVHRR) in the source region, and α is a constant that is determined by the soil type in the source region.[2]

3. Results

Figure 2 shows the time series of modeled PM_{10} concentrations averaged for the layers below 100 m, 100–1500 m and above 1500 m and the observed PM_{10} concentrations at Baeknyeongdo, Anmyeondo and Gosan in South Korea (Fig. 1) during the simulation period. The start and end time of the dust event are quite well simulated, indicating that the dust emission values in the ADAM model are satisfactory. However, simulated PM_{10} concentrations for the period of March 8–15, 2004 are highly overestimated compared

Table 1. USGS vegetation categories with the surface roughness length (Z_0) and the original dust-emission reduction factor (ADAM) and the modified value (ADAM2) in the ADAM model.

Type		Description	Z_0 (m)	Reduction factor (R)	
				ADAM	ADAM2
A	1	Urban and Built-up land	1.00	1.0	—
B	2	Dry Cropland and Pasture	0.02	0.4	0.9
C	3	Irrigated Cropland and Pasture	0.02	0.6	0.8
D	4	Mixed Dry/Irrigated Cropland and Pasture	0.02	0.5	0.8
E	5	Cropland/Grassland	0.02	0.5	0.9
F	6	Cropland/Woodland	0.02	0.7	0.8
G	7	Grassland	0.02	0.6	0.9
H	8	Shrubland	0.03	0.7	0.8
I	9	Mixed Shrub/Grassland	0.03	0.75	0.8
J	10	Savanna	0.02	0.8	—
K	11	Deciduous Broad leaf Forest	0.05	0.9	—
L	12	Deciduous Needle leaf Forest	0.05	0.9	—
M	13	Evergreen Broad leaf Forest	0.05	0.9	—
N	14	Evergreen Needle leaf Forest	0.05	0.9	—
O	15	Mixed Forest	0.05	0.9	—
P	16	Water	0.001	1.0	—
Q	17	Herbaceous Wet land	0.002	1.0	—
R	18	Wooded Wet land	0.003	1.0	—
S	19	Barren or sparsely vegetated land	0.01	0.1	0.2
T	20	Herbaceous Tundra	0.003	1.0	—
U	21	Wooded Tundra	0.003	1.0	—
V	22	Mixed Tundra	0.002	1.0	—
W	23	Bare ground Tundra	0.001	1.0	—
X	24	Snow or Ice	0.001	1.0	—

with observations, suggesting that some improvement in the specification of the dust emissions in the source region is required.

This discrepancy might have arisen due to the change in surface conditions in the source region. The maximum dust concentration in Fig. 2 is associated with the dust storms that occurred in central northern China and eastern Inner Mongolia. To examine this discrepancy, we have analyzed precipitation amount in the northwestern central part of China (Region 1 in Fig. 1) and the eastern part of Inner Mongolia (Region 2 in Fig. 1).

Table 2 shows the annual total precipitation amount in Regions 1 and 2 from 1998 to 2004. Since 1998, the annual total precipitation amount in Region 1 decreased to a minimum value of 44.8 mm in 2001 with a slight increase thereafter and the annual total precipitation amount in Region 2 decreased remarkably from 1999 to a minimum value of 265 mm in 2001,

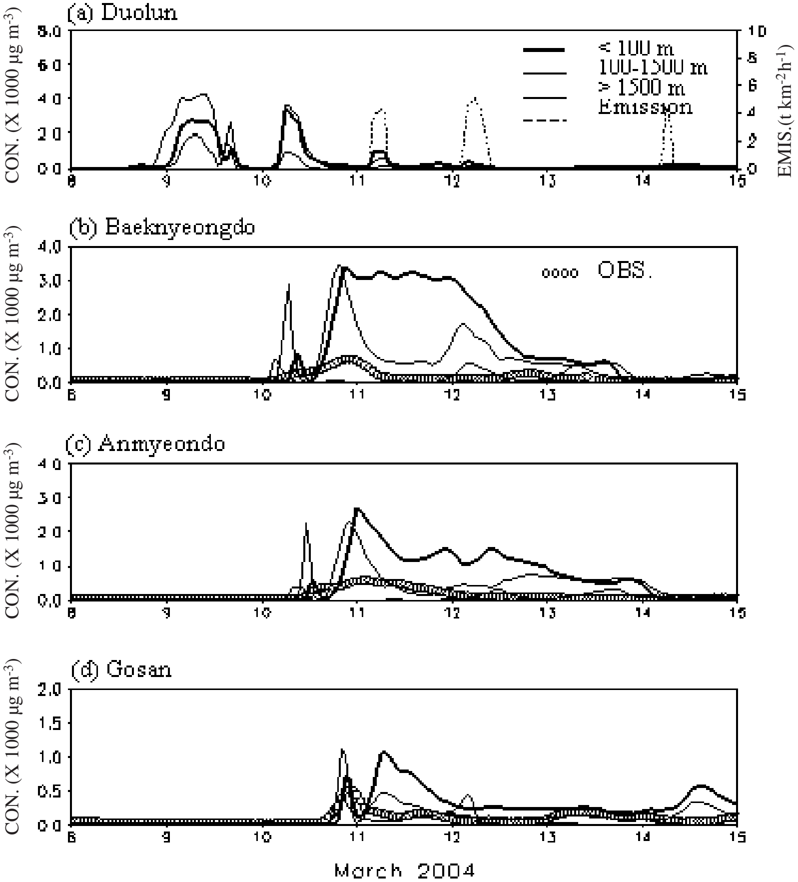

Fig. 2. Time series of modeled PM_{10} concentrations ($\times 10^3\,\mu g/m^3$) averaged for the layers of below 100 m (▬), 100–1500 m (—) and above 1500 m (—) above the ground is given at (a) Duolun in China, (b) Baeknyeongdo, (c) Anmyeondo and (d) Gosan in South Korea from the original ADAM model (ADAM1). The modeled dust emission ($ton/km^2/h$) at Duolun (- - -) and the observed PM_{10} concentration is denoted by “-o-o-”.

causing a wide spread of desertification in northern China.[4] The drought in Region 2 continued from 1999 to the spring of 2002. Thereafter the precipitation increased to above normal in 2003 (Table 2).

Figure 3 shows the monthly mean AVHRR normalized vegetation index averaged in each Region from 1998 to 2001 and for 19 years from 1982 to 2000. During the drought period (from 2000 to spring of 2002), the vegetation index is much lower compared with the long-term average value

Table 2. Annual total precipitation (mm) in Regions 1 and 2 from 1998 to 2004.

	1998	1999	2000	2001	2002	2003	2004 (Jan.–Sep.)
Region 1	82.0	80.9	54.4	44.8	58.7	58.5	35.8
Region 2	435.5	285.5	275.4	265.1	289.0	374.4	312.7

(a) Region 1

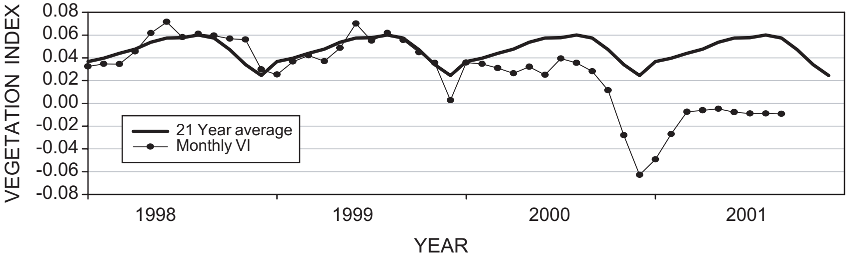

(b) Region 2

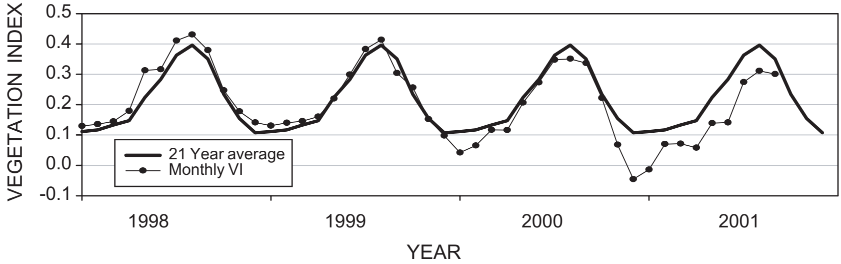

Fig. 3. The time series of monthly mean AVHRR Vegetation index (-●-●-) averaged in (a) Region 1 and (b) Region 2 with the averaged value for the period of 1998–2001 (▬).

in both Regions, especially in 2001 when the precipitation was a minimum. Since the data are available up to September 2001 only, the vegetation index during the vegetation recovery period of 2003 and 2004 is not shown in Fig. 3.

The above analysis clearly indicates that surface conditions in the Asian dust source regions have changed significantly after 2002, especially in the northeastern part of China, where the grassland is regenerating thereby reducing raised dust. To consider this in the ADAM model, the emission reduction factor in the ADAM model has been modified for the grasslands that are located to the east of 105°E and to the north of 40°N.

The modified reduction factors are given in Table 1 together with the original values used in the ADAM model.

Another possible source of the discrepancy between the simulated and observed dust concentration might arise from inadequate simulation of meteorological fields. Figure 4 compares the modeled meteorological data with the observed tower data at Duolun in Inner Mongolia during the simulation period.

One of the important conditions for the dust emission in the source region is the thawing of the top soil. This is not taken into account in the ADAM model since the meteorological model does not have an algorithm to predict the soil temperature. However, the model can predict the ground surface temperature. As seen in Fig. 4(b) the predicted ground surface temperature is as low as -6°C when the observed top soil temperature is just above freezing level (Figs. 4(a) and (b)).

The model simulated wind speed closely matches the observed wind speed at Duolun. The time period that the wind speed occurs above the threshold wind speed of 6 m/s coincides well with the observation, suggesting the suitability of the present threshold wind speed (Fig. 4(c)).

The model simulates higher relative humidity (Fig. 4(d)) of about 10%. The simulated friction velocities and those measured by a sonic anemometer are shown in Fig. 4(e). During the dust emission period (denoted by the thick overbars) the observed friction velocity is much lower than the modeled friction velocity by a ratio factor of 1:1.4, suggesting a modification to the model friction velocity may be required to estimate the dust emission amount more accurately using model output.

Based on analyzes mentioned above, the original ADAM model[1,2] has been altered to yield the modified ADAM model called "ADAM2" Table 3.

The ADAM2 model was used to simulate the Hwangsa event observed in Korea during the period from 10 to 12 March 2004. The resulting time series of PM_{10} concentrations is shown in Fig. 5. The ADAM2 model simulates quite well the start, end and dust peak times, and the maximum PM_{10} concentration in South Korea.

4. Conclusions

The modified ADAM model based on meteorological observations and surface conditions in the source region simulates well the start, end and the dust peak times, and the maximum PM_{10} concentration of the Asian dust event during the period March 10–12, 2004.

(a) Temperature

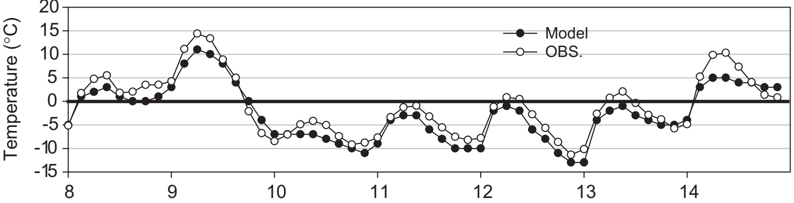

(b) Soil temperature

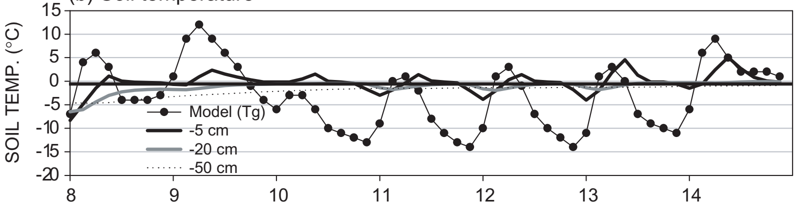

(c) Wind speed

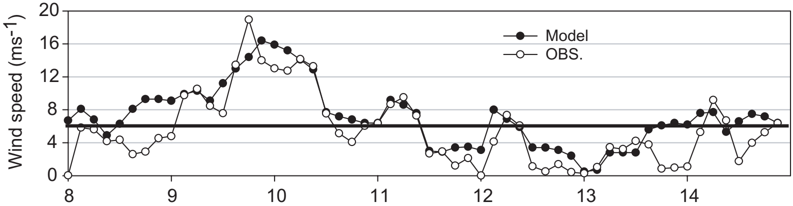

(d) Relative humidity

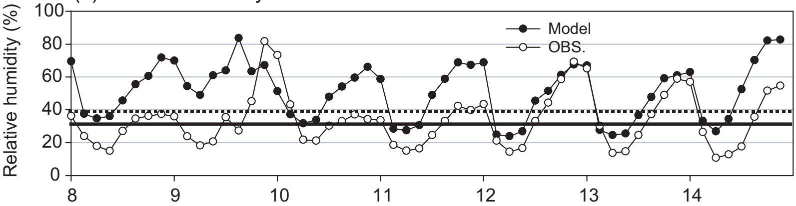

(e) Friction velocity

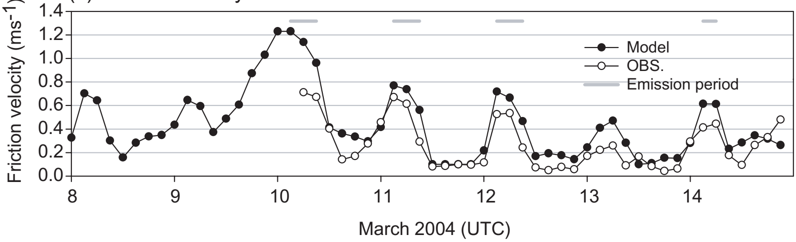

Fig. 4. Time series of modeled (●●) and observed (○○), (a) temperature (°C), (b) soil temperature with modeled ground surface temperature (°C), (c) wind speed (m/s), (d) relative humidity (%) and (e) friction velocity (m/s) at Duolun in Inner Mongolia during March 8–15, 2004. The overbars in (e) indicate dust-rise periods at Duolun.

Table 3. Conditions for raised dust in ADAM (A1) and ADAM2 (A2).

Soil	Threshold wind speed (m s^{-1})		Upper limit of RH (%)		Prec. (mm)		Top soil temp. (T_g °C)		Friction velocity	
type	A1	A2	A1	A2	A1	A2	A1	A2	A1	A2
Gobi	9.5	9.5	60	60	None		—	• $T_g \geq -2$°C: Full emission	—	$U_*/1.4$
Sand	7.5	7.5	35	45	None			• $-2 \leq T_g < -6$: Emission reduction of 1/3		
Loess	6.0	6.0	30	40	None			• $T_g < -6$: No emission		
Mixed	9.2	9.2	45	50	None					

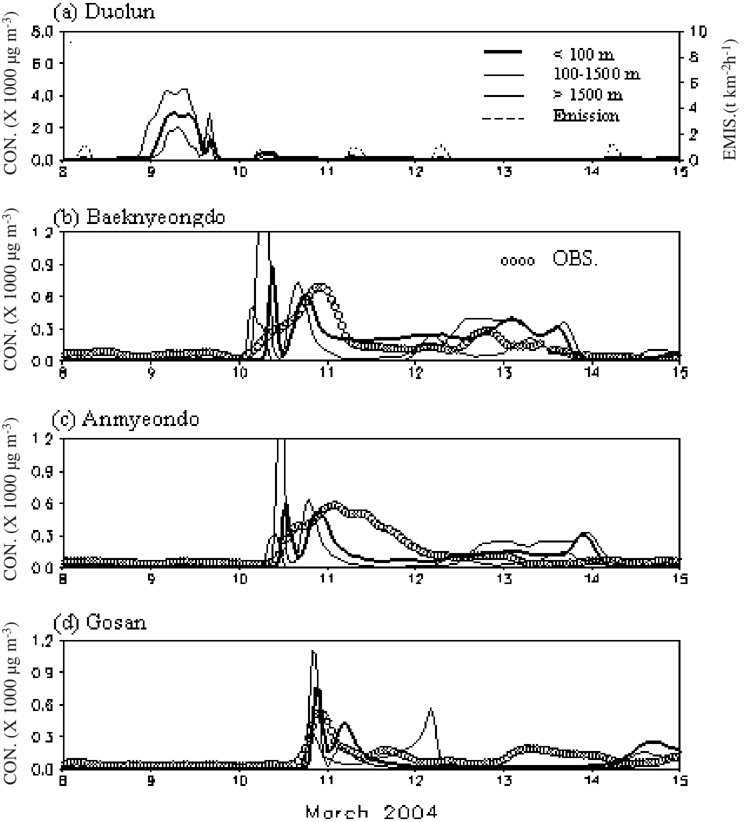

Fig. 5. As in Fig. 2 except for the results of ADAM2.

This study clearly indicates that the ADAM2 model with the proper emission reduction factor specified from accurate land–surface conditions and meteorological model output, has great potential to be used as an Asian dust forecasting tool in Korea. The forecasting system requires detailed monitoring of land-use type changes in the source region.

Acknowledgments

This research was partially supported by Climate Environment System Research Center that is funded by Korea Science and Engineering, the Ministry of Education under the Brain Korea 21 program and the Meteorological and Earthquake R&D Program funded by Korea Meteorological Administration.

References

1. S.-U. Park and H.-J. In, *J. Geophys. Res* **108**, (D19) (2003) 4618.
2. S.-U. Park and E.-H. Lee, *Atmos. Environ.* **38** (2004) 2155.
3. H.-J. In and S.-U. Park, *Atmos. Environ.* **36** (2002) 4173.
4. N. Bai and K. Zhang, *Proceedings of 7th International Joint Seminar on the Regional Deposition Processes in the Atmosphere*, November 20–22, 2001, Tsukuba, Japan, 2001.

A RADIATIVE TRANSFER MODEL FOR RADIATION COMPUTATIONS IN AN OCEAN–ATMOSPHERE SYSTEM

S. V. SALINAS* and S. C. LIEW†
Centre for Remote Imaging, Sensing and Processing
National University of Singapore, Blk. SOC 1, Level 3
Lower Kent Ridge Rd., Singapore 119260
**crsscsv@nus.edu.sg*
†*crslsc@nus.edu.sg*

We report a radiative transfer model for the atmosphere–ocean system based on the numerical solution of the radiative transfer equation. We use a modified radiative transfer code to handle multiple scattering inside the atmosphere and include a new surface reflection term to handle light reflection from a rough liquid surface including surface wind and wave age effects. The one-dimensional model atmosphere is solved via the widely known doubling and adding method and the ocean system is treated as a boundary condition to the problem. Model calculations and evaluation are performed for representative wind speeds and wave ages. The model can then be used for the analysis and interpretation of reflectance variability near a Sun glint region.

1. Introduction

Light reflection from calm windless surfaces has long been studied using the classical Fresnel and Snell's relations to represent specular reflection and medium refractive changes at the ocean–atmosphere boundary. Moreover, to represent the ocean–atmosphere interface, a smooth, flat boundary is usually employed. Under this assumption, Fresnel formulae can be easily incorporated to represent the specular reflection of the sea surface. However, smooth water surfaces are rarely encountered in nature, therefore a wind-roughed surface treatment is necessary to deal with sea surface reflection. Since the pioneering work of Cox and Munk,[1,2] who first investigated the probability distribution of wind generated liquid surface facets using the analysis of aerial photographs of the Sun glitter, it has been widely recognized that the dominant parameter that determines the sea surface roughness is the mean square slope (MSS) of the sea surface which is mainly related to short wind waves and other surface effects in a lesser degree. The reflectivity of the liquid surface can be computed using Cox and Munk[1,2] empirical formulation together with a normal probability distribution of water surface facets and applying Fresnel formulae to each surface facet as shown in Ref. 3. However, this approach do not include the influence of wave states or any of the physical properties of the surface on the computation of the MSS. In a recent work, Zhao and Toba[4] introduced an analytical method to calculate the MSS which is consistent with current empirical algorithms, especially at low wind speeds. The MSS is calculated by integrating a widely accepted wind-wave spectrum which includes the gravity-capillary regime into the formulation as well as the physical properties of the ocean boundary. This new treatment, coupled with linear wave theory is used here for the computation of the bi-directional reflectivity of the ocean surface. The radiative transfer equation is then solved using a modified one-dimensional radiative transfer code[5] based on the widely known doubling and adding method[6] with the ocean surface treated as a boundary condition to the problem. For the surface term, We use a method similar to Deuzé[3] with the exception that we compute the bi-directional reflectivity function directly in azimuth space and then Fourier transform the results via a FFT. In this way, the azimuth independent part of the radiative transfer equation is preserved and effectively solved by the doubling and adding algorithm and the interaction principle.[7]

2. Radiative Transfer

For a plane-parallel finite atmosphere with a solar source, the unidimensional radiative transfer equation for a single wavelength can be written as

$$\mu\frac{\partial I(\tau,\mu,\phi)}{\partial\tau} = I(\tau,\mu,\phi) - \frac{\varpi_0}{4\pi}\int_0^{2\pi}\int_{-1}^{+1} P(\tau,\mu,\phi;\mu',\phi')I(\tau,\mu',\phi')\mathrm{d}\mu'\,\mathrm{d}\phi' + \frac{\varpi_0}{4\pi}\mathrm{e}^{(\tau/\mu_s)}P(\tau,\mu,\phi;\mu_s,\phi_s)F_s, \tag{1}$$

where τ represents the optical depth, ϖ_0 is the single scattering albedo, (μ,ϕ) and (μ',ϕ') are the cosine of the zenith and azimuth angle of the reflected and incident light beams, respectively, F_s refers to the total solar flux at the top of the atmosphere, $P(\tau,\mu,\phi;\mu',\phi')$ the scattering matrix, and I represents the intensity of the radiation.

There are several methods to solve the radiative transfer equation for a plane-parallel atmosphere, several of these methods are described in Ref. 6. However, to solve Eq. (1), two boundary conditions must be specified: the incident radiation at the top of the atmosphere $I(0, \mu, \phi)$ and surface reflection at the bottom of the atmosphere $I(\tau, -\mu, \phi)$. For near-UV to near-IR, there is no source other than direct sunlight at the top of the atmosphere. There is, in general, a source at the bottom of the atmosphere from reflection of the surface. The surface reflected radiation is a function of the downward radiation incident upon it. If the surface is a pure specular reflector, then the full reflection matrix can be written in terms of Fresnel equations. In reality however, the rough sea surface cannot assumed to behave like a pure specular reflector and as such a bi-directional reflectance distribution function (BDRF) is required to model sea surface reflectivity.

2.1. *Rough sea surface reflection: Cox and Munk MSS*

Computing the scattering of solar radiation for a smooth, specular liquid surface requires only the direct application of Fresnel equations. However, for the case of a rough liquid surface, these equations are no longer directly applicable since specular reflection will only exist for suitable tilted liquid surface facets. According to Cox and Munk[1,2] study of the Sun glitter, the probability distribution of water surface facet normals under the influence of the wind is given by the following Gaussian distribution (isotropic rough surface, independent of wind-direction):

$$F(\mu_n, \phi_n) = \frac{1}{\pi\sigma^2} \exp\left(-\frac{1-\mu_n^2}{\delta^2\mu_n^2}\right). \tag{2}$$

The term δ^2 is called the mean-square slope (MSS) of the sea surface. Cox and Munk,[1,2] based on their photographs of the Sun glint, formulated a linear relation between the MSS and the wind speed V_w (measured at 12.5 m height) given by the following equation,

$$\delta^2 = 0.003 + 0.00512 V_w. \tag{3}$$

This form of the MSS has been widely used by the scientific community over the years to describe specular reflection from sea surface wave slopes.

2.2. *Rough sea surface reflection: Zhao and Toba MSS*

In a recent work, Zhao and Toba[4] proposed a spectral approach to determine the MSS from radar altimeter data. The proposal includes the integration for a wind-wave spectrum but extended to include the gravity-capillary wave range. Based on this wave spectrum, they obtained the following analytical relation for the MSS function,

$$\begin{aligned}\delta^2 &= 2\alpha C_D^{1/2}\beta^{-1}\\ &\quad+\frac{3}{2}\alpha C_D^{1/2}\beta^{-1}\left(\ln\frac{a+\sqrt{a^2+81g^2/(\beta V_{10})^4}}{9g/(\beta V_{10})^2}-\ln\frac{a+\sqrt{a^2+k_d^2}}{k_d}\right),\end{aligned} \tag{4}$$

here C_D is the drag coefficient of the sea surface. $\beta = c_p/V_{10}$ is the wave age with $c_p = g/\omega_p$ as the phase speed of waves corresponding to the peak frequency ω_p and V_{10} is the local wind speed a 10 m above sea level, k_d is the cut-off wave number for high wave numbers (in the near-IR the last term of Eq. (4) is negligible) and $a = \sqrt{g/\gamma_s}$ is used for convenience in the notation. For convenience on the interpretation of wave slopes, we have plotted (Fig. 1) the more intuitive root mean square slope (RMSS) to have a better idea of the tilting caused by the wind interaction with the sea surface. For further discussion and details about algorithm validation and comparison with experimental data, the reader is encouraged to see Ref. 4.

Several studies[8–10] suggested that there was evidence of nonwind-dependent factors on the determination of the MSS from altimeter measurements. The largest factor appears to be the degree of sea development which is known as wave age (characterized by the phase speed of the dominant wave and the wind speed measured at a height of 10 m).

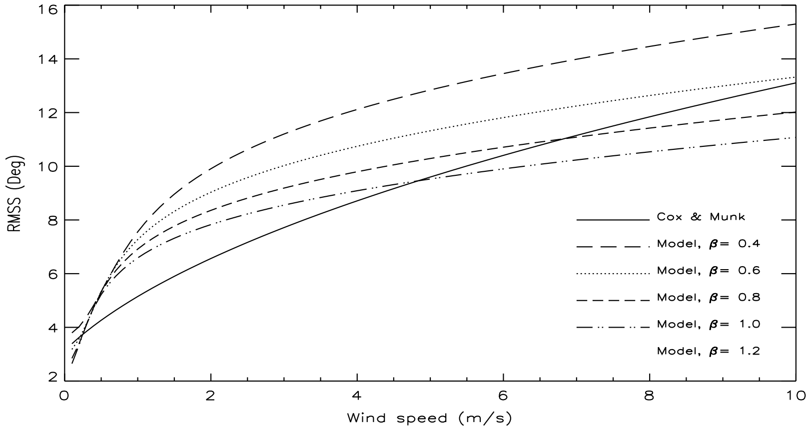

Fig. 1. Root mean-square slope from Eq. (4) for several wave ages (β's) including a comparison with Cox and Munk empirical RMSS of the sea surface.

The first wave-dependent algorithms appeared in the work of Glazman and Pilorz[8] and was further extended by Glazman and Greysukh.[11] However, the inclusion of wave states on the computation of the MSS function requires the selection and integration of a representative wave spectrum. A detailed study of frequency spectra of ocean waves can be found in Ref. 12.

3. Radiation Modeling

In this section, we will give a brief description of how we compute TOA reflectance (the so-called remote sensing reflectance) which is routinely used for a process known as atmospheric correction. Further details regarding the process of atmospheric correction can be found in the work of Gordon,[13,14] for applications to satellite imagery and ocean remote sensing see for example Ref. 15.

3.1. *Top of the atmosphere reflectance*

For remote sensing applications, usually the top of the atmosphere reflectance (TOA) rather than the physical irradiance are commonly used, therefore we write,

$$\rho(\lambda) = \frac{\pi L}{F_0 \cos(\theta_0)}. \tag{5}$$

Here, L represents the up-welling radiance, F_0 represents the extraterrestrial solar irradiance (or solar flux) and θ_0 represents the solar zenith angle. The total reflectance ρ_t at a given wavelength λ is the sum of the contributions from stratospheric gas (absorption and scattering), tropospheric aerosols scattering and ocean surface processes like Sun glint, foam and subsurface scattering diminished by the transmittance of the overlaying atmospheric layers. In general, the TOA reflectance can be decomposed into the following components, each of them defining a physical process inside the atmosphere or in the ocean: The reflectance due to multiple scattering by air molecules (Rayleigh), reflectance from multiple scattering by atmospheric aerosols, reflectance by interaction between Rayleigh and aerosol scattering, reflectance emerging from the sea water, the reflectance due to the Sun glint and the reflectance from white-caps at the air-sea interface. In this work, only atmospheric processes (molecular and aerosol scattering) and surface processes (Sunglint) are considered.

3.2. *Wind and wind-wave effects on TOA reflectance*

The analytical algorithm mentioned in Sec. 2.2 can now be applied to model specular reflection from a rough liquid surface, such as the ocean, as seen from a remote sensing satellite. However, in order to evaluate the top of the atmosphere radiances or reflectances, we need to include atmospheric processes such as aerosol scattering and absorption processes by the underlying atmosphere. In our model atmosphere, we have included Rayleigh and maritime aerosol scattering, each of them being of importance especially in the optical and near-IR region and ozone gas absorption. The model atmosphere is divided into fifty atmospheric layers resolving the aerosols, gas molecules and ozone vertical distribution (from 0 to 120 km altitude with aerosols in the lower 10 km). Molecular scattering is described by a Rayleigh phase function. The aerosol scattering phase function is modeled using refractive indexes provided by Shettle[16] as a function of relative humidity (Maritime aerosols with 98% rel. hum.). All calculations were done for an atmosphere at a wavelength of 0.551 μm and an optical depth of approximately 0.14. For the surface term part, refractive indexes of pure water at a given wavelength were taken from Ref. 17, a correction was applied to account for water salinity as in Ref. 18.

Plots in Fig. 2 show the Sun glint pattern simulation using both, Cox and Munk[1,2] formulation and the new MSS (at several wave ages) computed using the new wind-wave formulation. The solar angle is about 24° and the calculations were done for wind speeds of 2.0 and 8.0 m/s. These values were chosen as representative examples for low and intermediate winds.

From both panels of Fig. 2, we can qualify the effect of surface wind speed on the Sun glint pattern. As expected, at low wind speed, a smoother surface is encountered by the down-welling radiation field, therefore a well defined glint pattern would dominate. In both cases, the glint pattern is predominantly driven by the direct solar beam. However, if wind speed increases, the liquid surface becomes rougher and the developing wave pattern drives the amount of scattered photons away from the specular direction of the Sun. Hence, at higher wind speed, the sea surface increases the amount of diffuse radiation as the surface becomes rougher. This effect that can be easily observed over the ocean when wind conditions are rapidly changing, the surface roughness will increase and the glint pattern will be less dominant at higher speeds.

Comparing each individual plot from Fig. 2, we see that the Cox and Munk[1,2] formulation shows stronger glint reflectance as compared with

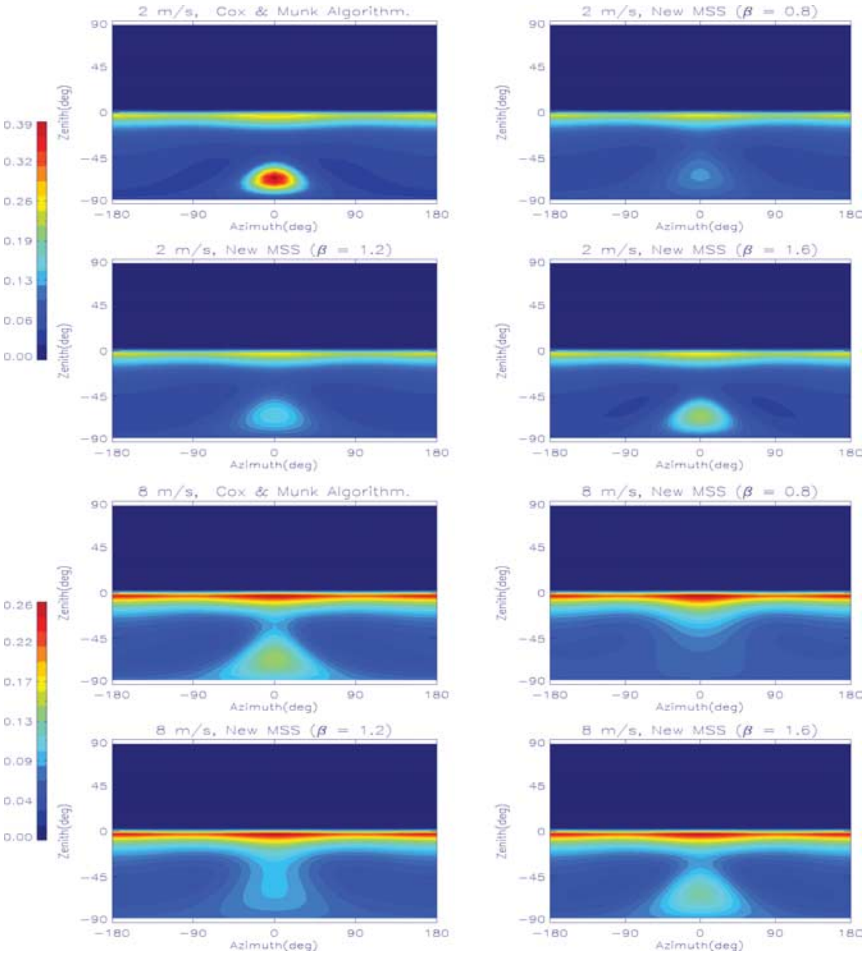

2 m/s, Cox & Munk Algorithm.

2 m/s, New MSS (β = 0.8)

2 m/s, New MSS (β = 1.2)

2 m/s, New MSS (β = 1.6)

8 m/s, Cox & Munk Algorithm.

8 m/s, New MSS (β = 0.8)

8 m/s, New MSS (β = 1.2)

8 m/s, New MSS (β = 1.6)

Fig. 2. Simulated reflectances at the TOA for a wind speed of 2 m/s (upper panel) and 8 m/s (lower panel) using both, Cox and Munk and the new wind-wave formulation. Wind-wave calculations are done for wave ages $\beta = 0.4$, 0.8 and 1.6.

the glint reflectance obtained with the new formulation, at the same wind speed, specially for the low speed case (e.g. 2 m/s). This observation can be explained with the help of Fig. 1. There we see that at low wind speed, the empirical Cox and Munk[1,2] formulation is equivalent to the new formulation only on the high wave age region ($\beta > 1.2$), therefore the high reflectivity observed on the simulated Sun glint is a direct effect of wave age. On the other hand, at low and intermediate wave age and high wind speed (e.g. 8 m/s), the wind-wave formulation is comparable with the Cox and Munk[1,2] method. This quantitative correspondence is expected since the Cox and Munk[1,2] formulation was empirically obtained from a wide distribution of wind-wave states and as such, it cannot discriminate individual wave states. This fact is overcome with the new formulation which is able not only to include wind-driven effects but also the influence of the sea state (wave age). This new formulation give us a new tool to quantitatively study the transfer of radiation in an atmosphere–ocean system by considering wind and sea state effects.

4. Conclusions and Further References

In this paper, we have reported a numerical model for radiative transfer calculations on the atmosphere–ocean system. The present model uses the liquid sea surface as a boundary condition, taking into account the influence of wind-speed and wave age on the sea surface roughness. The algorithm is able to compute TOA reflectance for low and high wind speeds using a new wind-wave formulation. We consider this to be an initial proof of concept exercise, the main aim being on the performance of the implementation and its evaluation when compared with other existing formulations. For further application to remote sensing data imagery the reader is encouraged to see Ref. 19 where the authors apply the present model to evaluate the variability of MODIS reflectance at the visible and near IR regions. MODIS reflectance variability is interpreted by considering both wind and wind-wave effects on the sea surface roughness which directly influences the observed Sun glint pattern.

References

1. C. Cox and W. H. Munk, *J. Opt. Soc. Am.* **44** (1954) 838–850.
2. C. Cox and W. H. Munk, *J. Mar. Res.* **13** (1954) 198–227.
3. J. L. Deuzé, M. Herman and R. Santer, *J. Quant. Spectrosc. Radiat. Transfer* **41** (1989) 483–494.
4. D. Zhao and Y. Toba, *J. Oceanogr. Soc. Jpn.* **59** (2003) 235–244.
5. K. F. Evans and G. L. Stephens, *J. Quant. Spectrosc. Radiat. Transfer* **46** (1991) 413–423.
6. J. Lenoble, *Radiative Transfer in Scattering and Absorbing Atmospheres: Standard Computational Procedures* (Deepak Publishing, Hampton, Virginia, 1995).

7. R. M. Goody and Y. L. Yung, *Atmospheric Radiation: Theoretical Basis* (Oxford University Press, New York, 1989).
8. R. E. Glazman and S. H. Pilorz, *J. Geophys. Res.* **95**, 14 (1990) 2857–2870.
9. J. M. Lefevre, J. Barckicke and Y. Menard, *J. Geophys. Res.* **99**, 18 (1994) 25,035.
10. D. Vandemark, J. B. Edson and B. Chapron, *J. Atmos. Oceanic Tech.* **4** (1997) 716–722.
11. R. E. Glazman and A. Greysukh, *J. Geophys. Res.* **98**, 17 (1993) 2475–2484.
12. R. M. Stanislaw, *Ocean Surface Waves: Their Physics and Prediction* (World Scientific Publishing, Singapore, 1996).
13. H. R. Gordon, *J. Geophys. Res.* **102**, 11 (1997) 17,081–17,106.
14. H. R. Gordon and A. Y. Morel, *Remote Assesment of Ocean Color for Interpretation of Satellite Visible Imagery: A Review* (Springer Verlag, New York, 1983).
15. R. M. Chomko and H. R. Gordon, *Appl. Opt.* **40**, 18 (2001) 2973.
16. E. P. Shettle and R. W. Fenn, *Models for the Aerosols of the Lower Atmosphere and the Effects of Humidity Variations on their Optical Properties.* (AFGL-TR-79-0214, Air Force Geophysics Laboratory, Hanscomb Airforce base, Mass. 1979).
17. G. M. Hale and M. R. Querry, *Appl. Opt.* **12–3** (1973) 555–563.
18. D. Friedman, *Appl. Opt.* **8**, 10 (1969) 2073–2078.
19. S. V. Salinas and S. C. Liew, *Remote Sens. Environ.*, (2006, under review).
20. Y. M. Liu, Y. Su, X. H. Yan and W. T. Liu, *J. Atmos. Oceanic Tech.* **17** (2000) 1092–1105.

BLUElink> OPERATIONAL OCEAN PREDICTION IN AUSTRALIA

GARY B. BRASSINGTON*,†, PETER R. OKE‡ and TIM PUGH*
Bureau of Meteorology Research Centre
P.O. Box 1289K, Melbourne 3001, Australia
†*g.brassington@bom.gov.au*

‡*CSIRO Marine and Atmospheric Research*
Hobart 7000, Australia
‡*peter.oke@csiro.au*

The Bureau of Meteorology is scheduled in 2007 to expand its oceanographic services to include operational mesoscale ocean forecasts. BLUElink> is a joint initiative of the Bureau of Meteorology, Commonwealth Scientific and Industrial Research Organisation and the Royal Australian Navy to develop this capability. The ocean model and data assimilation system have successfully completed an ocean reanalysis over the period 1992–2005 based on historical *in situ* and satellite altimetry observations and reanalyzed atmospheric fluxes. The model and assimilation components are being prepared with near real-time observations and atmospheric forecasts for operational trials.

1. Introduction

Operational oceanography is a relatively new capability, which is following on from the on-going and successful implementation of the Global Ocean Observing System (GOOS). Operational oceanography, in this context, refers to the hindcast, nowcast and forecast of the three-dimensional ocean state (temperature, salinity and pressure) and currents for short-range timescales out to one month. A pilot project called the Global Ocean Data Assimilation Experiment (GODAE)[1] has set out a vision for supporting the development of data assimilation of GOOS into state of the art models of the global ocean circulation in near real-time (NRT). GODAE promotes the sharing of data, standardising of metrics for model intercomparisons and supporting common infrastructure, formats and protocols for data servicing. Several GODAE server nodes in both the USA[2] and Europe[3] now provide public domain access to NRT satellite and profile observational data. BLUElink> is an Australian government initiative to develop the Ocean Model Analysis and Prediction System (OceanMAPS) for operational implementation at the Bureau of Meteorology (Bureau).

2. Oceanographic Data

Observational oceanography has seen a rapid expansion in earth observing instrumentation over the past two decades driven by the need to observe the climate system and conduct research into climate change science. The International Ocean Commission has implemented GOOS permanently. NASA, ESA and CNES have supported a number of remote sensing satellite programs including the Earth Observing System.[4] Some of the oceanographic variables being remotely observed together with the instrumented satellites and launch dates are outlined in Table 1.

In addition to satellite oceanography several *in situ* observational programmes have been undertaken including: Ship of Opportunity Program (SOOP) that deploy Expendable Bathy-Thermograph (XBT), Tropical Atmosphere Ocean (TAO) that maintains a network of moorings in the tropical Pacific and Argo, a program to deploy autonomous vertical profiling drifters. A significant number of these instruments contribute to the NRT ocean observing system, which are routinely distributed by the World Meteorological Organisation's Global Telecommunications System (GTS) as well as internet servers.

Accurate bathymetry is essential for the representation of ocean circulation and shelf current systems. BLUElink> has blended analyzed gridded products from Geoscience Australia including a 1 km resolution bathymetry dataset for the Australian region with global datasets from the US Navy. Ocean models are forced at the surface by atmospheric fluxes of momentum, heat and fresh water. Atmospheric forcing is available at the Bureau from Numerical Weather Prediction (NWP) systems run twice daily. The

Table 1. Earth observing satellites measuring ocean related variables that contribute to the near real-time global ocean observing system.

Variables	Instruments	Launch
Sea surface temperature	AVHRR,	. . . , 2000, 2002
	AATSR, AMSR-E	2001
		2001
Sea surface height	Topex-Poseidon,	1992
	GFO	1998
	Jason-1,	2001
	ENVISAT	2002
Sea surface salinity	Aquarius	2002
Wind stress	QuikSCAT	1999

Bureau supports the Global Assimilation and Prediction System[5] (GASP) and the Limited Area Prediction System[6] for the Australian region.

3. Operational Ocean Prediction System

The Ocean Model Analysis and Prediction System (OceanMAPS) is based on the Ocean Forecast Australia Model (OFAM),[7] the BLUElink> Ocean Data Assimilation System (BODAS),[8] a data management system and enhanced surface winds from NWP and high-resolution SST products. The system is implemented at the Bureau/CSIRO High Performance Computing and Communications Centre (HPCCC) which is presently based on the NEC SX6 machine.

3.1. *Ocean model development*

The Australian scientific community has a long and on-going relationship with Geophysical Fluid Dynamics Laboratory to adapt the Modular Ocean Model (MOM) software for Australian climate research applications. MOM Version4[9] is optimised for a scalable parallel architecture. This presents issues for performance of the software on alternative architectures such as the parallel vector NEC SX6 at the HPCCC. OFAM includes optimisation for the NEC SX6 with excellent results.

The OFAM grid has been designed as a global model, to avoid complexities associated with open boundary conditions. The Australian region has 10 km horizontal resolution, which resolves mesoscale ocean variability. In order to minimise the costs of the model, the grid employs lower resolutions outside the Australian region as shown in Fig. 1, where the white dots

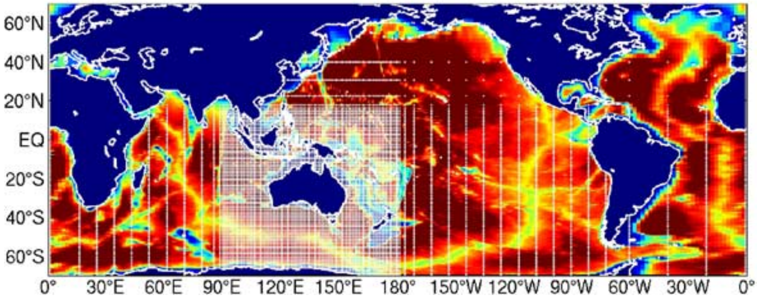

Fig. 1. Ocean Forecast Australia Model horizontal grid. Water cells are colored according the depth of bathymetry, every 10th grid point is shown as a white dot.

represent every 10th grid point. The vertical grid is comprised of 47 levels, with the top 20 levels at a resolution of 10 m. Each three-dimensional variable has dimension 1191 × 968 × 47 and a single snapshot is approximately 250 M bytes. A single snapshot of the five prognostic variables of the model is 1.2 Gbytes.

The performance of the OFAM on the NEC SX6 has been measured during two ocean model only integrations (so called "spinup") using ERA40.[10] The first integration was performed using MOM4p0b, which included the leap-frog time integration scheme and neutral physics using a baroclinic timestep of 300 s. This was performed on 21 processors across three nodes sustaining 20.3 Gflops. The second integration was performed using MOM4p0d, which included a new time integration scheme without neutral physics using a baroclinic timestep of 600 s. This was performed on 42 processors across six nodes sustaining 31.8 Gflops demonstrating some problems in scalability of the MOM software. The usage values are summarised in Table 2. OFAM's I/O requirements are outlined in Table 3 and include a complete ocean state specification either as initial conditions or a restart, O(5) Gbytes.

3.2. *Data assimilation*

BODAS[8] is a new software package developed to perform a multi-variate analysis based on statistics derived from the global ocean forecast system. The key feature of BODAS is the way it defines the background error covariances which is based on the stationary covariance of an ensemble

Table 2. Performance of OFAM (MOM4) on the NEC SX6.

	Spinup I	Spinup II
Nodes	3	6
Cpu's (total)	21	42
Memory (total)	∼86 GBytes	∼114 GBytes
Cputime/model day	20 min	11.5 min
Sustained flops	20.3 Gflops	31.8 Gflops

Table 3. Input files required for the Ocean Forecast Australia Model.

Input files	Size
Grid specification	∼400 MBytes
Restart	∼5 GBytes
NWP surface fluxes	∼150 MBytes
SST analysis	23 MBytes

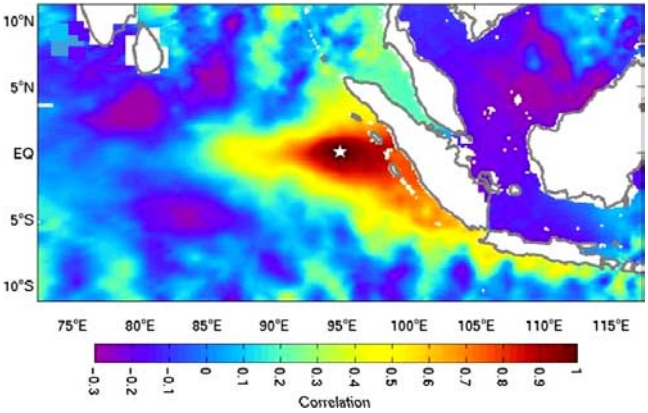

Fig. 2. Horizontal spatial correlations of sea surface height anomalies based on an ensemble of modelled states (a) Tasmania, (b) Indonesia (adapted from Ref. 8).

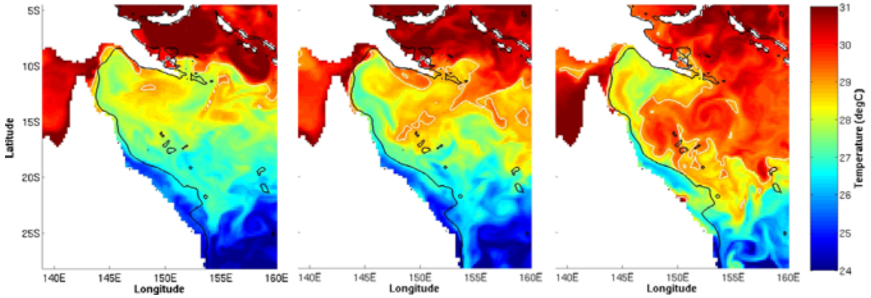

Fig. 3. BRAN surface temperature (10 m) in the Coral Sea for the January 6, 2000–2002. The 29 degree isotherm is represented by the white contour. The 200 m isobath is represented by the black contour.

of intraseasonal anomalies derived from a 9-year spinup integration of the ocean model without data assimilation. An example of the spatial structure of the ensemble covariances is shown in Fig. 2 for a location, indicated by the star, situated off Indonesia with the immediate surroundings. This example appears to represent the covariability associated with an equatorial Kelvin wave and its coastal extension (the positive correlations); and a Rossby wave pair (the negative correlations near 80°E) associated with the equatorial wave guide of the Indian Ocean.

3.3. *Ocean reanalysis*

OFAM and BODAS have been applied to construct an ocean reanalysis for the period 1992–2005. The BLUElink> ReANalysis (BRAN)[7] uses delayed mode observations including along track sea-level anomalies from altimetry (T/P, ERS, GFO, Jason, ENVISAT), coastal tide gauges, *in-situ* temperature and salinity profiles (WOCE, TAO, Argo, XBT) and analysed atmospheric forcing, ERA40.[10] Assimilation is performed every three model days. BRAN represents the first eddy-resolving ocean analysis for the Australian region. Analyses show skill in surface currents as compared with surface drifter observations.[8] An example of the analysed flow for sea surface temperature is shown in Fig. 3 for the Coral Sea. The three figures illustrate both the eddy scale variability as well as interannual variability for January 1, 2000–2002. The extensive warm intrusion shown in 2002 corresponds to a year of wide spread coral bleaching in the Great Barrier Reef.

BODAS was parallelised into 40 zonal sections submitted as single processor jobs. BODAS uses a stationary set of background error covariance statistics, which is based on a 72 member ensemble of model anomalies, O(15) Gbytes.

3.4. *Operational environment*

The Bureau's operations branch has the central responsibility for issuing meteorological analyses and predictions and distributing this information to the community through a network of regional forecast centers. In addition to meteorological forecasts, the Bureau also produces a range of other services in climate, hydrology, and oceanography. Oceanographic services at present cover a modest range of operational products including, tides, sea surface and subsurface temperature analyses and wave forecasts. The implementation of a high-resolution three-dimensional ocean state analysis and forecast system represents a major upgrade in computational resource and servicing requirements.

The high performance computational infrastructure that supports the operations branch is managed through the HPCCC. The core system, an NEC SX6, is accessed through an NQS based queue system that provides pre-emptive priority service to operational jobs while still providing services for research and development tasks performed by other sections of the Bureau and CSIRO. The SX6 is front-ended by dual NEC TX7 servers, each having 16 CPU and 16GB of memory. The TX7s provide global file system services for the SX6 nodes, and also scalar services for tasks associated with file transfers and data handling. Access to this common high-performance computing facility has been critical to the success of the BLUElink> project to date.

The SX6 includes high bandwidth, large scale storage and large shared memory per node that enable all of the data required for OceanMAPS to be stored for online operations. This structure minimises the interaction of the operational models with archive devices to post processing storage. The schedule for OceanMAPS is dependent on three inputs that are handled by the data management system, (a) NRT observations, (b) NWP surface fluxes, and (c) Sea surface temperature analyses. The system includes an analysis and forecast cycle that depends on the data management system for handling the distribution and servicing of products.

The Bureau maintains communications with a variety of networks to support NRT observation retrievals and data distribution. The majority of ocean profile observations are obtained from the GTS. Satellite observations such as sea surface anomalies from JASON-1 are pushed from OCEANIDS and available approximately 5–7 hrs behind real-time. ENVISAT is obtained from ESA on a 3 day delay.

Operational systems are designed to perform robustly to a regular schedule. The operational ocean system is planned to produce forecasts out to 7 days, twice per week. The prototype schedule includes: a symmetric analysis cycle for high-quality analyses, an asymmetric analysis cycle for forecast initial conditions and a forecast cycle. The symmetric analysis uses a symmetric observation window which is constrained by the time scale of one complete attimeter orbit (∼3 days behind real time) and is repeated daily using 3-day old analysed NWP fluxes. The asymmetric cycle uses an off-centred observation window and produces a nowcast and initial condition for the forecast. Both the analyses and forecasts depend on the availability of NWP fluxes and SST analyses. Both of these operational products have unique schedules. GASP is integrated twice daily at 0 UTC and 12 UTC while the analysis is performed every 6 hrs. SST is generated daily for the local region and weekly for the global domain. A forecast is then produced using NWP forecasts and fixed SST analyses (the boundary conditions of the NWP).

The Bureau has recently implemented the Meteorological Archival and Retrieval System (MARS) to serve as the primary meteorological database. This system was developed by ECMWF and was designed for storage of NWP output. The system supports two file formats Gridded Binary (GRIB) and Binary Universal Form for the Representation of meteorological data (BUFR). Neither of these two formats are widely used or supported outside this community by other centres or software developers. The Bureau has developed code to convert between file formats such as NetCDF and GRIB and BUFR.

Data management and exchange in the BLUElink> project involves several emerging standards. This has involved significant development of new systems, including the integration of the back-end database with available OPeNDAP servers. The push to standardisation is often hard to justify in the course of a single project, and can seem like more risk than reward. The advantage of enabling these standards, however, rather than relying on technologies such as FTP, is that it enables data sharing in a highly automated fashion. Just as XML and machine-independent data standards are becoming increasingly popular in business, so scientific standards will become increasingly popular in institutions. OPeNDAP, an openly published data exchange specification, allows tighter integration between heterogeneous applications, ultimately reducing the effort of end users and application developers in accepting new data sources. Putting in the additional effort to use open technologies will encourage faster take-up across the community, allowing smaller projects to achieve high-level goals faster. OPeNDAP has the advantage of being highly scalable. Its ability to subselect data on the server side allows data providers to reduce bandwidth by sending only the data which is requested by the client. Highly flexible, OPeNDAP servers can be used to both aggregate external data sources into a single format, easing the task of integrating new data into existing applications, or as a universal publishing mechanism. The ability to abstract away the problem of data exchange is a powerful enabler of new technologies.

4. Conclusion

The objective of BLUElink> is to produce the first operational forecasts of mesoscale ocean circulation for the Australian region. BLUElink> is halfway through the four-year contract period and will transition in focus from research and development to operational trials in 2006. The scale of the problem being undertaken is at the high-end of high performance computing and data management and will continue to pose interesting challenges to the Bureau. The development of this system has been constrained in its design to deliver the capability within the project period. There are numerous areas that have been identified for further development in a potential follow-on project and detailed analyses of the performance will offer additional insight. The scale of the analysis problem ensures that full use must be made of the wider research community. Connectivity and cost-effective distribution of data to this community is a critical activity.

Acknowledgment

This research is supported by the BLUElink project, Bureau of Meteorology, CSIRO and the Royal Australian Navy. The authors gratefully acknowledge the project leaders Andreas Schiller and Neville Smith and several other BLUElink team members for their valuable contributions. Atmospheric analyses were provided by ECMWF, satellite altimetry is provided by NASA, AVISO and NOAA. Bathymetry is derived from datasets from Geoscience Australia and the US Navy.

References

1. N. Smith and M. Lefebvre, *International Symposium*, Biarritz, October 15–17, (1997).
2. Naval Meteorology and Oceanography Command, <http://www.usgodae.org/> (2005).
3. MERSEA/GMES, http://strand1.mersea.eu.org/ (2005).
4. A. McClung, http://eospso.gsfc.nasa.gov/, (2005).
5. R. Seaman, W. Bourke, P. Steinle, T. Hart, G. Embery, M. Naughton and L. Rikus, *Aust. Met. Mag.* **44** (1995) 1–18.
6. K. Puri, G. Dietachmayer, G. A. Mills, N. E. Davidson, R. A. Bowen and L. W. Logan, *Aust. Met. Mag.* **47** (1998) 203–233.
7. A. Schiller, P. R. Oke, G. B. Brassington, R. Fiedler, D. Griffin, J. Mansbridge, K. Ridgeway and N. R. Smith, Eddy-resolving Ocean Circulation in the Asian-Australian region inferred from an ocean reanalysis effort (in press).
8. P. R. Oke, A. Schiller, D. Griffin and G. B. Brassington, Ensemble data assimilation for an eddy-resolving ocean model of the Australian region, *Q. J. R. Meteorol. Soc.* (in press).
9. S. M. Griffies, M. J. Harrison, R. C. Pacanowski and A. Rosati, A Technical Guide to MOM4 GFDL Ocean Group Technical Report No. 5, NOAA/Geophysical Fluid Dynamics Laboratory Version prepared on December 23, 2003.
10. P. Kallberg, A. Simmons, S. Uppala and M. Fuentes, The ERA-40 archive. Reading, UK, European Centre for Medium-range Weather Forecasts (ECMWF), ECMWF Re-Analysis Project (ERA), 2004. 31p. ERA-40 Project Report Series, 17.

SOURCE APPORTIONMENT OF THE SIZE-FRACTIONATED URBAN AEROSOLS IN AND AROUND KOLKATA, INDIA

UJJAINI SARKAR*, MONIRUL HAQUE, RAJDEEP ROY
and SANJOY CHAKRABORTY
Department of Chemical Engineering, Jadavpur University
Kolkata, Pin 700032, India
**abhigyan@hotmail.com*

Our main objective was to estimate the heavy metals like the Lead, Mercury, Cadmium, Sodium, Potassium, Calcium, Aluminium, and Iron, in addition to ammonium, chloride, nitrate, and sulphate ions, by Atomic Absorption Spectrophotometry and Ion Chromatography and apportion the most probable sources using the Chemical Mass Balance Model. The three urban locations of Behala Chowrasta, Rabindra Sadan, and Shyam Bazaar Five Points were chosen within the city of Kolkata. One rural location was chosen at the Indian Institute of Technology campus, Kharagpur, a rural site in the Midnapur District of the state of West Bengal, India. The results look quite encouraging.

1. Background

Understanding the sources of atmospheric particulate matter is important because ambient anthropogenic particles have adverse effects on human health, cause visibility degradation, participate in acid deposition, result in material and crop damage and impact global climate change. The increasing concern about PM_{10} and $PM_{2.5}$ has resulted in a considerable number of studies around the world including their mass balance and chemical characterization.

The problem of urban air pollution is worldwide and transcends national boundaries. Major advantages can be obtained both in the understanding of the problem and in attempting to address solutions by taking a regional approach rather than a national approach.

It has therefore become very important to not only measure the levels of fine particles in and around the major cities and industrial areas but to also identify the sources of these particles. In urban areas these fine particles

---

*Corresponding author.

are mostly associated with just a few key sources such as windblown soils, sea spray, biomass burning, motor vehicles, and other combustion processes associated with industry. The size distribution of trace metals is important, since this not only influences the toxicity of a metal when inhaled but also controls the extent to which metals may be dispersed via atmospheric transport and hence is a prerequisite for the determination of rates of deposition of metals to the Earth's surface. In India, such extensive investigations have not yet been undertaken. Data on PM_{10} and $PM_{2.5}$ from our experiments will help link particle species observed at ambient receptor locations to their sources, resulting in a means for developing effective emission control strategies for primary particles and secondary particle precursor species.

Our main objective was to estimate some of the heavy metals such as lead, mercury, cadmium, sodium, potassium, calcium, aluminium, and iron in addition to ammonium, chloride, nitrate, and sulphate ions by Atomic Absorption Spectrophotometry and Ion Chromatography and apportion their most probable sources using the Chemical Mass Balance Model. Three urban locations, namely, Behala Chowrasta, Rabindra Sadan, and Shyam Bazaar Five Points were chosen within the city of Kolkata. One rural location was chosen at the Indian Institute of Technology campus, Kharagpur, a rural site in the Midnapur District of the state of West Bengal, India.

2. Methodology

1. *Sampling*: We sampled atmospheric aerosols from various Urban and Rural locations in and around the city of Kolkata (as shown in Fig. 1), which is one of the major metropolitan cities in the eastern India, using a 5-stage Cascade Impactor (KIMOTO HVS-CPS 105) which automatically fractionated the dust particles into five size fractions and we could go up to the submicron range.
2. *Chemical analysis*: These size-fractionated dusts were then analyzed for several key metals, anions, and cations, using suitable analytical techniques. Atomic Absorption Spectrophotometry was used for estimation involving metals and Ion Chromatography was used for the ions.
3. *Source apportionment*: US-EPA's Chemical Mass Balance Model (CMB-Version 8.0) was used for apportioning the sources. The ambient data as obtained in Step 2 serve as the input to the CMB, along with different source profiles. For this, the various sources are identified and their concentration profiles were generated. The output gave quantitative measurement of the relative contribution of each type of emission source.

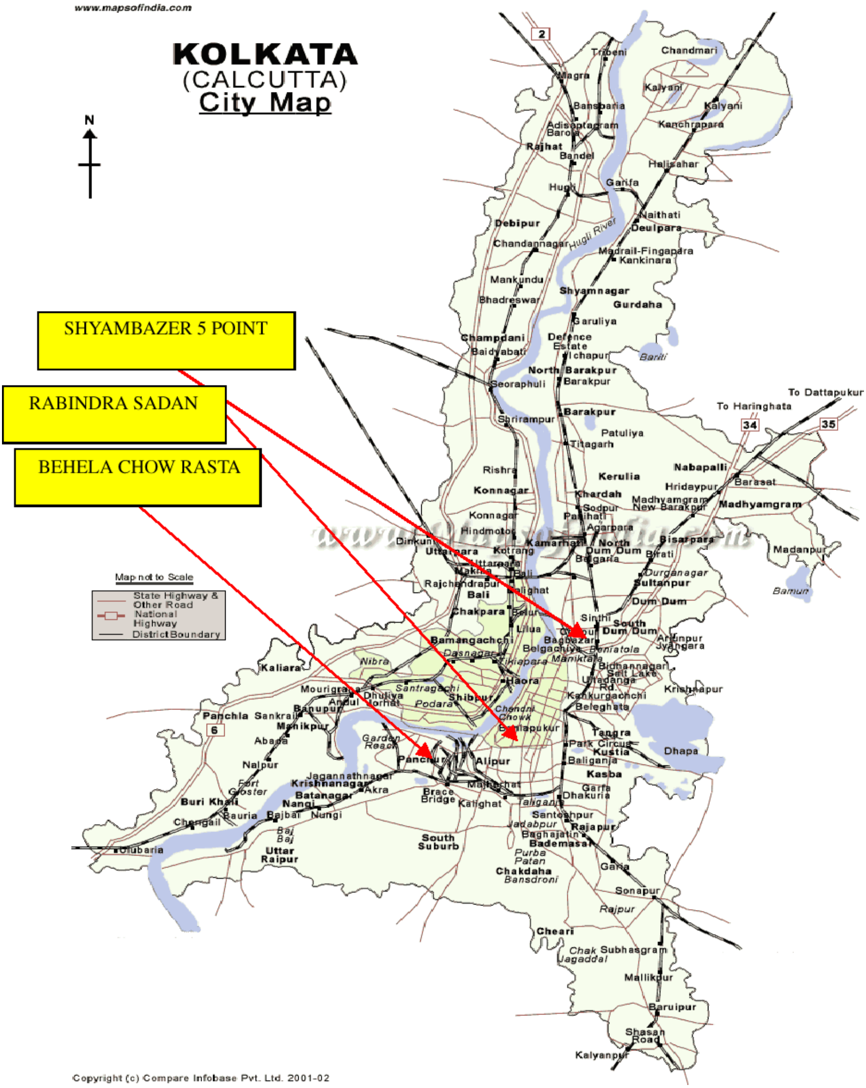

Fig. 1. A Map of Kolkata showing the three experimental sites, namely, Behala Chowrasta, Rabindra Sadan and Shyam Bazar Five Points.

2.1. *Inherent features of the CMB Model*

Receptor modeling is used to provide information regarding source characteristics from the measurements of particle chemical composition in all sampling sites.

The chemical mass balance modeling procedure included the following steps.

1. Identification of the contributing source types.
2. Selection of chemical species that are included.
3. Estimation of the fraction of each of the chemical species which are contained in each source type (i.e., the source composition).
4. Estimation of the uncertainty in both ambient concentrations and source composition.
5. Solution of the chemical mass balance equations.
6. Validation and reconciliation of the results.

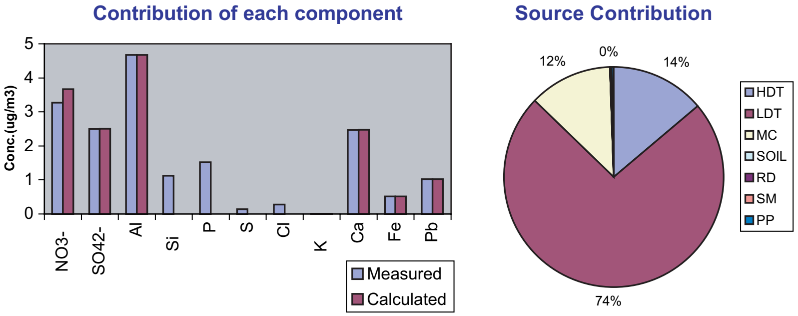

(a) (b)

Fig. 2. Results of a specific run at the Behala Chow Rasta, December' 2004.

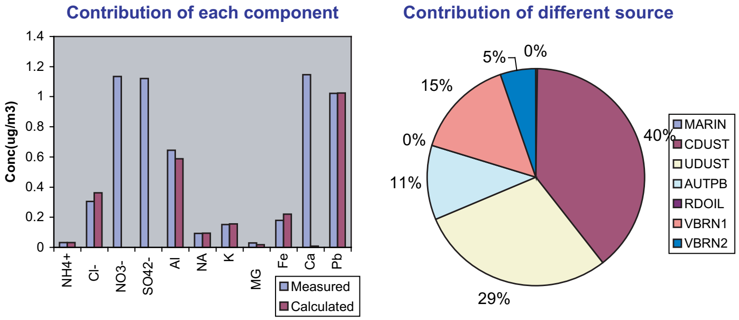

(a) (b)

Fig. 3. Results of a specific run at the Kharagpur, a rural site in the West Bengal, India during daytime, December, 2004.

3. Result and Discussion

Figure 1 shows the locations of the monitoring stations within the city of Kolkata. From the runs done in Behala Chowrasta Figs. 2(a) and (b) are some specific results, we find that the concentrations of the Chloride, Sulphate, Nitrate, Aluminum, Iron, Calcium, and Lead are in the marginal range, which can lead to health hazard. Three sources (HDT, LDT, MC) are the main contributors in this zone. LDT contributes 61% of the total source contribution for fine particles ($< 2.5\,\mu$m) and 74% for coarse (2.5–10.9 μm) particle. Next major source is MC, which contributes 34% of fine particle and 12% for coarse particle. So, the LDT source emission should be controlled in that zone.

Figures 3(a) and (b) show some sample results at the Kharagpur site, during the daytime, for December 2005. Nitrate, Sulphate, Chloride, Lead, Calcium, and Aluminum are most prominent here. Five sources (UDUST, CDUST, VBRN1, VBRN2, AUTPB) are the main contributors during daytime sampling data at this site.

All the sources contribute more or less in the same proportion in both coarse and the fine particle ranges. Among these sources only two, namely, UDUST, and CDUST, contribute approximately 70% for both particle ranges. So precaution is needed to minimize the effect of these sources.

Acknowledgments

We wish to thank the Indian Space Research Organisation (ISRO-GBP) for their kind support to carry out the monitoring at the Kharagpur site and the University Grants Commission, India for funding the entire project.

SPATIAL AND TEMPORAL DISTRIBUTION OF AEROSOL CONCENTRATIONS IN MARCH 2002 OVER ASIA

JAE-IN JEONG*, SOON-UNG PARK, LIM-SEOK CHANG
and EUN-HEE LEE
School of Earth and Environmental Sciences
Seoul National University, Seoul, 151-742, South Korea
**ss99@snu.ac.kr*

The Asian dust aerosol model (ADAM) and the aerosol dynamic model with the MM5 meteorological output on a grid of 60 × 60 km^2 have been used to simulate the temporal and spatial distribution of the Asian dust aerosol and the anthropogenic aerosol concentrations in Asia for the period of March 1–31, 2002. This model is coupled with the gas-phase chemistry of the California Institute of Technology Model and the aqueous-phase chemistry of the Regional Acid Deposition Model with the emission inventory data in the base year of 2000. The results indicate that the ADAM model simulates quite well the spatial and temporal variations of the Asian dust concentration. The spatial distribution of anthropogenic aerosols including sulfate, nitrate and ammonium in Asia show similar distribution patterns to the corresponding emission inventory. It is found that the time–area mean column aerosol mass over Asia is 160 mg/m^2, of which 79 and 21% can be contributed to the Asian dust and other aerosols, respectively. Averaged total nonsoil oriented Asian dust aerosol mass is 35 mg/m^2, of which 23, 24, 16, 11, 5, and 21% contributes to PM$_{10}$ emission, carbonaceous aerosols, sulfate, nitrate, ammonium, and sea salt, respectively.

1. Introduction

Aerosols play important roles in many biogeochemical cycles by providing reaction sites and serving as carriers for many condensed and sorbed species,[1] and also the earth-atmosphere radiative forcing.[2–5] Wind-blown mineral dusts from deserts and semiarid inland areas of the Asian continent have become a distinct feature in East Asia.[6–8] Some of the Asian dust events are reported to transport dust to the western part of USA across the Pacific Ocean.[8,9] During periods of long-range mineral dusts encounter various anthropogenic pollutants that are emitted from various source regions, especially in the eastern part of China, where industrial complexes are concentrated. The nss-SO_4^{2-}can be formed by heterogeneous oxidation reaction on the aerosol surface.[10,11]

Observational data support sulfate and nitrate formation on the mineral aerosols.[12–15] The important mechanism of the aerosol transformation seems to be the aging processes of naturally emitted aerosols in East Asia during long range transport.[16–18] Through the aerosol aging process volatile inorganic compounds such as carbonate or bicarbonate in the dust aerosol in the source region are substituted by particulate sulfate and nitrate, resulting in elevated sulfate and nitrate concentration on the dust aerosols.

Since the Asian dust aerosols have rich trace metal components of Al, Ca, Fe, Na, K, and Mg[16,19] these components have a strong alkaline nature and can act as natural neutralizers of the acid species[20] under certain atmospheric conditions. This process is likely to elevate the levels of sulfate and nitrate on the aerosol.

The purpose of this study is to examine the spatial distributions of Asian Dust and anthropogenic aerosol concentrations over Asia for the period from 1 to 31 March 2002.

2. Model Description

2.1. *Aerosol dynamic model*

An aerosol dynamic model developed by Chang and Park[21] with the gas-phase chemistry of the California Institute of Technology (CIT) model and the aqueous-phase chemistry of the Regional Acid Deposition Model (RADM) together with meteorological output of the MM5 model on a $60 \times 60\,\mathrm{km}^2$ grid has been used to estimate anthropogenic aerosols and gaseous pollutants in Asia for the period March 1–31, 2002 (Fig. 1).

The aerosol dynamic model includes such processes as nucleation, condensation/evaporation, coagulation, sedimentation, hygroscopic growth, dry, and wet deposition processes. The detailed model description is given in Ref. 21.

2.2. *Asian dust aerosol model*

The Asian Dust Aerosol Model (ADAM) developed by Park and In[6] and modified by spectral dust emission flux in the source regions[7] has been used to calculate the temporal and spatial distributions of the Asian Dust concentration in the model domain. The detailed model description is given in Refs. 6 and 7.

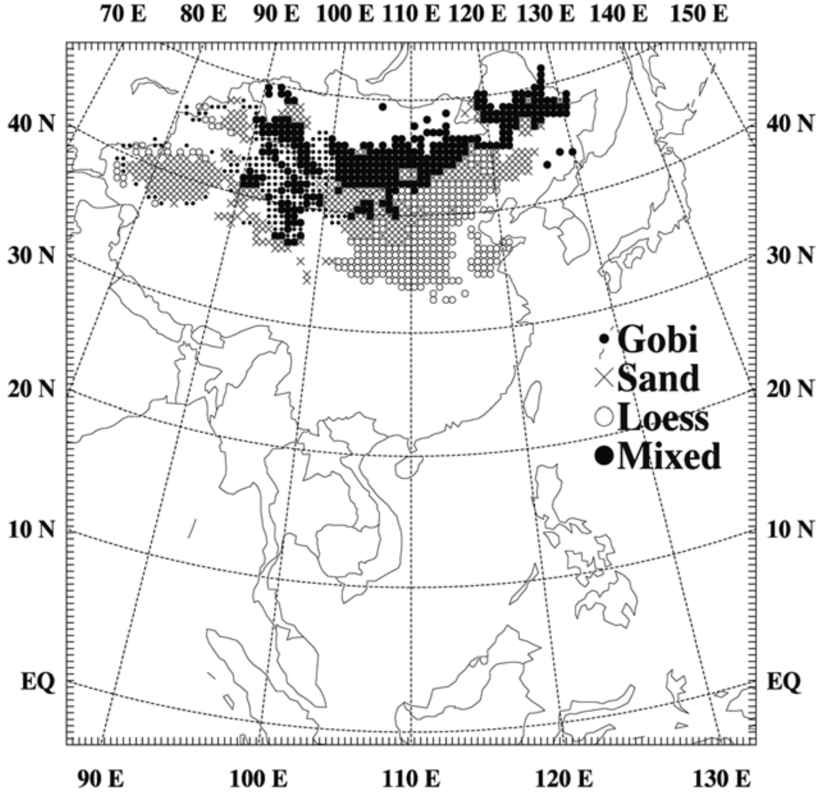

Fig. 1. The model domain with the indication of Asian dust source regions of Gobi (•), Sand (×), Loess (○), and Mixed (●) soil type.

3. Distributions of Anthropogenic Pollutants Emissions

The emission rates of SO_2, NO_x, NH_3, CO, non-methane volatile organic carbon (NMVOC), black carbon (BC), and organic carbon (OC) for the month of March obtained from Ref. 22 are shown in Fig. 2 on a $60 \times 60\,\text{km}^2$ grid. These emission inventories were gathered in the year 2000.

The spatial distribution patterns of SO_2, NO_x and NH_3 (Figs. 2(a), (b) and (e)) emissions are similar with a maximum exceeding 2000 ton/gird/month over eastern China whereas those of PM_{10} and VOC (Figs. 2(c) and (f)) show a maximum over eastern China and the Indo-China peninsula where biomass burnings are the main sources.

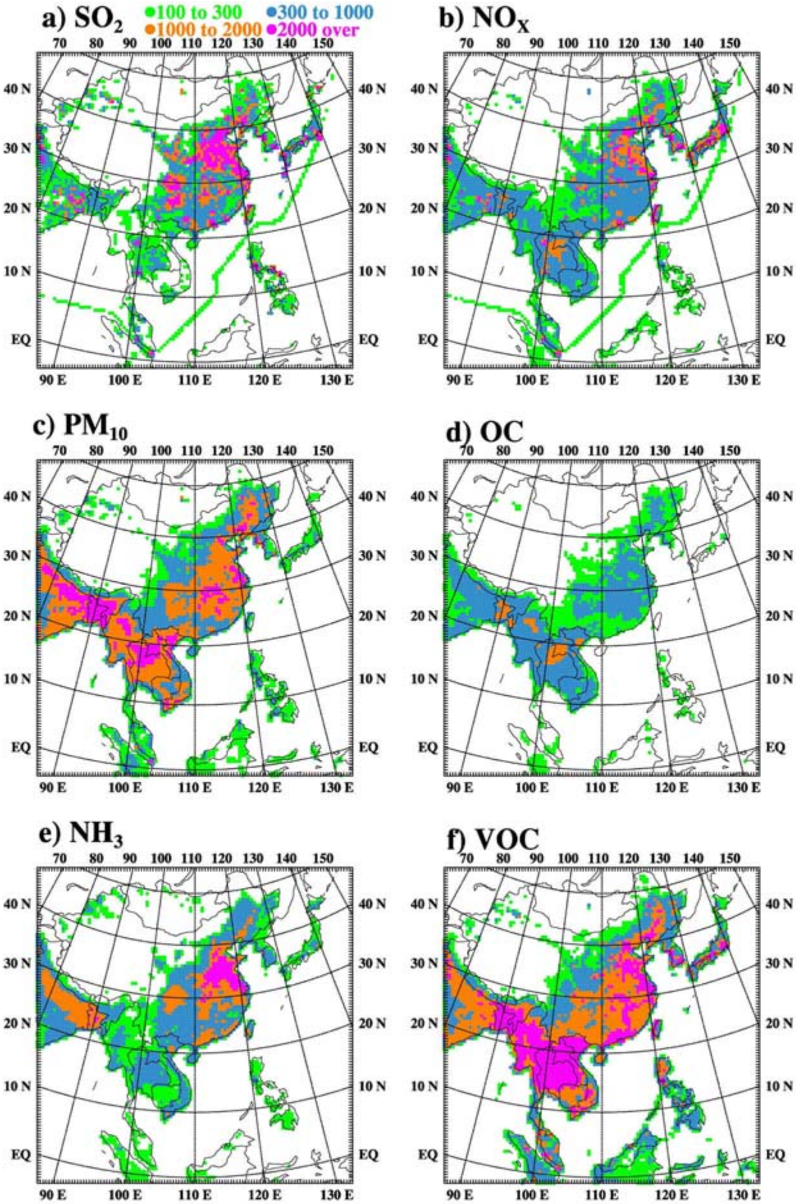

Fig. 2. Spatial distributions of (a) SO_2, (b) NO_x, (c) PM_{10}, (d) OC, (e) NH_3 and (f) VOC emission (ton/gird/month) in a grid $60 \times 60\,\text{km}^2$ over the model domain.

4. Results

4.1. *Temporal variations of observed and modeled gases pollutants and PM_{10} concentrations in Korea*

Figure 3 shows the time variation of the modeled and observed daily mean SO_2, NO_2, O_3, and PM_{10} concentrations averaged over South Korea for the period from 1 to 31 March 2002. The model simulates quite well the temporal variations of observed concentrations. However, the model underestimates the observed NO_2 concentration significantly. This might be mainly due to the underestimation of NO_x emission rate. The simulated SO_2, O_3, and PM_{10} concentration closely matches observations in South Korea. The PM_{10} concentration during the Asian dust period from 19 to 22 March 2002

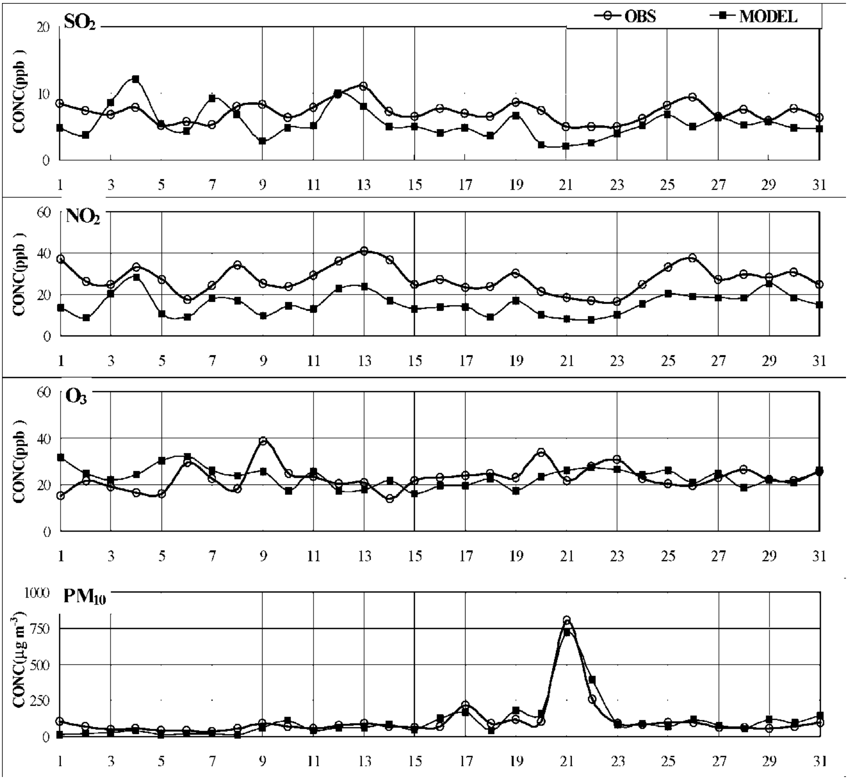

Fig. 3. Time series of daily mean observed (-o-o-) and modeled concentrations of SO_2(ppb), NO_2(ppb), O_3(ppb) and PM_{10} (μg/m^3) (-■■-).

is especially well simulated, implying the usefulness of the ADAM model for the simulation of Asian dust events.

4.2. *Spatial distributions of aerosol concentrations*

The spatial distributions of monthly mean column sulfate, nitrate, ammonium and PM_{10} concentration are shown in Fig. 4. The spatial distribution pattern of monthly mean column sulfate (Fig. 4(a)) is similar to that of the SO_2 emission (Fig. 2) but the maximum concentration zone is slightly further southeast. The spatial distribution pattern of monthly mean column

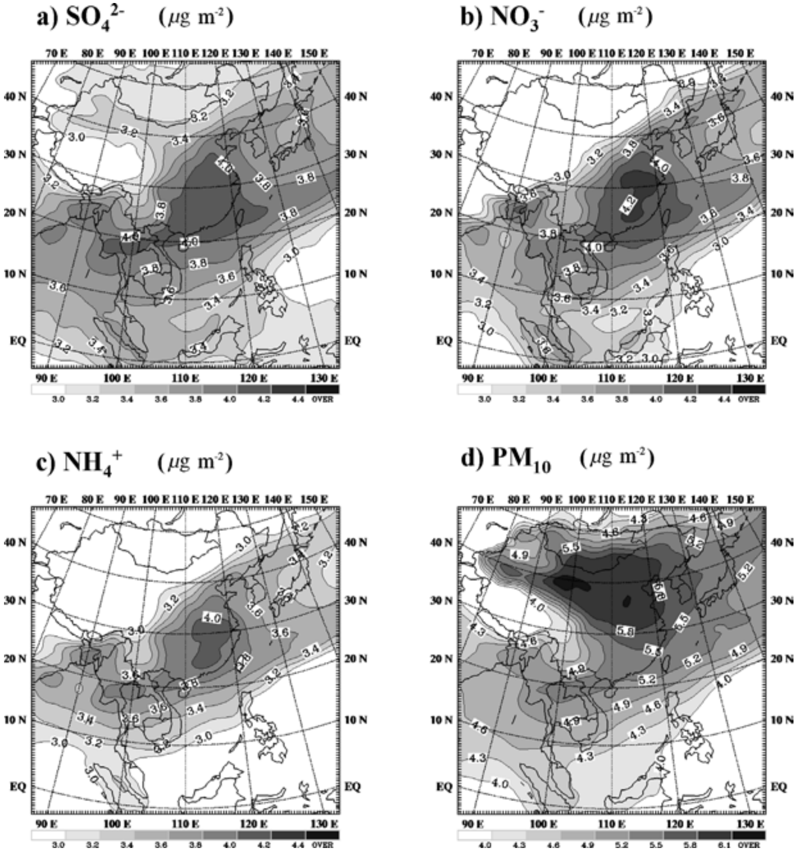

a) SO_4^{2-} (μg m^{-2})

b) NO_3^- (μg m^{-2})

c) NH_4^+ (μg m^{-2})

d) PM_{10} (μg m^{-2})

Fig. 4. Spatial distributions of modeled monthly mean column concentrations of (a) SO_4^{2-}, (b) NO_3^-, (c) NH_4^+, and (d) PM_{10}. The column concentration ($\mu g/m^2$) is expressed in common logarithm.

nitrate concentration (Fig. 4(b)) resembles that of NO_x and VOC emissions (Fig. 2). Nitrogen formation on the aerosol is small and more effective in the regions where both VOC and NO_x emissions are large, indicating the importance of photochemistry. Also, the maximum ammonium concentration (Fig. 4(c)) occurs in southeast China where the maximum ammonia emission occurs (Fig. 2).

The spatial distribution of monthly mean column PM_{10} concentration (Fig. 4(d)) shows that the high PM_{10} concentrations in northern China and Mongolia are mainly due to the Asian dust aerosol whereas those in eastern China and Korea are a mixture of the Asian dust and anthropogenic aerosols.

4.3. *Contribution of each type of aerosol to the total aerosol mass*

The fractional contributions of each type of aerosol to the time–area averaged column integrated total mass of aerosols in the whole analysis period of the whole domain (Fig. 1) are shown in Fig. 5. The time–area mean column aerosol mass is about 160 mg/m^2 of which 79 and 21% contribute to Asian dust and other aerosols, respectively (Fig. 5(a)).

In March 2002 in Asia, several severe dust storms occurred, so that the contribution of Asian dust to the total aerosol mass was much larger than that of the other aerosols. Averaged total nonsoil oriented aerosol mass is 35 mg/m^2, of which 23, 24, 16, 11, 5, and 21% contributed to the PM_{10}

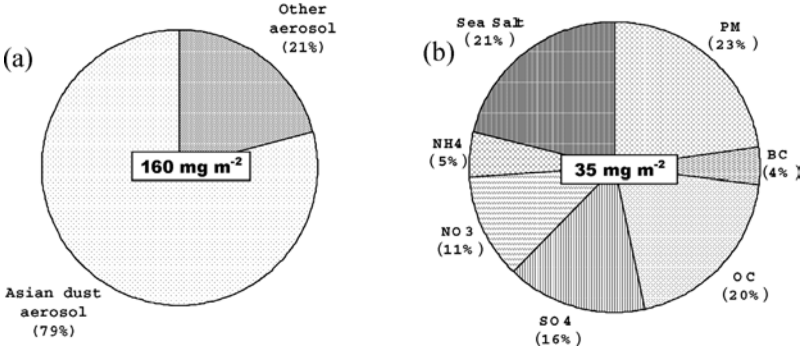

Fig. 5. The fractional contributions of each type of aerosol to the time–area averaged column integrated (a) total aerosol mass and (b) anthropogenic aerosol mass in the whole analysis domain in Fig. 1 for the period from 1 to 31 March 2002.

emission, carbonaceous aerosols (organic carbon + black carbon), sulfate, nitrate, ammonium and sea salt, respectively.

5. Summary

The ADAM and the aerosol dynamic model using MM5 meteorological output on a $60 \times 60\,\text{km}^2$ grid have been used to simulate the temporal and spatial distribution of the Asian dust aerosol and the anthropogenic aerosol concentrations in Asia for the period from 1 to 31 March 2002. During this period severe dust storm events have been reported.

The results indicate that the spatial distribution patterns of monthly mean column anthropogenic aerosol concentrations are quite similar to those of emission rates but the maximum concentration zone is slightly further southeast due to the prevailing wind. The high PM_{10} concentrations in northern China and Mongolia are mainly due to the Asian dust aerosol whereas those in eastern China and Korea are a mixture of Asian dust and anthropogenic aerosols.

The time–area mean column aerosol mass value is about $160\,\text{mg/m}^2$, of which 79 and 21% contribute to Asian dust and anthropogenic aerosols, respectively. Averaged total non-soil oriented aerosol mass is $35\,\text{mg/m}^2$, of which 23, 24, 16, 11, 5, and 21% contribute to the PM_{10} emission, carbonaceous aerosols (organic carbon + black carbon), sulfate, nitrate, ammonium and sea salt, respectively.

Acknowledgments

This research is partially supported by the Climate Environment System Research Center funded by the Korea Science and Engineering Foundation, the Ministry of Education under the Brain Korea 21 Program and the Meteorological and Earthquake R&D Program funded by Korea Meteorological Administration.

References

1. F. J. Dentener, G. R. Carmichael, Y. Zhang, J. Lelieveld and P. J. Crutzen, *J. Geophys. Res.* **101** (1996) 22869.
2. I. Tegen, A. A. Lacis and I. Fung, *Nature* **380** (1996) 419.
3. I. Tegen and I. Fung, *J. Geophys. Res.* **99** (1994) 22897.
4. X. Li, H. Maring, D. Savoie, K. Voss and J. M. Prospero, *Nature* **380** (1996) 416.

5. M. O. Andreae, *Nature* **380** (1996) 389.
6. S.-U. Park and H.-J. In *Atmos. Environ.* **36** (2003) 4877.
7. S.-U. Park and E.-H. Lee, *Atmos. Environ.* **38** (2004) 2155.
8. R. B. Husar, D. M. Tratt, B. A. Schichtel, S. R. Falke, F. Li, D. Jaffe, S. Gasso, T. Gill, N. S. Laulainen, F. Lu, M. C. Reheis, Y. Chun, D. Westphal, B. N. Holben, C. Guymard, I. McKendry, N. Kuring, G. C. Feldman, C. McClain, R. J. Frouin, J. Merrill, D. DuBois, F. Vignola, T. Murayama, S. Nickovic, W. E. Wilson, K. Sassen, N. Sugimoto and W. C. Malm, *J. Geophys. Res.* **106** (2001) 18317.
9. H.-J. In and S.-U. Park, *Atmos. Environ.* **36** (2002) 4173.
10. K. Okada, H. Naruse, T. Tanaka, O. Nemoto, Y. Iwasaka, P.-M. Wu, A. Ono, R. A. Duce, M. Uematsu, J. T. Merrill and K. Arao, *Atmos. Environ.* **24A** (1990) 1369.
11. M. Luria and H. Sievering, *Atmos. Environ.* **25** (1991) 1489.
12. F. Parungo, Y. Kim, C.-J. Zhu, J. Harris, R. Schnell, X.-S. Li, D.-Z. Yang, M.-Y. Zhou, Z. Chen and K. Park, STC Rep. 2906, Natl. Oceanic and Atmos. Admin. Air Resour. Lab, Silver Spring, MD, 1995.
13. S. Horai, I. Minari and Y. Migita, The Annual Report of the Kagoshima Prefectural Insititute, Vol. 9, 1993.
14. Y. C. Gao, D. Zhang and T. Okita, *Shanghai Proceedings Second IUAPPA reg. Conference Air Pollution* **1** (1991) 65.
15. G. R. Carmichael, M.-S. Hong, Ueda, L.-L. Chen, K. Murano, J. K. Park, H. G. Lee, C. Kang and S. G. Shim, *J. Geophys. Res.* **102** (1997) 6047.
16. M. Nishikawa and S. Kanamori, *Anal. Sci.* **7** (1991a) 1127.
17. M. Nishikawa, S. Kanamori, N. Kanomori and T. Mizoguchi, *Sci. Total Environ.* **107** (1991b) 13.
18. M. J. Harkel, *Atmos. Environ.* **31** (1997) 417.
19. S.-U. Park, *Proceedings of Workshop of Asian Dust, March 22, 2002*, Korea Meteorological Administration, Korea, 2002.
20. N. Thongboonchoo and J. Wang, http://www.engineering.uio.wa.eud/~chem_eng/ (1997).
21. L.-S. Chang and S.-U. Park, *Atmos. Environ.* **38** (2004) 4467.
22. D. G. Streets, T. G. Bond, G. R. Carmichael, S. D. Fernandes, Q. Fu, D. He, Z. Klimout, S. M. Nelson, N. Y. Tsai, M. Q. Wang, J.-H. Woo and K. F. Yarber, *J. Geophys. Res.* **108** (2003) (D21), 8809, doi:10.1029/2002JD003093.

AN INVESTIGATION OF WINTER RAINFALL AND SNOWFALL IN THE MOUNTAIN AND COAST

HYO CHOI
Department of Atmospheric Environmental Sciences
Kangnung National University, Kangnung 210-702, Korea
du8392@hanmail.net

The case study of snowfall in the mountainous coastal region of Korea had been undertaken from 09:00 UTC December 6, 2002 through 12:00 UTC December 9, 2002, using 3D-numerical model, MM5 V3.5 with NCEP data inserted as initial input data for the model. During the snowfall period, north-easterly wind and easterly wind in a high-pressure system in north and a low pressure in south of Korean peninsula prevailed in the eastern mountainous coastal region and sensible heat flux induced a great amount of evaporation from the sea surface. This wind could drive the moisture transported from the East Sea-coastal area toward the top of mountain in the west and uplifted moisture should be cooled down and saturated, under westerly cool air masses, resulting in the formation of ice and rain particles inside low cloud. Snowfall band coincided with minimum sensible heat flux band or zero value area, where maximum cooling of air parcels occurred. This snowfall band also directly coincided with the area of relative humidity of 100%. As air temperature at the level of cloud base was below 0°C, water droplet of cloud formed ice crystal phase like snow. As stratocumulus type low clouds moved down toward the ground surface of coastal area, the falling droplets remained snow phase without melting of snow due to the short distance to the ground. Vertical distribution of total cloud mixing ratio, air temperature and relative humidity gave detail information on the height of cloud formation, the determination of snowfall or rainfall of droplets and snowfall area. Under north-westerly wind parallel to the coast, moisture advection became very weak, resulting a small amount snow or no snow in the coast.

1. Introduction

The driving mechanisms on snowfall or winter rainfall are basically similar, but the prediction of snowfall is quite different from one of rainfall. It is generally due to the reason how much cooling is necessary to make for the formation of snowfall. The development of snowball is greatly affected by cooling of water droplets, due to orography in the mountain[1–4] and by enough supplying of moisture through the transfer of moisture evaporated from ocean surface toward the land in the coastal region.[5,6] In the recent years, frequent snowfalls have taken in the mountainous coastal area in Korea. In the coastal sites, we classified three categories such as category 1 — the positions of high pressure system in the north China and low-pressure system in the south sea of Korea, category 2 — the passage of trough in the behind region of high pressure through the eastern coastal sea and category 3 — the couple of a high pressure in north and a low pressure in south with later another high pressure in west and a low pressure in east inducing strong easterly wind from the East Sea.[7,8]

In this study, the case of category 1 was mainly investigated in detail using a three-dimensional (3D) nonhydrostatical numerical model called MM5 model, Version 3.5 and driving mechanism on the formation of snow fall was mainly focused.

2. Numerical Method and Data

A 3D nonhydrostatic grid point model of MM5, Version 3.5 with NECP data in a terrain following coordinate system was adopted for 4 days numerical simulation on meteorological phenomena from 09:00 LST, December 6 to 12:00 LST, December 9, 2002 by PC Pentium 4 with one-way triple nesting at Kangnung National University. There were 22 layers in the vertical spread from 10 m to 10 km with sequentially larger intervals between levels with increasing altitude.

In the numerical process, a triple nesting were made with grid numbers of 125 × 105 with horizontal 27 km interval and vertical grid number of 23 in the coarse domain and in the second domain, grid numbers of 82 × 82 with 9 km interval and in the third domain, grid numbers 61 × 61 with 3 km interval. About 2.50° interval terrain date was used for the largest domain and then the 0.9 km interval data was used for fine mesh domain.

MRF method was adopted for boundary layer process in the planetary boundary layer, and simple ice method for the prediction was also considered. Horizontal and vertical wind and air temperature fields, 3 h accumulated snowfall amount, mixing ratio inside snow, relative humidity, and sensible heat flux were evaluated for understanding snowfall event.

3. Results

3.1. *Beginning stage of snowfall in the coast*

At the beginning stage of snowfall event from 12:00 LST to 18:00 LST, on December 7, a high-pressure system in the north (north-eastern China) and

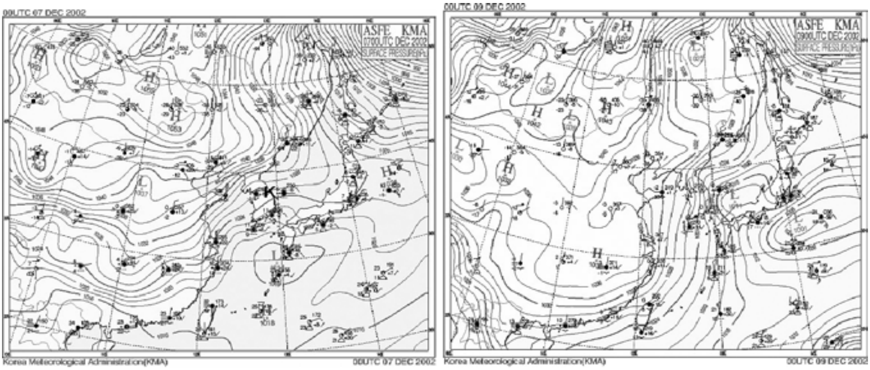

(a) (b)

Fig. 1. (a) Surface weather map near Kangnung city (K) at 09:00 LST December 7 (a high pressure in north and a low in south of Korean peninsula; beginning time of snowfall) and (b) 9, 2002 (a high in west and a low in east; ending time).

a low-pressure system in the south (below Kyusu, Japan) on the weather map in the north eastern Asia influenced the whole Korean peninsula. Under such pressure system, north-easterly wind and easterly wind prevailed near the Kangnung city (here, K) in the eastern mountainous coastal region (Fig. 1).

In Fig. 2, easterly wind near Kangnung city (K) could induce a great amount of moisture from the East Sea toward Kangnung city and then the induced moisture further went to the top of mountain, called Taegulyung of 868 m height (T).[9–11] From vertical profiles of wind, air temperature and relative humidity in Fig. 3, the moisture driven by easterly wind should be cooled down during its uprising toward the mountain top and saturated. The saturated water vapors formed a great stratocumulus cloud near the right-hand side of the mountain top under the influence of westerly wind in the upwind side confronting an easterly upslope wind along the eastern slope of the mountain.

The base of the cloud existed near the eastern top of Mt. Taegulyung at about 600 m and extending to 1.9 km height and spreading toward the sea near the upper level of 1 km at 12:00 LST and 18:00 LST, December 7, 2002. Thus, Gangwon Regional Meteorological Administration (GRMA) located in Kangnung city reported the event of snowfall measured at Taegulyung Meteorological Office near the top of the mountain at 12:00 LST, December 7, and six hours later, at 18:00 LST, Kangnung city in the eastern basin near the coast had snowfall under the extension of 100% relative humidity area over the ground of the city (Fig. 3).

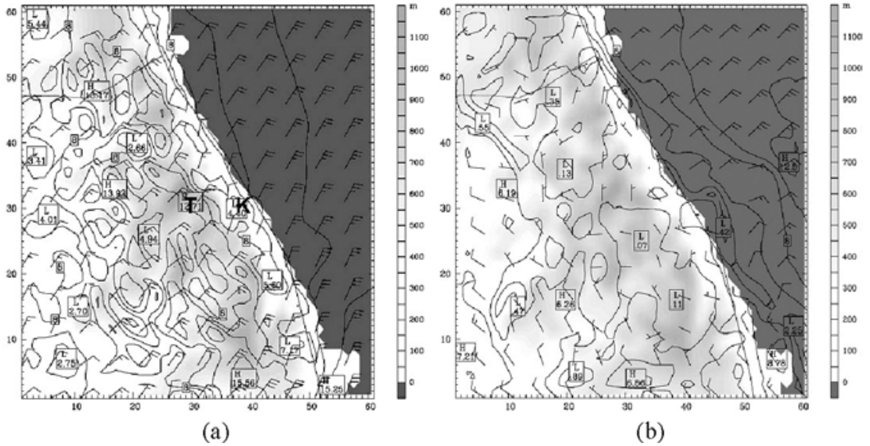

Fig. 2. (a) Surface wind (m/s) in a fine mesh domain at 18:00 LST, December 7, 2002 at the beginning time of snowfall at Kangnung city. (b) 06:00 LST December 9 at the ending time of snowfall. Dark grey area, T and K indicate the East Sea, Mt. Taegulyung and Kangnung city.

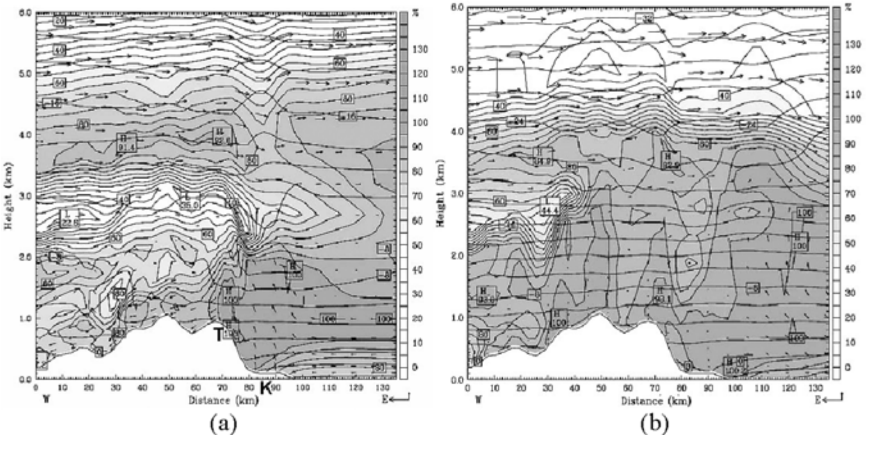

Fig. 3. Vertical profiles of wind (m/s), relative humidity (%) and air temperature (°C) at (a) 18:00 LST, December 7, (b) 18:00 LST, December 8, 2002. T and K denote Mt. Taegulyung and Kangnung city.

As air temperature near the cloud base was below −2°C at 18:00 LST December 7, droplets falling from the cloud base toward the ground of the city should be minute ice crystals and the droplets reaching the ground surface with air temperature of 2°C might be snow without melting of snow due to their short falling distances of about 700 m or rain due to their melting processes or snow mixed with rain like sleet. Kangung city had new snow of 0.1 cm corresponding to rainfall amount of 7 mm. However, GRMA reported Kangnung city had snow instead of rain.

As times went on, easterly wind became stronger and 100% relative humidity area also extended vertically and horizontally, making the cloud to be larger. From the vertical profile of total cloud mixing ratio (g/kg), which represented water content within cloud, the cloud base also became lower and lower and finally it reached less than 50 m height over the ground in Kangnung city, especially around 18:00 LST, December 8. As the base of a great stratocumulus cloud reached the ground surface of the city in Figs. 3 and 4 and air temperature near the ground was 0°C, droplets falling from the cloud toward the ground should be snow without melting of snow. From 06:00 LST through 18:00 LST, the city had continuously new snows with a maximum amount of 3.4 cm and an accumulated amount of snow was 9.2 cm.

Generally speaking, the area of 100% relative humidity over the ground surface from the vertical profiles of wind, relative humidity and air temperature in Fig. 3 coincided with the area of cloud formation in showing total cloud mixing ratio in Fig. 4. As the cloud base was below 0°C, the droplets in cloud were ice crystals. However, the possibility of droplets falling down to the ground to be snow should depend upon no melting of droplets composed of ice crystals under a short distance to the ground surface.

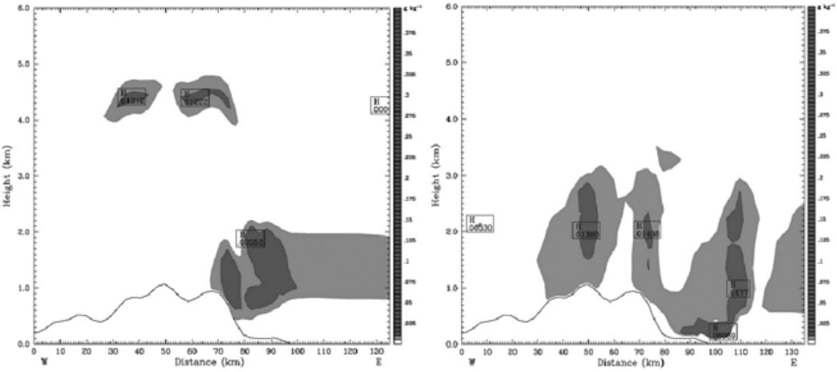

(a) (b)

Fig. 4. As sown in Fig. 3, except for total cloud mixing ratio (g/kg).

If cloud droplets fall down toward the ground with air temperature greater than 0°C like 3°C at 18:00 LST December 8, they become rain. As the cloud droplets of ice phase close to the ground surface of the city, the phase of snow was changed into the phase of rain, through melting process of ice crystal to be water due to air temperature over than 0°C. However, when the distance between the cloud base and the ground is very close, snow phase of droplets still remains snow phase, but when the distance is far, snow phase is changed into rain phase.

A relative humidity band of 100% near the ground surface lay along the coast from south-east to north-west and coincided with rainfall amount band along the coast (Figs. 5 and 6). Simultaneously, these two kinds of bands also coincided with minimum values of sensible heat fluxes near the surface (Fig. 7).

In the open sea, sensible heat flux was very big with a maximum value of 320 W/m^2, which implied a great amount of water vapor to be evaporated from the sea surface into the atmosphere, due to the temperature difference between sea water (about 8°C) and air temperature (about 2–3°C) near the sea surface. The sensible heat fluxes became smaller closing to the coast. In the coastal inland, the fluxes were zero or negative value, due to very small temperature difference between air temperature and ground surface temperature, implying the cooling of air masses by the cold ground surface.

Thus a great amount of moisture driven by easterly wind from the sea into the inland basin and further the mountain side should be cooled down

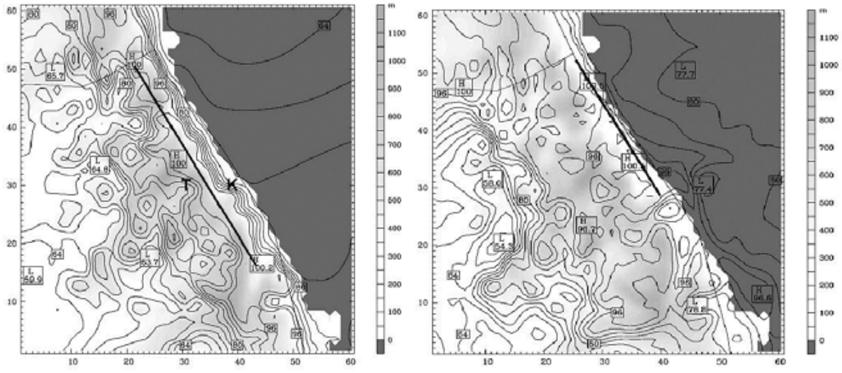

(a) (b)

Fig. 5. (a) Relative humidity (%) at 10 m height over the ground surface at 18:00 LST, December 7, 2002 and (b) 18:00 LST, December 8. T and K denote Mt. Taegulyung and Kangnung city.

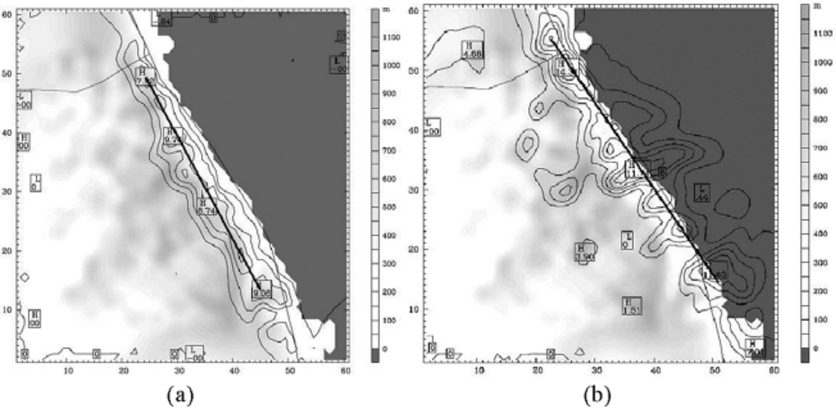

Fig. 6. As shown in Fig. 5, except for rainfall amount (mm) (a) at 18:00 LST, December 7, 2002 and (b) 18:00 LST, December 8.

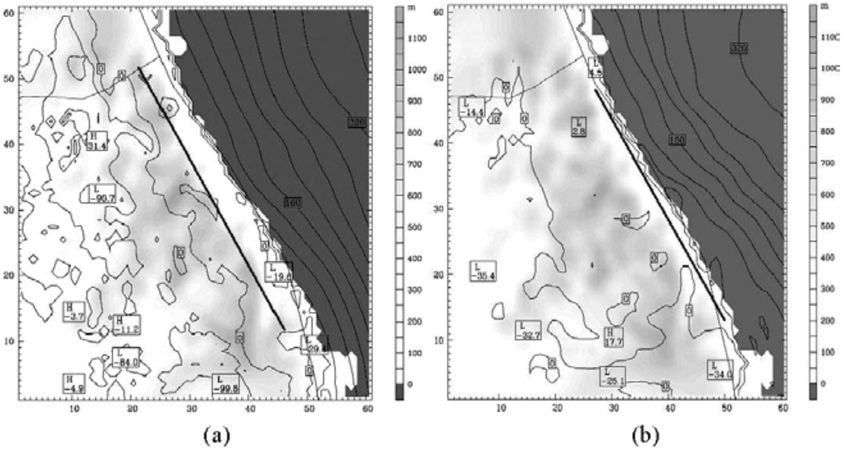

Fig. 7. As shown in Fig. 5, except for (a) sensible heat flux (W/m^2) at 18:00 LST, December 7, 2002 and (b) 18:00 LST, December 8.

by cold ground surface and adiabatic cooling processes during their uprising toward the mountain top, showing the saturation of transported moisture. The saturated moisture formed a great low cloud like stratocumulus on the mountain top and the cloud was observed in the right hand side of the mountain top under westerly wind in the upwind side of the mountain.

3.2. *Ending stage of snowfall in the coast*

After 18:00 LST, December 8, snowfall band (or rainfall band) moved from the coastal inland toward the coastal sea, as time went on. As north-easterly wind prevailed during the snowfall period was gradually changed into northerly or north-westerly before 09:00 LST, December 9, onshore wind was confined to the only coast and became weak under the westerly wind from the upwind side of the mountain toward the coast, resulting in the movement of snowfall band into the coast (Fig. 8).

Similar to the case of snowfall, snowfall band directly coincided with the area of relative humidity of 100% and simultaneously, the area of minimum sensible heat flux. Under the northerly and north-westerly winds, moisture advection from the sea into the inland became weaker and weaker, inducing the formation of a small amount of clouds or no cloud in the inland basin like Kangnung city.

From 09:00 LST, December 9, north-westerly wind parallel to the coastal line could not induce sufficient amount of moisture advection from the sea into the inland basin and further the top of the mountain, resulting in the formation of small amounts of clouds in the coast (or no cloud) and sequentially, no snowfall occurred in the city (Fig. 9).

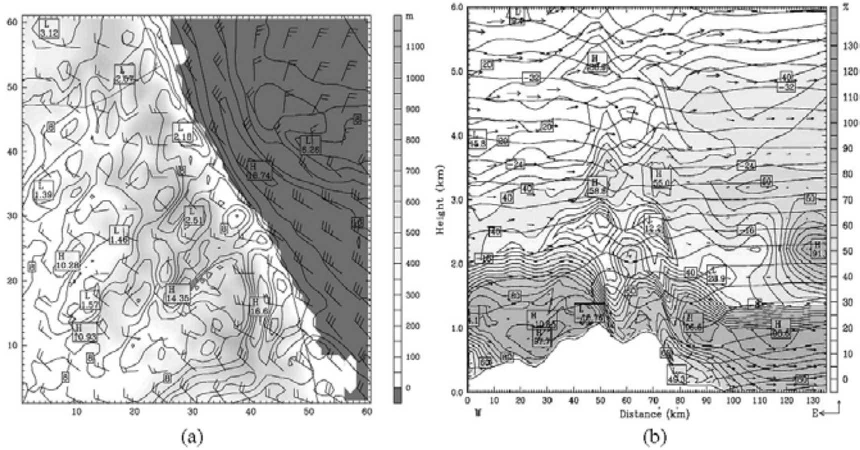

(a) (b)

Fig. 8. (a) Surface wind (m/s) at 10 m height over the ground surface at 06:00 LST December 9 near the ending time of snowfall. (b) Vertical profiles of wind (m/s), relative humidity (%) and air temperature (°C).

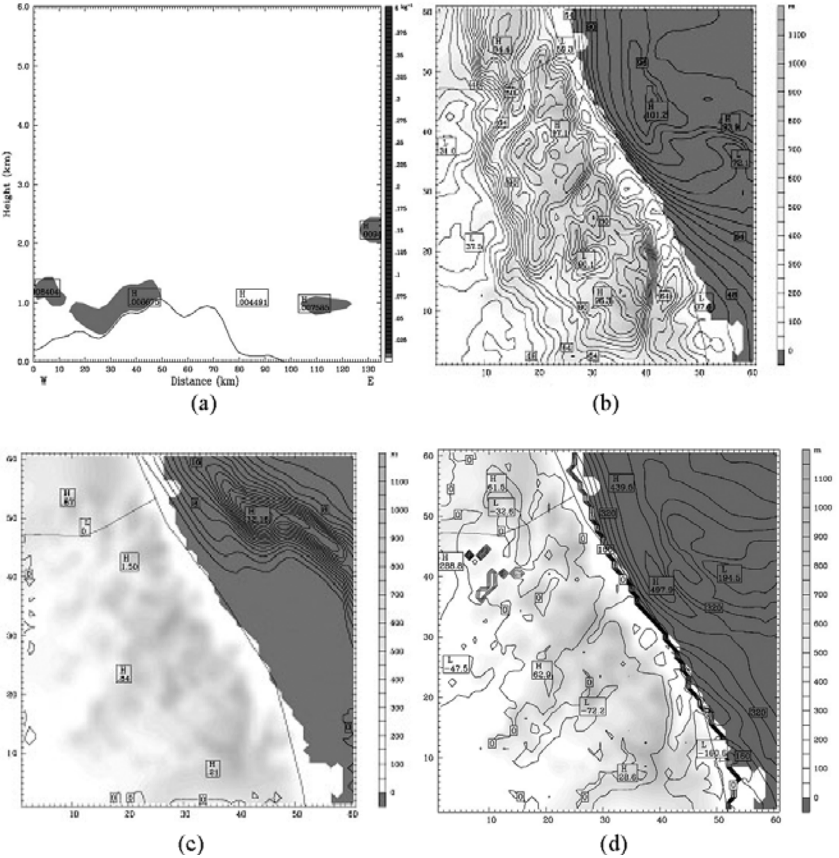

Fig. 9. (a) Vertical profiles of total cloud mixing ratio (g/kg). (b) relative humidity (%), (c) rainfall amount (mm) and (d) sensible heat flux (W/m^2) at 10 m height over the ground surface, respectively.

Even if north-westerly wind coming from northern China made air parcels be cooled down, generally air parcels with a small amount of moisture in winter could not be saturated, resulting in no existence of snowfall in the coastal region.

3.3. *Comparison of precipitation and snowfall*

Through 78 h numerical simulation with NCEP data sets, numerical simulation results of winter rainfall amounts were compared with precipitation and

Table 1. Comparison of calculated precipitation (mm) to observed ones at Kangnung city from December 7–9, 2002. ( ) denotes snowfall amount.

Date	Comparison	12:00	18:00	00:00	06:00	12:00	18:00	00:00	06:00
12/07	Observed	6.6	7.0	3.0	3.5	6.5	4.0	1.2	4.6
to	(snow amount)	(0.0)	(0.1)	(0.2)	(2.8)	(3.4)	(0.1)	(0.2)	(8.6)
12/08	Calculated	4.5	7.0	2.0	2.0	6.5	8.0	1.0	0.0

snowfall amounts measured at Gangwon Regional Meteorological Administration located in Kangnung city. The general tendency of calculated rainfall amounts well matched with observed ones, except for two cases. As at 18:00 LST, December 8, the cloud base very closed to the ground surface of the city, ice droplets falling toward the ground became rain droplets at air temperature of 3°C, through melting process of ice crystal to be water. Thus the reason why observed snowfall amount was too small with 0.1 cm might be attributed to melting of snow into rain, and result in calculated precipitation amount to be twice greater than observed one (Table 1).

When both calculated and observed wind directions at 06:00 LST, December 9 was north-westerly (340°) parallel to the coast and this wind did not induce sufficient moisture advection from the sea into the coast to make a great cloud, showing calculated value of precipitation to be zero and resulting in a great discrepancy to observed one. Probably, this discrepancy might be due to the exaggeration or reduction of moisture modification by the model, under unknown local effect or by a couple hours faster movement of calculated snowfall band (or rainfall band) by the model toward the coast than the observed one. Even if partial discrepancy between calculated and observed ones still existed, the general tendency of calculated rainfall amount well matched with observed one.

4. Conclusions

During the snowfall period, north-easterly wind and easterly wind under the existence of a high pressure system in north and a low pressure in south of Korean peninsula prevailed in the eastern mountainous coastal region and sensible heat flux induced a great amount of evaporation from the sea surface into the lower atmosphere. Then north-easterly could induce a great amount of moisture from the sea toward the top of mountain in the west. The uplifted moisture should be cooled down and saturated, resulting in the formation of ice and rain particles inside low cloud and sequentially a great cloud, resulting in falling of snow from the cloud base. Snowfall band (or rainfall band) near the surface coincided with the area of minimum sensible heat flux and it directly coincided with the area of relative humidity of 100%. Under air temperature below 0°C near cloud base, water droplets falling from stratocumulus type low cloud could form ice crystal phase like snow.

However, as the low cloud moved down toward the ground surface of coastal area in the east, snow phase of falling droplet was changed into rain phase of droplet under higher air temperature over than 0°C. If the distance from the cloud base to the ground was too close, the droplet still remained snow phase, showing snowfall in the coastal basin. As north-easterly wind was gradually changed into northerly or north-westerly in the coastal sea near the ending stage of snowfall and onshore wind was confined to the only coast and the moisture advection from the coastal sea into the inland became weaker, resulting in the movement of snowfall band into the coastal sea and finally no snowfall in the coastal inland basin like a coastal city.

Acknowledgments

The author thanks Korean Meteorological Administration for the research on "Gangwon region heavy snowfall prediction skill development of 2002–2005".

References

1. B. A. Colle, J. B. Wolfe, W. J. Steenburgh, D. E. Kingsmill, J. A. W. Cox and J. C. Shafer, *Mon. Wea. Rev.* **133** (2005) 2947.
2. C. N. James and R. A. Houze, *Mon. Wea. Rev.* **133** (2005) 3110.
3. K. Kim, K. Ha and H. Um, *J. Korean Meteor. Soc.* **39** (2003) 151.
4. M. Wetzel, M. Meyers, R. Borys, R. McAnelly, W. Cotton, A. Rossi, P. Frisbie, D. Nadler, D. Lowenthal, W. Brown and S. Cohn, *Wea. Forecasting* **19** (2004) 806.
5. K. Heo, K. Ha and S. Shin, *J. Korean Meteor. Soc.* **41** (2005) 547.
6. J. S. Waldstreicher, *Bull. Amer. Soc.* **33** (2002) 19.
7. E. Shon and M. Ahn, *Proc. Korean Meteor. Soc.* (2004) 154.
8. Y. Lee and L. Mahrt, *Proc. Korean Meteor. Soc.* (2004) 172.
9. A. Bamzai and J. Shukla, *J. Climate* **12** (1999) 3117.
10. H. Choi, *Meteor. & Atmos. Phys.* **87** (2004) 93.
11. H. Choi, Y. Zhang and Takahashi, *Meteor. & Atmos. Phys.* **87** (2004) 109.

IMPACT OF REGIONAL CIRCULATION AND HEAT BUDGET TO TROPICAL NIGHT

HYO CHOI and DOO SUN CHOI*
Dept. of Atmospheric Environmental Sciences
Kangnung National University
Kangnung, 210-702, Korea
**du8392@hanmail.net*

Unusual nocturnal high air temperature over than 25° C called tropical night in the mountainous coastal region was investigated by a three-dimensional non-hydrostatic model from 09:00 LST, August 13 to 09:00 LST, August 15, 1995. As synoptic westerly blowing over the mountain in the west is interrupted by upslope wind combined with valley wind and easterly sea breeze from the eastern sea, two different wind regimes go up to the 1700 m height, becoming a westerly return flow over the sea. Convective boundary layer (CBL) of about 1 km and thermal internal boundary layer less than 150 m are developed over the mountain basin and along the mountain slope from the coast. As sensible heat flux convergences between the ground surface of the mountain or inland coast and upper level atmosphere over the surface are much greater than the flux on the coastal sea, the flux should be accumulated inside thermal internal boundary layer along the mountain slope and the CBL over the mountain. Then, accumulated sensible heat flux under the influence of sea-valley wind from the sea to the top of mountain and from the mountain top toward the coastal surface should be transported into the coast, resulting in high air temperatures in the coastal inland and sea. After sunset, synoptic westerly wind was associated with mountain wind and land breeze and was further stronger. Very small flux divergence occurs in the coast, while flux divergences are much greater at both the mountain top and along its eastern slope than over the coastal inland and sea surfaces. By more cooling down of the mountain surface than the coastal surface and heat transfer from warm pool over the coast into the coastal surface, nocturnal air temperatures on the sea and coastal inland surfaces are not much changed from daytime ones, resulting in the formation of nocturnal high temperature.

1. Introduction

During the past decade, empirical and numerical studies on wind and heat budget over coastal complex terrain have been carried out for precise prediction, but their inaccurate predictions are due to complicate driving mechanisms of heat and moisture budgets. Arya[1] and Raynor *et al.*[2] explained direct association of heat process in the coastal region with wind and temperature generated by sea-land breeze. Pielke,[3] Choi[4,5] and Palmer *et al.*[6] stated both orographic effects with high mountains and the roll of sea breeze on atmospheric circulations near the coast, under the horizontal temperature contrast of air over land and sea surfaces. Kondo *et al.*[7] emphasized that more sensible heat had to be accumulated in the valley region than over the mountainous areas on calm and cloudless days, due to much larger amplitudes of the diurnal variations of atmospheric temperature and surface pressure at the bottom of a valley.

Whiteman[8] and Holton[9] explained thermally developed wind system in mountainous terrain through observation and Kuwagata *et al.*[10] discussed the daytime boundary layer heating process over complex terrain under fair weather. Baik *et al.*[11] also investigated dry and moist convection forced by an urban heat island, but they are confined to explain the accumulation of heat in the inland basin, not consider thermal accumulation in the mountainous coastal region. Choi and Kim[12] verified the formation of nocturnal thermal high in inland basin near Taegu city, Korea by numerical simulation on thermally induced circulation. This study is focused on the diurnal variation of sensible heat flux in the mountainous coastal sea, using a three-dimensional numerical model, which can greatly influence upon sea and air temperature distribution over the coastal sea under the effects of steep high mountains and coastal inland.

2. Numerical Analysis and Data

Topographical feature of the study area consists of inland plain, high steep mountains, narrow inland basin and sea. In a coarse-mesh domain, Tae Bak mountains lie from south toward north along the eastern coast of Korea and another several branch mountains stretch out toward south-west off the mountains. In a fine-mesh domain, the study area consists of complex terrains characterized by forest in a high steep mountain (Mt. Taeguallyung; 865 m) in the west, Kangnung city in the narrow plain of the center and sea in the east.

A nonhydrostatic grid point model in a complex terrain-following coordinate (x, y, z^*) was adopted for a 48 h numerical experiment from 06:00 LST (Local Standard Time = 9 h + UTC), August 13 to 06:00 LST, August 15, 1995, by Hitachi super computer at Japan Meteorological Research Institute (JMRI).[13,14] Two different domains consist of 50×50 grid points with a uniform horizontal interval as 20 km in a coarse-mesh model and 5 km in a fine-mesh for one-way double nesting, respectively. Sixteen levels in the vertical co-ordinate were divided from 10 m into 6 km. Twelve hourly global meteorological analysis data (G-ANAL) made by Japan Meteorological Agency were horizontally and vertically interpolated for initial data in the coarse domain and predicted ones by the model were treated as lateral boundary data in the fine-mesh. National Oceanic and Atmospheric Administration satellite pictures were used as sea surface temperature in two models.

3. Result and Discussion

3.1. *Wind and air temperature distribution-day*

At 12:00 LST, August 14, in a coarse-mesh domain, synoptic-scale westerly winds at 10 m height over the ground surface prevail over the Yellow Sea and penetrate into the Korean peninsula and pass through the eastern coastal mountainous regions near Kangnung city. The city was under south-westerly wind in the inland, but easterly sea breeze was also detected in both the coastal inland and sea, due to the temperature contrast of air temperature between over land and sea surfaces. So, two different wind regimes confront each other in the inland 15 km away from the coast and the intrusion of sea breeze from sea toward inland near is limited to inland 15 km near Kangnung city or 20 km in the low latitude (Figs. 1(a)–(c)).

Winds at the city with a high steep Mt. Taeguallyung in the west of the city and the East Sea in the east are still south-westerly. Though wind and temperature in the coarse and fine-mesh domains are similar to observed data, simulations in a fine domain by one-way nesting process produce more accurate values with the same patterns. In Fig. 1(d), turbulent heat in terms of vertical diffusion coefficients for turbulent heat (K_h) can easily present vertical motion of air due to daytime heat process. The values of K_h are more than 120 m^2/s over the plain in the west of the mountain and the top or along the eastern slope of the mountain, but 5 m^2/s over the sea surface.

Higher values of the diffusion coefficients are found along the eastern slope than over the sea, due to great diabatic heating on the mountain surface. In the layer above the height of 1700 m, turbulent heat diffusivity is almost constant and the development of convective boundary layer (CBL) is confined to this level. So, the CBL is developed with a depth of about 1 km over the ground in the upwind side of the mountain, while its depth is only limited to less than 150 m along the eastern slope as thermal internal boundary layer (TIBL) parallel to sea breeze front. The depth of TIBL in

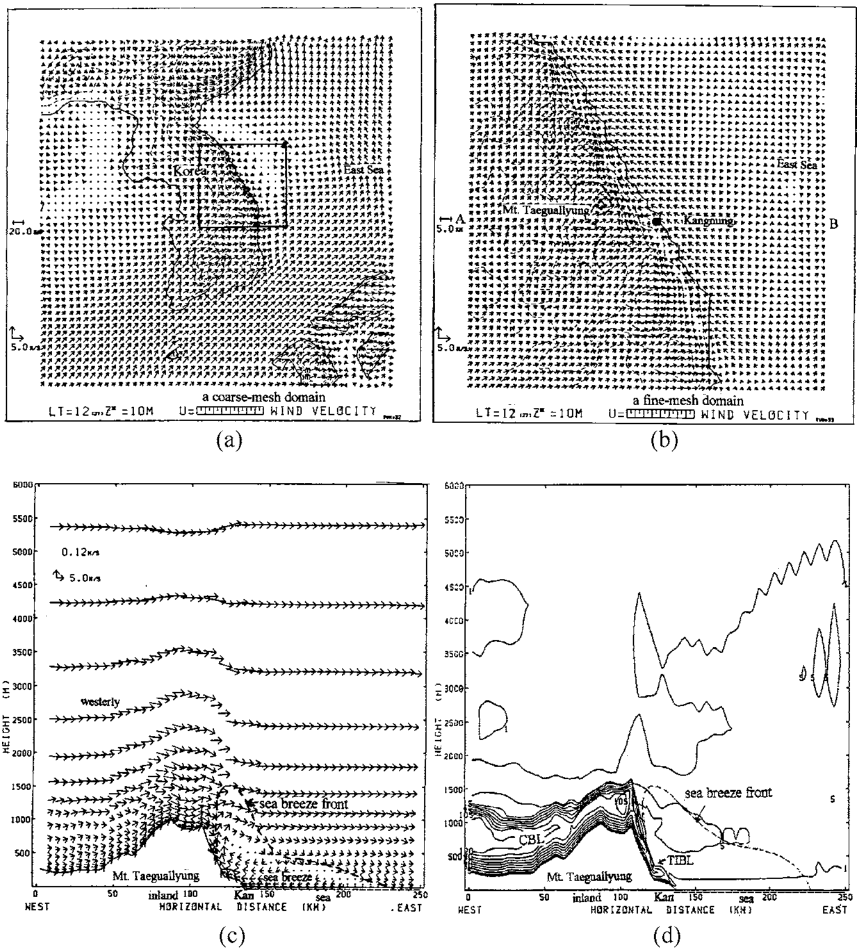

Fig. 1. (a) Wind (m/s) in a coarse-mesh domain at 12:00 LST, August 14, 1995. Thin dash line and box denote topography and (b) a fine-mesh domain near Kangnung city. (c) Vertical distribution of wind (m/s) in a fine-mesh domain near Kangnung city. Kan denotes Kangnung city. (d) Vertical diffusion coefficient for turbulent heat (m^2/s).

the inland coast is 250 m and becomes shallow along the slope. Warm and dry air is the inside of TIBL or CBL, while relatively cool and moist air is in the sea breeze front. The formation of shallow TIBL like CBL from the coastal edge along the eastern slope of the mountain is due to the shrunken of CBL cooled down by relatively cool easterly sea breeze and partly due to different surface roughness between land and sea surfaces.

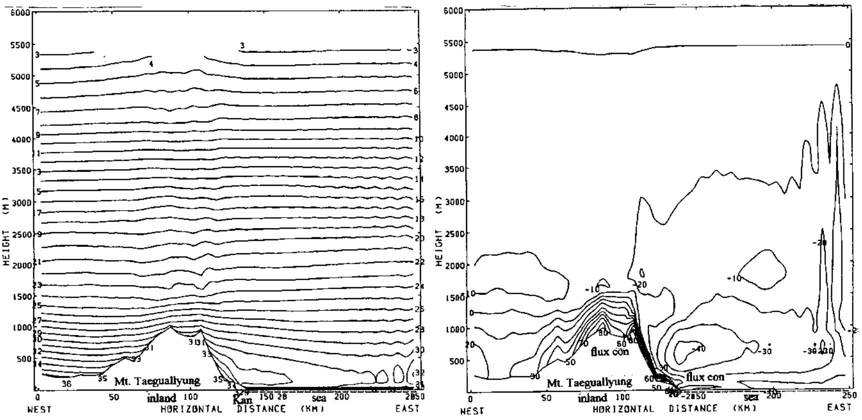

(a) (b)

Fig. 2. (a) As shown in Fig. 1(c), except for air temperature (°C) and sensible heat flux (W/m^2).

In Fig. 2(a), maximum air temperature is found near the bottom of the eastern slope, because strong daytime thermal heating at the ground surface on the mountain slope can produce a very high air temperature and westerly downslope wind may make, in part, a contribution to the increase of air temperature due to adiabatic heating processing from compression of air by wind, which exact amount of adiabatic heating rate has not presently been known in literatures.

In Fig. 2(b), sensible heat fluxes from the surface of the mountain top to the upper level are in a range of 60 to $-20\,\mathrm{W/m^2}$ and those from the inland coast to the upper level are also from 50 to $-40\,\mathrm{W/m^2}$, showing flux convergence. On the other hand, the fluxes from the coastal and open sea surfaces to the upper levels are from -20 to $-40\,\mathrm{W/m^2}$ and from -10 to $-40\,\mathrm{W/m^2}$. As sensible heat fluxes are much greater at both the top of the mountain and inland coast than in the upper level or slightly greater at the sea surface, flux convergences toward the upper level could cause these surfaces to be warmed up. Since sensible heat flux convergence at the mountain top is stronger than over the coastal sea, accumulated sensible heat flux should be transported into the coast and results in maximum air temperature just on the coastal inland surface, especially at the point of maximum sensible heat flux convergence. The transportation of accumulated sensible heat flux follows the return flow in the upper level over the coastal sea, which has two atmospheric circulations, such as small circulation in the coastal sea and big one in the open sea.

Compare to surface heating of basin surrounded by only mountains, the transportation of accumulated sensible heat flux from the mountain toward the low atmosphere over the sea cannot cause sea waters to be much warmed up, but it can greatly warm up air and soil. Because one thousand times higher energy is required to warm up sea water masses than air masses. At this time, air temperature near ground surface of Kangnung city was 35°C, which well matches calculated value, but air temperature on the sea surface is 28°C less 7°C than one in the inland coast.

3.2. *Wind and air temperature distribution — night*

At 00:00 LST, August 15, as nighttime radiative cooling of the ground surface due to no solar radiation increases, synoptic south-westerly wind over the top of Mt. Taeguallyung moves down along the eastern slope toward the coast and is associated with mountain wind generated by air temperature difference between the mountain and the plain surfaces, resulting in downslope wind. Then, the downslope wind is further intensified by land breeze due to horizontal air temperature difference between the coastal inland and the sea surfaces, becoming strong downslope wind storm (Figs. 3(a)–(c)).

As the downslope wind storm reaching the bottom of the eastern slope is too strong, a hydraulic jump motion of air occurs near the ground surface of Kangnung downtown, bounding up to the 1 km height over the coastal sea and causes the generation of lee-side internal gravity waves. Maximum speed of wind storm on the lee slope of the mountain reaches 15 m/s, but nighttime surface wind speed of 2 m/s near Kangnung city beneath of the internal gravity waves is much weaker than daytime one of 5 m/s, under the sea breeze.

Turbulent diffusion coefficients for heat of 1 m^2/s exists near the ground surface and indicates occurrence of a thin shallow nocturnal surface inversion layer (NSIL). Although its thickness is within the height of about 150 m over the ground in the west of the mountain, no inversion layer due to the destruction of the inversion by strong downslope windstorm is found along the eastern slope and shallow surface inversion layer exists in the coast (Fig. 3(d)). Over the sea surface, marine inversion layer (MIL) forms with a thickness of about 250 m.

The thickness of the marine inversion layer is slightly larger than one of the inland NSIL, because the cooling of sea surface is much smaller than that of the ground surface. At 00:00 LST, surface air temperature at Kangnung city is 29°C, which is over than 25°C and this temperature continues to be until next day morning. If air temperature over 25°C persists for

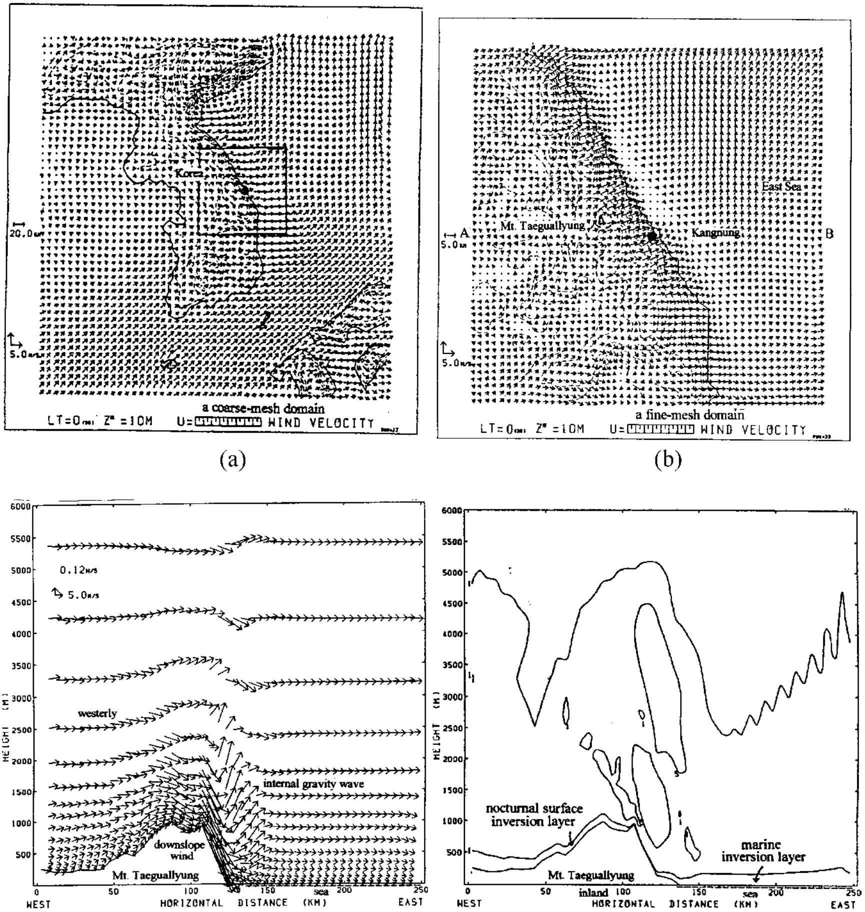

(a) (b)

(c) (d)

Fig. 3. (a) Wind (m/s) in a coarse-mesh domain at 00:00 LST, August 15, 1995. Thin dash line and box denote topography and (b) a fine-mesh domain near Kangnung city. (c) Vertical distribution of wind (m/s) in a fine-mesh domain near Kangnung city. Kan denotes Kangnung city. (d) Vertical diffusion coefficient for turbulent heat (m^2/s).

whole night, it is called tropical night in the northeastern Asian countries (Fig. 4(a)).

Sensible heat fluxes at the surface of the mountain top and in lower atmosphere with -70 and $-10\,W/m^2$ produce sensible heat flux divergence, indicating heat loss at the ground surface and cooling of ground surface (Fig. 4(b)). Sensible heat fluxes of $-140\,W/m^2$ on the eastern slope to $-10\,W/m^2$ in the lower atmosphere also produces a great sensible heat flux divergence along the slope, resulting in great change of air temperature

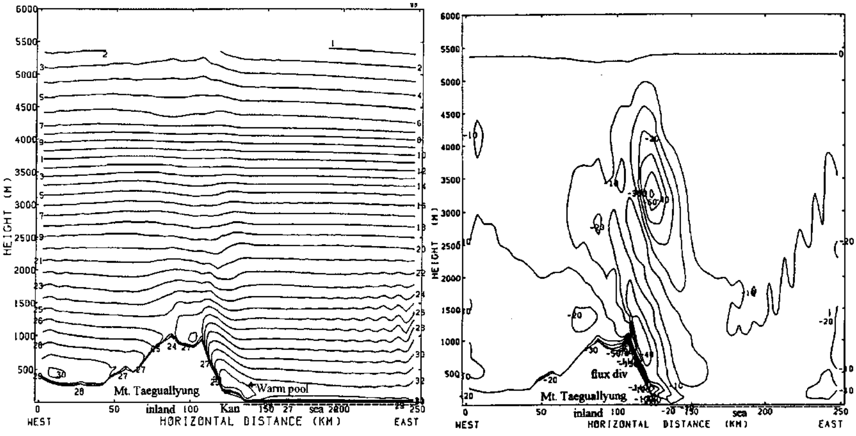

(a) (b)

Fig. 4. (a) As shown in Fig. 3(c), except for air temperature (°C) and sensible heat flux (W/m^2).

in the narrow atmospheric boundary layer along the slope, as shown in Fig. 4(a). On the other hand, sensible heat fluxes at the inland coastal surface (or coastal sea) and in the lower atmosphere are just $-20\,\mathrm{W/m^2}$ (or $-10\,\mathrm{W/m^2}$) and $-20\,\mathrm{W/m^2}$ (or $-10\,\mathrm{W/m^2}$), very small sensible heat flux divergence (or no flux divergence) occurs in the coastal area.

So, sensible heat flux divergence is much greater at the top of mountain and along the eastern slope than at the coastal inland surface near Kangnung city and the sea surface. It appears that the mountain surface more cools down than the coastal inland surface and the sea surface, and the nighttime air temperatures near the coastal inland and sea surfaces are not much changed from daytime one, resulting in the persistence of nocturnal warming over the coast near Kangnung city and the sea surface and the formation of nocturnal thermal high (tropical night). One of possible mechanism on the formation of tropical night is some amount of heat transfer from warm pool of 34°C into the coastal surface, penetrating through very shallow nocturnal surface inversion layer less than 100 m depth.

3.3. *Comparison of observed results with calculated ones by a model*

Through 48 h numerical simulation with G-ANAL data sets, numerical simulation results of air temperature on heat budget such as sensible heat in

Table 1. Comparison of calculated air temperature (°C) to observed one at Kangnung city from August 14 through 15, 1995.

Date	Comparison	1200	500	800	2100	0000	0300	0600	0900
8/14 to	Observed	35.0	34.6	33.4	30.0	29.8	27.6	26.5	29.9
8/15	Calculated	35.0	34.0	32.0	30.0	29.0	29.0	29.0	32.0

the coarse-mesh and fine-mesh domains were compared with hourly air temperature measured by Kangnung Local Meteorological Administration. The air temperature calculated by the model well represents observed ones with a discrepancy of 5–10% error.

4. Conclusions

As the convergence of sensible heat flux from the ground surface of mountain (or inland coast) toward upper level atmosphere is much greater than the flux on the coastal sea, sensible heat flux should be accumulated inside thermal internal boundary layer along the eastern slope of the mountain and convective boundary layer over the top of the mountain. Then, accumulated sensible heat flux under the influence of sea breeze circulation returning from the mountain top toward the coastal surface should be transported into the coast, resulting in high air temperatures in the coastal inland and sea. Very small sensible heat flux divergence occurs in the coast and coastal sea, but the flux divergences are very big at the top of the mountain and along its eastern slope. Thus, nocturnal air temperature on the sea and coastal inland surfaces are not much changed from daytime ones, because of much more cooling down of the mountain surface than the coastal surface and heat transfer from warm pool over the coast toward the coastal surface. Thus, as sensible heat flux is not much changed in the coastal sea for day and nighttime hours, resulting in a very high air temperature, called tropical night.

Acknowledgments

This work was supported by Korean Meteorological Administration for “Gangwon region heavy snowfall prediction skill development from 2002–2006 and by Meteorological Research Institute of Japan through a visiting research program in 1998. The author wishes to thank Mr. Syunji. Takahashi, Japan Meteorological Agency and Dr. Milton S. Speer, Bureau of Meteorology, Australia for their helpful comments on this research and to Dr. Junji Sato of Meteorological Research Institute for using Hitachi super-computer facility.

References

1. S. P. S. Arya, *Introduction to Micrometeorology* (Academic Press, New York, 1988).
2. G. S. Raynor, S. SethuRaman and M. Brown, *Boundary Layer Meteorology* **16** (1979) 4587.
3. R. A. Pielke, *Mesoscale Meteorological Modeling* (Academic Press, New York, 1984).
4. H. Choi, *La Mer* **34** (1996) 133.
5. H. Choi, *Water, Air & Soil Pollution: Focuss* **3** (2003) 31.
6. T. N. Palmer, G. J. Smith and R. Swinbank, *Quart. J. Royal Meteor. Soc.* **112** (1986) 1001.
7. J. Kondo, T. Kuwagata and S. Haginoya, *J. Atmos. Sci.* **46** (1989) 2917.
8. C. D. Whiteman, *Meteor. Monog.* 40, *Amer. Meteor. Soc.* 5 (1990).
9. J. R. Holton, *Introduction to Dynamic Meteorology* (Academic Press, New York, 1992).
10. T. Kuwagata, M. Sumioka, N. Masuko and J. Kondo, *J. Meteor. Soc. Japan* **68** (1990) 625.
11. J. Baik, Y. Kim and H. Chun, *J. Appl. Meteor.* **40** (2001) 1462.
12. H. Choi and J. Kim, *Korean J. Geophys. Res.* **25** (1997) 57.
13. F. Kimura and S. Takahashi, *Atmos. Environ.* **25** (1991) 155.
14. S. Takahashi, *Manual of LAS model* revised by Dr. J. Sato (1998).